Chemie der Erde 78 (2018) 432–461

Contents lists available at ScienceDirect

Chemie der Erde

journal homepage: www.elsevier.com/locate/chemer

Petrology, geochemistry and geodynamic setting of Eocene-Oligocene alkaline intrusions from the Alborz-Azerbaijan magmatic belt, NW Iran

Nasser Ashrafi[a,*], Ahmad Jahangiri[b], Noriko Hasebe[c], G. Nelson Eby[d]

[a] Department of Geology, Payame Noor University, P.O. Box 19395-3697 Tehran, Iran
[b] Department of Geology, Natural Science Faculty, University of Tabriz, Iran
[c] Institute of Nature and Environmental Technology, Kanazawa University, Japan
[d] Department of Environmental, Earth, and Atmospheric Sciences, University of Massachusetts Lowell, USA

ARTICLE INFO

Handling Editor: Hadi Shafaii Moghadam

Keywords:
Neo-Tethys
Shoshonitic magmatism
Nepheline syenite
Extension regime
Sevan-Akera-Qaradagh

ABSTRACT

The Kaleybar, Razgah and Bozqush (KRB) intrusions were studied to better understand subduction-related Eocene-Oligocene alkaline magmatism in NW Iran. The bulk of intrusions mainly consist of Si-undersaturated rocks including foid-bearing monzonite and syenite (nepheline syenite, pseudoleucite syenite) with some foid-bearing diorite and gabbro. In addition, they are spatially associated with Si-saturated rocks ranging in composition from monzo-diorite to syeno-granite. The main mafic rock-forming minerals of the studied rocks are olivine ($Fo_{44}Fa_{56}$), clinopyroxene (diopside to augite), biotite (Mg-biotite through Fe-biotite), amphibole (ferro-pargasite and magnesio-hastingsite with Mg# < 0.55), and garnet (Ti-andradites). Based on whole rock geochemistry, the foid-syenites and associated rocks show mildly alkaline (shoshonitic) affinity. The content of SiO_2, $K_2O + Na_2O$, and K_2O/Na_2O ratio ranges from 47.8 to 60.7 wt.%, 5.31 to 16.33 wt.%, and 0.6 to 3.2, respectively. The intrusions are commonly metaluminous, with an aluminum-saturation index (ASI) ranging from 0.66 to 1.01. Almost all the rocks display similar arc-related geochemical features characterized by the enrichment in large ion lithophile elements (LILE) and light rare earth elements (LREE) together with the depletion in high field strength elements (HFSE). The chondrite-normalized REE patterns show no to marked negative Eu anomaly (Eu/Eu* = 0.55 to 1.12), $(La/Yb)_N$ = 8.16 to 31, $(La/Sm)_N$ = 2.80 to 10.59, and $(Tb/Yb)_N$ = 0.84 to 2.40. The evaluation of the REE patterns for the KRB magmas and the comparison of the trace element ratios with experimental studies indicate a chemically enriched lithospheric mantle source composed of garnet-spinel-lherzolite that have underwent a low degree of partial melting < 5% to generate the KRB intrusions. Based on the present data, we infer that the mantle source was contaminated by a subduction component and the melting of the mantle lithosphere occurred by local extension in an overall convergent regime in NW Iran. The extension regime during the Eocene is proposed to be the result of the Neo-Tethys slab roll-back and the Sevan-Akera-Qaradagh (SAQ) slab break-off.

1. Introduction

Pre-, syn- and post-collision alkaline magmatism are reported from many collision zones (e.g., Barker, 1987; Muller et al., 1992; Harris et al., 1994; Alici et al., 1998; Turner et al., 1996; Aldanmaz et al., 2000; Hajalilou et al., 2009; Ahmadzadeh et al., 2010; Dabiri et al., 2011; Shafaii-Moghadam et al., 2014; Prelević et al., 2015; Moritz et al., 2016a; Rezeau et al., 2017). During the life of a subduction zone the typical calc-alkaline magmas tend to become more potassic with time and may give way to igneous rocks of the shoshonitic/alkaline association (e.g., Fitton and Upton, 1987; Muller and Groves, 2000). There are two circumstances under which subduction processes can lead to the generation of more normal alkaline magmas. Once the descending slab has become dehydrated at depth it loses its capacity to stimulate the generation of calc-alkaline magmas but it can still cause melting in the overlying asthenosphere (e.g., Tatsumi and Eggins, 1995). This can lead to the production of alkaline magmas from the mantle above the deepest parts of subduction zones (e.g., Barker, 1987). After the cessation of subduction, relaxation of the former compressive regime often results in extension and the generation of alkaline magmas (e.g., Carmichael et al., 1996; Peccerillo and Frezzotti, 2015).

Alkaline rocks in general can be derived from partial melting of metasomatized upper mantle sources (e.g., Dawson, 1987; Eby et al., 1998), from unmetasomatized asthenospheric mantle by very small

* Corresponding author.
E-mail address: n_ashrafi@pnu.ac.ir (N. Ashrafi).

https://doi.org/10.1016/j.chemer.2018.10.004
Received 25 February 2018; Received in revised form 5 October 2018; Accepted 5 October 2018

degrees of partial melting followed by extensive crystal fractionation (e.g., Fitton, 1987), from interaction of asthenosphere-derived melts with the overlying lithosphere (e.g., Menzies, 1987), from crystal fractionation from alkali basaltic precursors combined with varying degrees of crustal contamination (e.g., Brotzu et al., 1997; Korobeinikova et al., 2000; Litvinovsky et al., 2002; Jung et al., 2004; Wang et al., 2005; Zhang et al., 2010) or from small-degree partial melting of enriched upper mantle or even lower crust (e.g., Woolley and Jones, 1987; Zanvilevich et al., 1995; Motoki et al., 2015). Decompression melting of metasomatized lithospheric lherzolite with minor phlogopite and pargasite has been invoked for the formation of high-K magmas by dehydration melting at 1–1.5 GPa, 1050–1150 °C (Conceição and Green, 2004). Magmatic rocks with shoshonitic and ultrapotassic (with high K and/or high MgO and with different degree of silica saturation/undersaturation) signatures are abundant in the Mediterranean–Iran regions, and their origin has been correlated to partial melting of clinopyroxene–amphibole–phlogopite veins in a metasomatized mantle source (e.g., Prelević et al., 2008; Pe-Piper et al., 2009). Their genesis is suggested to be related to sediment fluids/melts and subsequent K-metasomatism and enrichment of peridotitic lithosphere (e.g., Conticelli et al., 2009). Factors that control the silica activity of the high-K melts are suggested to be related to: (1) abrupt change of the composition of the recycled sediments (e.g., Conticelli and Peccerillo, 1992; Frezzotti et al., 2009) and/or (2) interaction between deep asthenospheric mantle with lithospheric portion of mantle wedge through slab tears within the descending slab (e.g., Prelević et al., 2012).

The NW Iran region, confined by the Tabriz, Talesh, and Arax (or Araks) faults, is the southeastern continuation of the Lesser Caucasus and located in the western part of the Alborz-Azerbaijan magmatic belt (AAMB) (Fig. 1). This region is one of the most important metallogenic provinces (e.g., Richards, 2015; Richards and Sholeh, 2016; Moritz et al., 2016b) and the most tectonically active area along the Alpine-Himalayan Orogenic belt. The studied area is located between the Bitlis-Zagros suture in the southwest and the nearest Sevan-Akera-Qaradagh (SAQ) suture in the northeast (Fig. 1). The NW-trending AAMB stretches from the Alborz Mountains to Azerbaijan Province and is separated from the Urumieh-Dokhtar magmatic arc (UDMA) to the south by the Tabriz fault (Fig. 1).

The Turkish-Iranian plateau, as a main part of the Arabia-Eurasia accretionary orogeny, arose from a complex geotectonic evolution with the successive closure of the northern and southern branches of the Neo-Tethys oceans during the Mesozoic and Cenozoic, respectively (e.g., Rolland et al., 2012; Rolland, 2017; Sosson et al., 2016; Hässig et al., 2015). The final Arabia-Eurasia collision is unclear and occurred either during the Late Cretaceous (Mohajjel and Fergusson, 2000), Late Eocene to Oligocene (Vincent et al., 2007; Allen and Armstrong, 2008; Agard et al., 2011; Ballato et al., 2011; Van Hunen and Allen, 2011; Rolland et al., 2012; Chiu et al., 2013; Kaislaniemi et al., 2014a,b; Moritz et al., 2016a; Rezeau et al., 2017), or Early to Middle Miocene (McQuarrie et al., 2003; Okay et al., 2010).

The temporal distribution of the Cenozoic alkaline magmatism in the Turkish-Iranian plateau, northeast of the Bitlis-Zagros suture, shows different phases of magma generation mainly in the late Eocene, late Miocene and Plio–Quaternary (e.g., Dilek et al., 2010; Eyuboglu et al., 2011; Shafaii-Moghadam et al., 2014; Moritz et al., 2016a; Rezeau et al., 2017). The Cenozoic magmatism of Iran, especially in the AAMB, has typically been viewed in terms of widespread and voluminous Eocene–Oligocene arc-related volcanism and plutonism (e.g., Berberian and King, 1981; Aftabi and Atapour, 2000; Aghazadeh et al., 2010; Verdel et al., 2011; Ballato et al., 2011; Castro et al., 2013; Nabatian et al., 2014). The voluminous subduction-related magmatism (calc-alkaline, alkaline and shoshonitic) occurred during the Eocene in the back arc of the Neo-Tethys subduction zone (e.g., Berberian and King, 1981). Some authors have proposed an Eocene to Miocene phase of lithospheric extension in Iran and adjacent regions to explain the local alkaline and shoshonitic Tertiary magmatism (Hassanzadeh et al., 2002; Vincent et al., 2005; Castro et al., 2013). Alternatively, a decrease of the degree of partial melting of the sub-lithospheric mantle within a compressional context related to the initiation of the Arabia-Eurasia collision is also proposed in the southernmost Lesser Caucasus for the generation of shoshonitic magmas (e.g., Rezeau et al., 2017).

The temporal geodynamic evolution from a subduction to collision to post-collisional setting is controversial along the Turkish-Iranian plateau. Also, there is no consensus regarding the origin of the Eocene to Oligocene calc-alkaline, alkaline, and shoshonitic magmatism in the AAMB. More recently, in the southernmost Lesser Caucasus, Rezeau et al. (2017) showed a clear evolution from calc-alkaline in the mid-Eocene to shoshonitic in the late Eocene-Early Oligocene in the Meghri-Ordubad pluton. The later shares geochemical similarities with the magmatism reported in the AAMB in the Eocene to Oligocene (Moritz et al., 2016b). Is the Eocene-Oligocene AAMB magmatism a result of the subduction of Neo-Tethys oceanic crust beneath the Iranian plate? Or is it because of extension and late- to post-collisional events? Or is it due to subduction of an unknown oceanic crust beneath the Alborz-Azerbaijan plate? Or is it because of early subduction during the Eocene, followed by the initiation of the Arabia-Eurasia collision in the late Eocene-Early Oligocene? All of these questions have been the subject of debate.

In comparison with widespread occurrences of the Eocene-Oligocene Si-oversaturated calc-alkaline and shoshonitic rocks throughout the AAMB, the Si-undersaturated alkaline/shoshonitic rocks appear to be rare. The main outcrops of the foid-bearing alkaline intrusions have been discovered from Kaleybar, Razgah, and Bozqush (KRB) area in the NW of Iran (Fig. 1). Also, there are small outcrops of foid-bearing intrusions close to the main outcrops (e.g., Marzrud, Hashtsar, Bashkand, Abas-abad, Van-abad, and Leghlan area). Detailed studies of the relationship between magma genesis and the geodynamic setting of the Eocene-Oligocene foid-bearing plutons of NW Iran are rare (Babakhani, 1981; Moinevaziri, 1999; Ashrafi, 2009; Modjarrad et al., 2011; Tajbakhsh et al., 2012). In this paper we present new data on the geology, petrography, mineral chemistry and major, trace, and rare-earth-elements characteristics of the KRB intrusions to identify the nature of the parental magmas and to better understand magmatic processes that generate alkaline melt in subduction-related environment in the AAMB.

2. Regional geology and geodynamics

Discovery of the Late Cretaceous pelagic limestones, pillow basalts, and ophiolites along the "Qaradagh suture zone" in northwest Iran (Berberian et al., 1981) illustrated the southeastern continuation of the Mesozoic Sevan-Akera Ocean, i.e. the northern branch of the Neo-Tethys Ocean, in Iran. In the northern branch of the Neo-Tethys, an intra-oceanic north-dipping subduction was operating from the Middle Jurassic to the Late Cretaceous and induced the opening of a back-arc basin (the SAQ basin) floored with oceanic crust. The present SAQ suture zone marks the closure of both the Neo-Tethys and its internal back-arc basin (e.g., Berberian, 1983; Galoyan et al., 2009; Rolland et al., 2009; Hässig et al., 2015; Sosson et al., 2016). The SAQ ophiolite is correlated with the Izmir-Ankara-Erzincan suture zone of northern Anatolia (Yilmaz et al., 2000; Hässig et al., 2013). The northward subduction of the northern branch of the Neo-Tethys oceanic plate under the Eurasian continental plate is confirmed by the arc-type magmatic products that are found on the Eurasian southern margin from Azerbaijan, Talesh, the west-central Alborz Mountains, and the Lesser Caucasus in the east to the eastern Pontides in the west (Adamia et al., 1981; Berberian, 1983; Lordkipanidze et al., 1989; Meijers et al., 2010; Okay and Nikishin, 2015; Robinson et al., 1996). Subduction started in the Middle Jurassic and the oceanic plate was entirely subducted from Late Cretaceous to Early Paleocene in the Lesser Caucasus (Hässig et al., 2015; Rolland et al., 2012; Sosson et al., 2010) and from Paleocene to Eocene in the

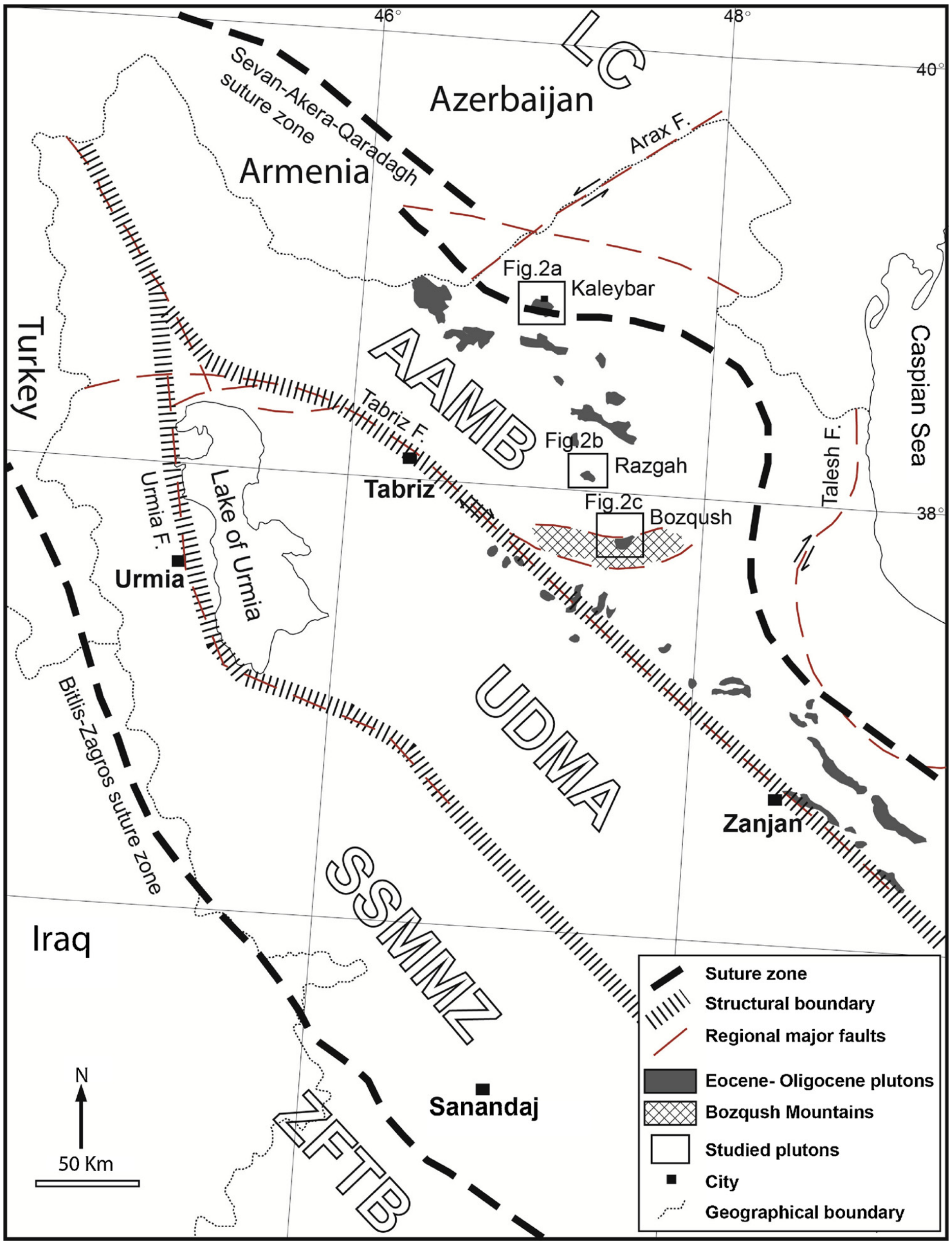

Fig. 1. Map of the important Iranian structural-magmatic zones and Eocene-Oligocene plutons in NW Iran with location of the Kaleybar, Razgah, and Bozqush plutons, shown as squares (simplified and modified from Aghanabati (1990) and Berberian (1983)). The studied plutons are surrounded between two old long major faults, in the W-SW by the Tabriz fault and in the E-NE by the Talesh (Astara) fault. Abbreviations: AAMB, Alborz-Azerbaijan Magmatic Belt; LC, Lesser Caucasus; SSMMZ, Sanandaj–Sirjan Metamorphic and Magmatic Zone; UDMA, Urumieh–Dokhtar Magmatic Arc; ZFTB, Zagros-Folded-Thrust Belt.

Pontides (Espurt et al., 2014; Lefebvre et al., 2013; Okay and Nikishin, 2015; Robertson et al., 2014; Sengör et al., 2003). The SAQ ophiolite was obducted on the Lesser Caucasus and NW Iran between 88 and 83 Ma (Galoyan et al., 2007; Rolland et al., 2010), and final collision between the Eurasian margin and the Gondwana-derived blocks, i.e. the South Armenian and northwestern Central Iranian blocks, took place at 73-71 Ma (Rolland et al., 2009).

Paleogene subduction-related plutonic rocks cut the SAQ suture zone (~50 Ma; Mederer et al., 2013) which indicate that the South Armenian block was already accreted to the southern Eurasian margin. Cenozoic magmatism is commonly reported from the Lesser Caucasus to southeastern Iran and ascribed to the northward subduction of the southern branch of the Neo-Tethys ocean during the convergence of the Arabian plate towards the Eurasian margin and the subsequent collision (e.g., Mouthereau et al., 2012; Castro et al., 2013; Chiu et al., 2013; Moritz et al., 2016a; Rezeau et al., 2017).

The Arabian Peninsula is converging northward with respect to Eurasia at > 20 mm/yr

(DeMets et al., 1990) and has formed the Bitlis-Zagros suture extending southeast from Turkey to the Persian Gulf (Fig. 1). According to plate-tectonic reconstructions, the motion of Arabia with respect to Eurasia changed from about NE to N during the Miocene (Avagyan et al., 2010), coupled with a decrease in plate convergence rates (e.g., McQuarrie et al., 2003; Bertrand et al., 2014). It is proposed that the Arabia-Eurasia collision began along the Turkish margin and progressed towards southeastern Iran through time (e.g., Chiu et al., 2013). Collision age estimates range from the Late Cretaceous to Pliocene, with most estimates between 40 and 20 Ma (Allen and Armstrong, 2008; Agard et al., 2011; Ballato et al., 2011; Chiu et al., 2013; McQuarrie and van Hinsbergen, 2013; Kaislaniemi et al., 2014a,b; Moritz et al., 2016a;

Rezeau et al., 2017). Suturing has not yet occurred within the Gulf of Oman and the Makran where subduction remains active.

The Iranian plateau comprises a number of continental fragments that have been welded together along a suture zone of oceanic nature (e.g., Azizi and Moinevaziri, 2009). Based on structural trends, the Iranian plateau can be divided into seven fragments which are bounded by major faults (Fig. 1): Zagros-Folded-Thrust Belt (ZFTB), Sanandaj–Sirjan Metamorphic and Magmatic Zone (SSMMZ), Urumieh–Dokhtar Magmatic Arc (UDMA), Alborz-Azerbaijan Magmatic Belt (AAMB), Central Iran Blocks, Kopeh Dagh, and East Iran Belt (e.g., Dewey et al., 1973; Jackson and McKenzie, 1984; Sengör, 1984; Stöcklin and Nabavi, 1973). The subduction of Neo-Tethys beneath the Iranian plate during the Late Cretaceous to Paleogene accompanied by the accretion of the Iranian blocks/terranes, and the subsequent continent–continent collision of the Arabian plate during the Eocene to Miocene, was responsible for developing three ribbon structural zones in Iran (ZFTB, SSMZ, and UDMA).

Magmatic activity in the UDMA and the AAMB started in the Late Cretaceous and continued during Eocene until the Quaternary period (e.g., Berberian et al., 1982; Azizi and Moinevaziri, 2009; Chiu et al., 2013). The Eocene magmatism is volumetrically dominant at the surface in both regions (e.g., Alavi, 2004; Farhoudi, 1978; Moinevaziri, 1999). Geochemical studies indicate that the UDMA mainly is composed of subduction-related calc-alkaline rocks (e.g., Berberian et al., 1982) although alkaline rocks are reported locally (Aftabi and Atapour, 2000; Amidi et al., 1984; Hassanzadeh, 1993; Moayyed et al., 2008; Moradian, 1997).

In the southernmost Lesser Caucasus and the AAMB, the Middle Eocene to Miocene magmatism was punctuated by the intrusion of plutons, which include the Meghri-Ordubad polycyclic pluton with ages of ~18–38 Ma (Rezeau et al., 2016, 2017), the Tarom, Lavasan, and Qasr-e-Firuzeh intrusions with emplacement ages of ~35–40 Ma (Ballato et al., 2011; Rezaeian et al., 2012; Nabatian et al., 2014), the Arasbaran-Taroum batholith with ages of ~23–38 Ma (Aghazadeh et al., 2010, 2011; Castro et al., 2013). There is no isotopic dating, crystallization age, for the KRB plutons. However, the cooling ages for the KRB plutons range from ~29–40 Ma (Ashrafi et al., 2018), which determined by the apatite fission track analysis. In the Alborz, submarine volcaniclastic sedimentation ended in the Late Eocene-Early Oligocene (~34 Ma) as the tectonic regime reverted to compression. The timing of this change is consistent with a regional termination of the voluminous arc and back-arc magmatism (Ballato et al., 2011) across Iran and adjacent areas, which is related to the initial collision of Arabia and Eurasia (Allen and Armstrong, 2008). At this time the southern Alborz emerged above sea level and was affected by widespread erosion, terrestrial deposition, and limited subaerial basaltic volcanism (e.g., Emami, 2000; Verdel et al., 2011). This transition towards a compressional regime affected most of the Arabia-Eurasia collision zone and is recorded by a regional unconformity seen in the Central Iranian Plateau, Turkey, Caucasus, Talesh and Zagros mountains (Hessami et al., 2001; Brunet et al., 2003; Vincent et al., 2007; Morley et al., 2009). The post-suturing magmatism in the UDMA and the SSMZ was probably controlled by roll-back processes following break-off of the Neo-Tethys subducted slab (Ghasemi and Talbot, 2006; Jahangiri, 2007; Agard et al., 2011; Mouthereau et al., 2012).

To summarize, four main magmatic events have occurred in the NW Iran (Alberti et al., 1976; Comin-Chiaramonti et al., 1979; Didon and Gemain, 1976; Stöcklin and Nabavi, 1973), and the KRB plutons were formed during the second magmatic event described below.

(1) The first, from Late Cretaceous to Early Eocene, is mainly characterized by volcanic rocks as well small sub-volcanic intrusions. The magmatism was first submarine and then subaerial with blairmoritic character. The magmatism has limited areal extent and was characterized by a strong explosive activity.
(2) The second, from Eocene to Oligocene, is a shoshonitic event characterized by many granitic-syenitic-gabbroic stocks/batholiths (e.g., Aghazadeh et al., 2010; Castro et al., 2013; Nabatian et al., 2014). The most abundant volcanic rocks are Ne-normative tephritic lavas in which the foids are mainly represented by analcite (analcite-bearing tephritic phonolites).
(3) The third magmatic event, from Miocene to Pliocene, is characterized by medium-K calc- alkaline and foid-free volcanic rocks (9–11 Ma; Alberti et al., 1976) and small intrusions. Products of this volcanism range from latitic rocks to alkali-quartz trachytes (e.g., Jahangiri, 2007). Limited occurrences of Miocene analcite and leucite-bearing alkaline volcanics are also reported from the NW Iran (Moayyed et al., 2008; Shafaii-Moghadam et al., 2014).
(4) The fourth magmatic event, Plio-Quaternary volcanism, displays sub-alkaline, high-K calc-alkaline and alkaline affinities (e.g. Ahmadzadeh et al., 2010; Dabiri et al., 2011).

3. Field relationships

The Kaleybar pluton was emplaced in Late-Cretaceous limestones and intermediate to acid lava flows. There are distinct contact metamorphic areoles and chilled margins around the Kaleybar pluton. The Kaleybar pluton mainly consists of gabbro, quartz monzonite and nepheline syenite (Fig. 2a). Pyroxenites as enclave and lenticular small bodies in and/or near the gabbro occur in the southern part of the pluton. The microgranite and quartz monzonite stocks occur in the north and center of the Kaleybar pluton. Based on field evidence, such as enclaves, intrusive contacts, and apophyses within the Kaleybar pluton, the pyroxenite and gabbro are older than the nepheline syenite and quartz monzonite. The general textures of the main rocks are coarse-grained granular and porphyritic. They have been mostly cut by abundant pink-coloured aplitic and pegmatitic dykes. Lamprophyric, gabbroic and phonolitic dykes also occur in the Kaleybar pluton.

The Razgah pluton is in contact with Quaternary sediments. However, there are Eocene and Miocene basaltic andesite and gypsiferous marl in the vicinity of the Razgah pluton. The Razgah pluton composition varies from pseudoleucite syenite to monzo-diorite/syenite (Fig. 2b). The contact between the pseudoleucite syenite and monzo-diorite/syenite is typically controlled by faulting, however a gradual change in composition is observed locally. The pseudoleucite syenites have porphyritic texture with pseudoleucite megacrysts, whereas the monzo-diorites/syenites have coarse-grained texture. Both the pseudoleucite syenites and the monzo-diorites/syenites have been cut by abundant pink-coloured micro-syenitic, micro-granitic, and pegmatitic dykes as well as dark grey phonolitic dykes up to 4 m in thickness. The Razgah pluton is cut by aplitic and silicic dykes along the western margin, where a copper mineralization zone is reported.

The Bozqush pluton was emplaced into Eocene mega-porphyry andesite, analcite trachy-andesite, trachyte, and tuff. A slight contact metamorphic areole and a chilled margin are observed along the eastern and western contact of the Bozqush pluton, respectively. The main rocks of the Bozqush pluton are biotite nepheline syenite and pseudoleucite syenite (Fig. 2c). The pseudoleucite syenite forms a small part of the southern portion of the pluton. The Bozqush pluton is mostly cut by abundant aplitic and pegmatitic dykes up to 5 m thickness. The dykes vary from syenite to granite in composition and are light pink to light grey in color. Scarce dark grey basaltic dykes are also found.

4. Rock types and petrographic features

According to the recommendations of the International Union of Geological Sciences (IUGS) (Le Maitre, 1989), rock compositions for the KRB plutons range from quartz monzonite to syeno-granite for the Si-saturated rocks and from foid-bearing diorite/gabbro to foid syenite with minor foidolite and pyroxenite for the Si-undersaturated rocks (Fig. 3). Detailed description for each the pluton is presented in the following subsections. A summary of the petrographic characteristics of

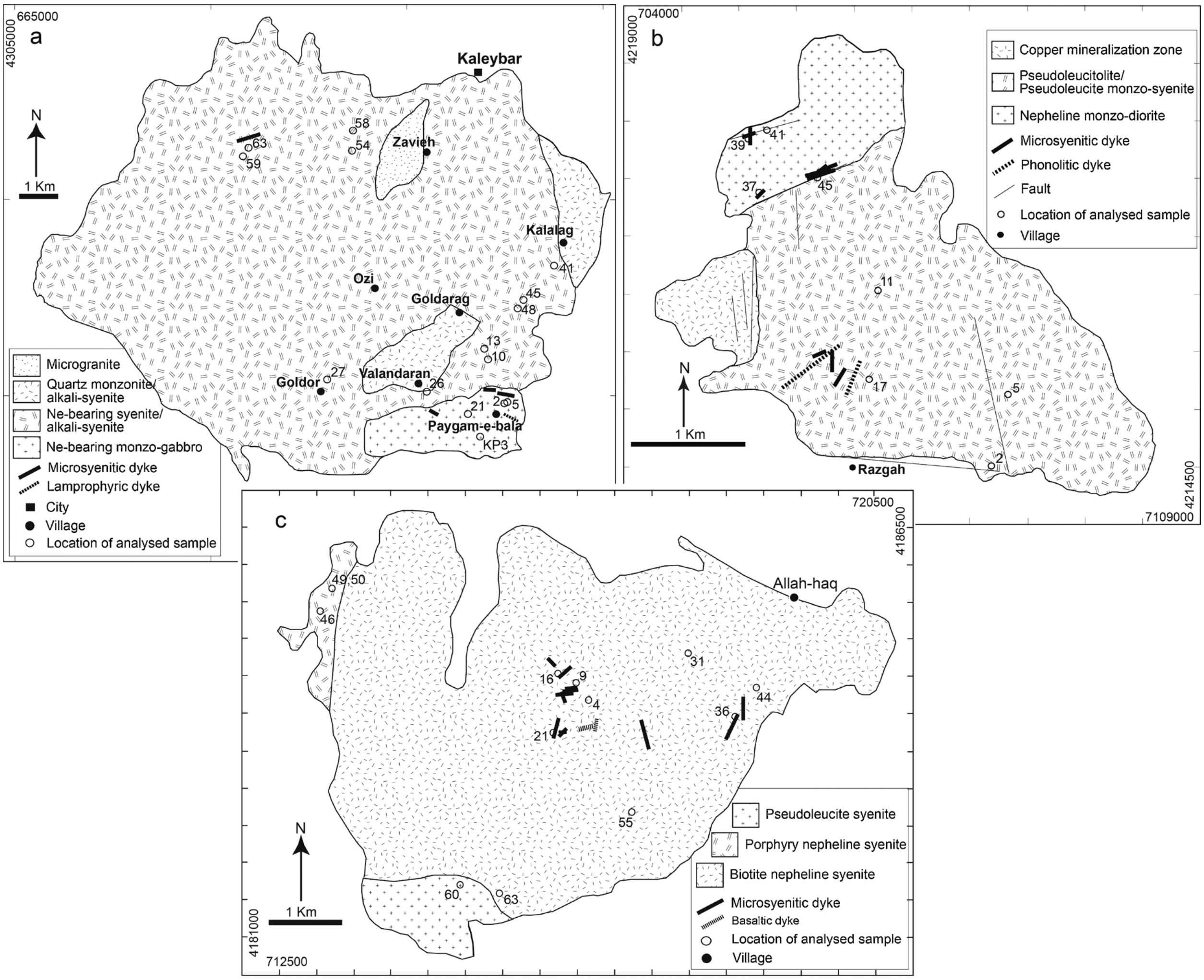

Fig. 2. Geological map of the KRB plutons with the location of analysed samples; (a) the Kaleybar pluton (modified from Mehrpartou and Nazer, 1999; Mehrpartou et al., 1992), (b) the Razgah pluton (modified from Mahdavi and Aminifazl, 1989), (c) the Bozqush pluton (modified from Asadian et al., 1993).

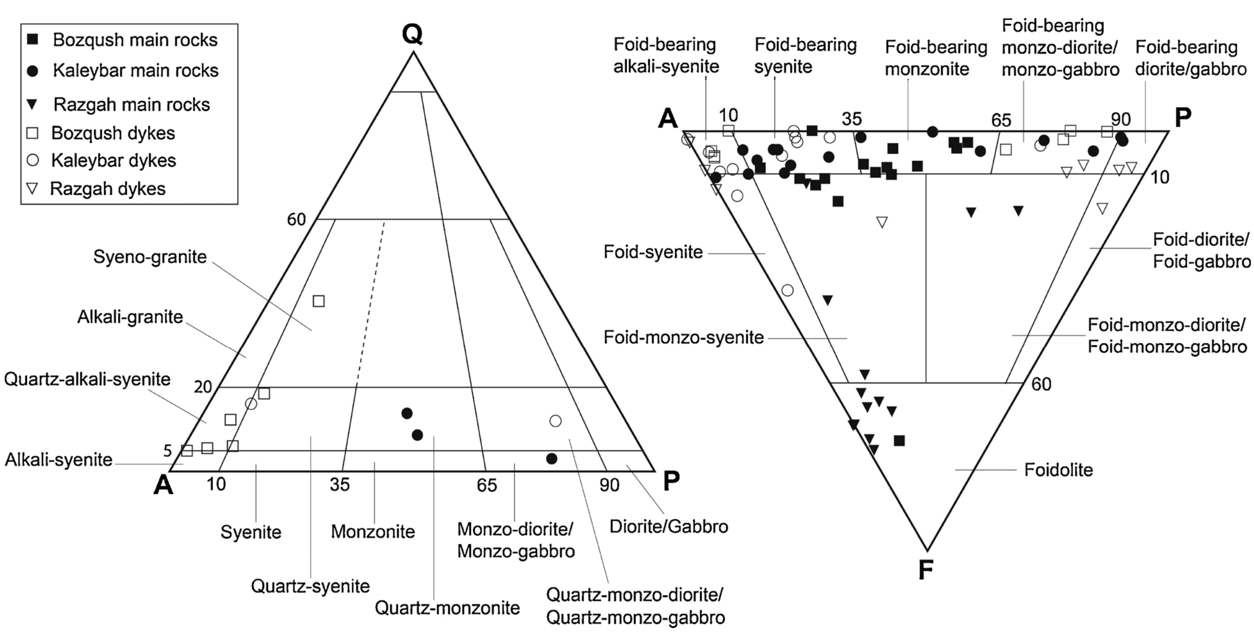

Fig. 3. Modal classification of the samples by quartz (Q), alkali-feldspar (A), plagioclase (P), and feldspathoid (F) (Le Maitre, 1989).

Table 1
Petrographic characteristics of the KRB main rocks.

Pluton	Kaleybar	Razgah	Bozqush
Rock type	NeSy, NeAlSy, NeMo, NeMoDG, NeDG, QtzMo, QtzMoDG, Cpy	Pslsy (PSL), NeMoDG, PslMoSy	NeSy, PslSy (PSL), NeMoSy, NeMo
Texture	porphyry, hypidiomorphic	porphyry (hypidiomorphic)	hypidiomorphic (porphyry)
Grain size	medium, coarse	coarse	medium, coarse
Mafic phase	Cpx, Bt, Amp, (±)Grt,	Cpx, Ol, (±)Bt	Cpx, Amp, Bt
Accessory	Opq,Ttn, Ap, Zrn, (±)Spl	Opq, Ap, Zrn	Opq, Ap, Zrn, Ttn, (±)Grt
Alteration	very slight	slightly to moderately	very slight
Secondary phase	sericite, muscovite, sodalite, analcite, cancrinite, zeolite, epidote, chlorite, quartz, calcite, iron oxide, clay minerals	zeolite, sericite, calcite, iron oxide, muscovite, analcite, cancrinite, iddingsite, chlorite, quartz, clay minerals	sericite, muscovite, analcite, zeolite, epidote, quartz, calcite, clay minerals

Abbreviations: Amp, amphibole; Ap, apatite; Bt, biotite; Cpy, clinopyroxenite; Cpx, clinopyroxene; Grt, garnet; QtzMo, quartz monzonite; QtzMoDG, quartz monzo-diorite/gabbro; NeAlSy, nepheline-bearing alkali-syenite; NeDGnepheline-bearing diorite/gabbro; NeMo, nepheline-bearing monzonite; NeMoDG, nepheline monzo-diorite/gabbro (nepheline-bearing monzo-diorite/gabbro); NeSy, nepheline syenite (nepheline-bearing syenite); Ol, olivine; Opq, opaques; PslSy, pseudoleucite syenite; Spl, spinel; Ttn, titanite; and Zrn, zircon.

the KRB rocks is found in Table 1.

4.1. Kaleybar

The lithologies of the Kaleybar intrusion vary from the mafic clinopyroxenite to more differentiated quartz monzonite and nepheline-bearing alkali-syenite (Fig. 3). The clinopyroxenite contains up to 90% pale pink to green diopside, up to 20% interstitial magnetite, tiny green spinels enclosed by magnetite and occasional pale green amphibole and brown biotite forming ragged areas or rims on pyroxene. Overall, the rock forming minerals are alkali-feldspar, nepheline, plagioclase, amphibole (up to 10%), clinopyroxene (up to 5%), melanite (up to 5%), biotite, apatite, titanite, zircon, spinel, Fe-Ti oxide, quartz, and secondary minerals (Fig. 4a, b and Fig. 5c, d). Spinel only appears in clinopyroxenite and displays a Fe-Ti oxide reaction rim (Fig. 4c).

4.2. Razgah

The lithologies of the Razgah pluton vary from pseudoleucitolite to nepheline monzo-syenite (Fig. 3). The pseudoleucite syenite and nepheline monzo-syenite constitute the main bulk of the pluton. The pseudoleucitolite and pseudoleucite syenite are coarse-grained and porphyritic with pseudoleucite megacrysts up to 5 cm across. The rock forming minerals of the main rocks are pseudoleucite, alkali-feldspar, plagioclase, clinopyroxene (up to 10%), nepheline, olivine (up to 5%), biotite, apatite (up to 2%), zircon, Fe-Ti oxide, and secondary minerals (Fig. 5a, b).

4.3. Bozqush

The lithologies of the Bozqush intrusion vary from nepheline-bearing biotite syenite to nepheline-bearing monzo-diorite (Fig. 3). The rock forming minerals are alkali-feldspar, plagioclase, biotite (up to 10%), clinopyroxene (up to 5%), nepheline, amphibole, melanite,

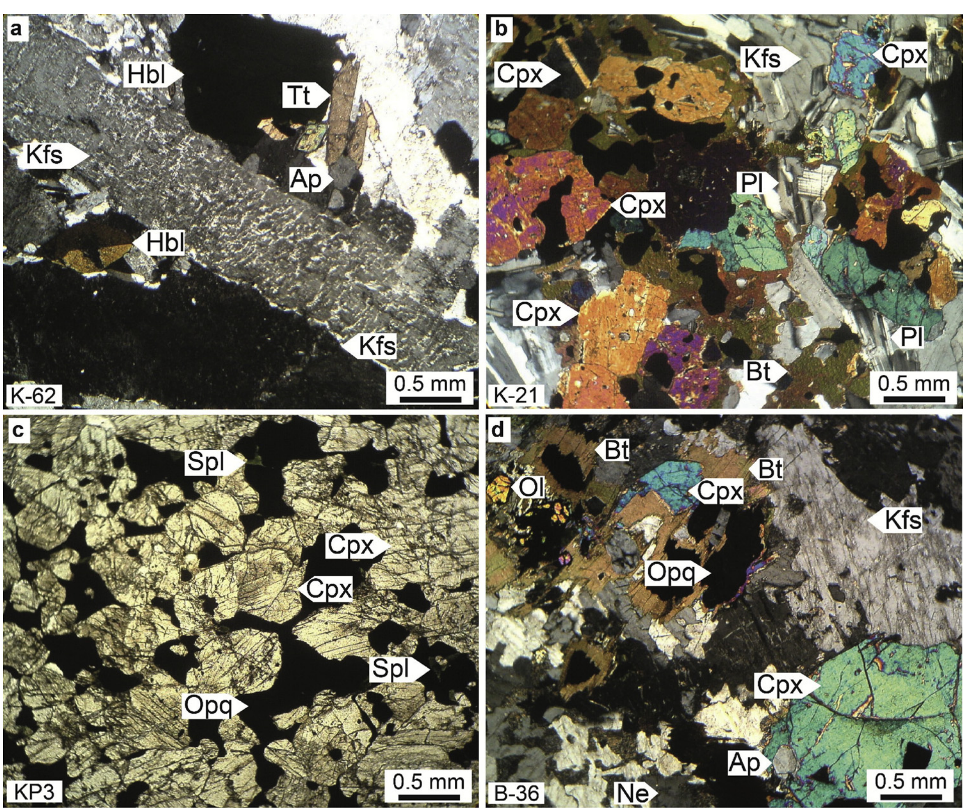

Fig. 4. Photomicrographs of the KRB rocks; (a) microperthitic alkali-feldspar (Kfs), hornblende (Hbl), titanite (Tt) and apatite (Ap) in the Kaleybar nepheline syenite, (b) main minerals of clinopyroxene (Cpx), plagioclase (Pl) and biotite (Bt) in the Kaleybar monzo-gabbro, (c) the Kaleybar clinopyroxenite with granular texture and minerals of clinopyroxene, Fe-Ti oxide (Opq) and spinel (Spl), (d) the Bozqush nepheline syenite with hypidiomorphic texture and minerals of microperthitic alkali-feldspar, biotite (enclosing Fe-Ti oxide), clinopyroxene, opacity olivine (Ol), nepheline (Ne) and apatite.

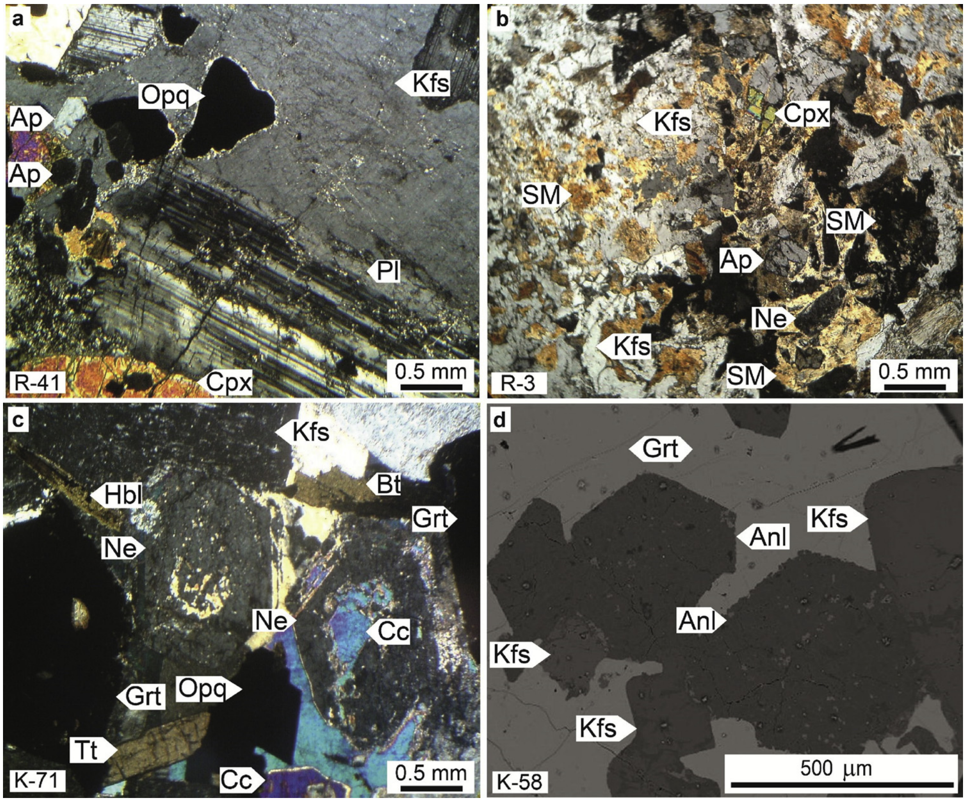

Fig. 5. (a–c) Photomicrographs of the KRB rocks; (a) coarse minerals of alkali-feldspar (Kfs), plagioclase (Pl), clinopyroxene (Cpx), apatite (Ap), Fe-Ti oxide (Opq) in the Razgah monzonite, (b) intergrowth of alkali-feldspar and nepheline (Ne) accompanied by uncertain secondary minerals (SM) inside pseudoleucite in the Razgah pseudoleucite syenite, (c) euhedral nephelines slightly altered to cancrinite (Cc) accompanied by alkali-feldspar, garnet (Grt), titanite (Tt), hornblende (Hbl), biotite (Bt), and Fe-Ti oxide in the Kaleybar nepheline syenite. (d) Back-scattered electron image of analcimized nepheline (Anl) and alkali-feldspar within coarse garnet in the Kaleybar nepheline syenite.

olivine, apatite, titanite, zircon, Fe-Ti oxide, pseudoleucite, and secondary minerals (Fig. 4d). The alkali-feldspar generally shows microperthitic and poikilitic texture. Optically, the plagioclase occasionally shows a distinct zoning. Biotite is the main hydrous mineral and occurs as individual grains and/or enclosing the Fe-Ti oxides. The amphibole forms rims on the clinopyroxene. Fine-grained melanite garnet (up to 1%) only appears in a sample from the margin of the pluton.

5. Analytical methods

Mineral analyses were done using a JEOL electron probe X-ray microanalyzer (JXA-8800) at the Kanazawa University. Operating conditions were an acceleration voltage of 20 kV, a beam current of 20 nA, and 3 µm probe diameter. Natural and synthetic minerals of known compositions were used as standards. Representative analyses are listed in Table 2.

Thirty-seven representative fresh whole-rock samples were powdered using an agate ball mill. Major elements were analysed by ICP-AES and trace elements, including rare-earth elements (REE), were analysed by ICP-MS at the ALS Chemex lab (Canada). The detection limit for major elements oxides is 0.01%. The analytical results for the samples are presented in Table 3.

6. Mineral chemistry

6.1. Olivine and spinel

The olivines from the Razgah have the composition of $Fo_{44}Fa_{56}$, which characterized them as hortonolite (Table 2).

Spinels appear in the Kaleybar clinopyroxenite and contain ~62 wt.% Al_2O_3, ~20 wt.% MgO, ~16 wt.% FeO, up to 0.18 wt.% MnO, up to 0.06 wt.% TiO_2, and up to 0.04 wt.% NiO (Table 2).

6.2. Fe-Ti oxide

The chemistry of magnetite and ilmenite from the Bozqush nepheline syenite and the Kaleybar clinopyroxenite has been determined. Unlike magnetite, ilmenite is quite scarce in the studied plutons. In the nepheline syenite, ilmenite occurs as exsolution lamella in magnetite, which likely illustrates subsolidus reequilibration. The nepheline syenite magnetites have 9.75–19.97 wt.% TiO_2 and 1.26–2.25 wt.% Al_2O_3 while the clinopyroxenite ones contain 1.81–4.42 wt.% TiO_2 and 0.70–2.90 wt.% Al_2O_3. The ilmenites contain ~3.3 wt.% MnO and up to ~0.65 wt.% MgO (Table 2).

6.3. Clinopyroxene

The clinopyroxenes range in composition from diopside to augite (Fig. 6c). Considering the atomic proportion of Wo, En and Fs in the studied clinopyroxenes, variation in end-member components mostly involves the interchange of En and Fs. The clinopyroxenes Mg#, Mg/(Mg + Fe), ranges from ~0.8 in the Kaleybar clinopyroxenite and monzo-gabbro to ~0.6 in the Bozqush nepheline syenite and the Razgah pseudoleucite syenite. Moreover there is $Ca^{M2}(Fe^{2+},Mg)^{M1} = Na^{M2}Fe^{3+M1}$ exchange in the clinopyroxenes.

6.4. Amphiboles

Chemical composition of the amphiboles is ferro-pargasite (Mg# < 0.5; $^{VI}Al \geq Fe^{3+}$) and magnesio-hastingsite (Mg# > 0.5; $^{VI}Al < Fe^{3+}$) with Mg# < 0.55 (Fig. 6a). The Kaleybar amphiboles are richer in Ca + Al^{IV} and poorer in Ti than the Bozqush ones and $CaAl^{IV}$ = SiNa exchange is the main substitution.

6.5. Feldspars

Alkali-feldspars from the Bozqush nepheline syenite vary from Or_{61} Ab_{36} An_3 to Or_{84} Ab_{15} An_1 (Table 2). The average anorthite content of

Table 2
Representative electron microprobe analysis of some minerals from the KRB plutons.

Mineral	olivine				
Pluton	Razgah				
Rock type	PslSy				
Sample no.	1	2	3	4	5
Wt.%					
SiO_2	34.76	34.87	35.07	34.45	34.64
TiO_2	0.02	0.03	0.02	0.05	0.03
FeO	46.73	46.78	46.24	45.51	45.37
MnO	2.43	2.38	2.45	2.33	2.25
MgO	18.35	18.85	19.30	19.42	19.96
CaO	0.56	0.56	0.49	0.40	0.50
Na_2O	0.02	–	0.03	0.01	–
NiO	–	0.03	–	–	–
Total	102.88	103.49	103.60	102.17	102.75
Cations on the basis of 4 (O)					
Si	1.003	0.999	1.000	0.996	0.994
Ti	–	0.001	–	0.001	0.001
Fe^{2+}	1.127	1.121	1.103	1.100	1.088
Mn	0.059	0.058	0.059	0.057	0.055
Mg	0.789	0.805	0.821	0.837	0.853
Ca	0.017	0.017	0.015	0.012	0.015
Na	0.001	–	0.002	0.001	–
Ni	–	0.001	–	–	–
Cations	2.996	3.002	3.000	3.004	3.006
Mg/(Fe + Mg)	0.41	0.42	0.43	0.43	0.44

Mineral	Fe-Ti oxide								
Pluton	Bozqush						Kaleybar		
Rock type	NeSy						Cpy		
Sample no.	1	2	3	4	5	6	1	2	3
Wt.%									
SiO_2	0.13	0.27	0.03	0.04	0.02	0.02	0.02	0.00	0.02
TiO_2	8.78	19.97	7.82	52.04	52.11	52.11	2.80	4.42	2.67
Al_2O_3	2.19	1.32	2.25	0.12	0.12	0.10	1.18	2.79	1.48
FeO	83.11	70.88	82.88	44.91	45.10	44.48	88.07	85.34	87.77
MnO	1.13	2.04	1.08	3.28	3.29	3.29	0.30	0.47	0.30
MgO	0.27	0.41	0.24	0.69	0.68	0.65	1.30	2.68	1.41
CaO	0.03	0.01	–	–	0.01	0.02	–	–	–
Na_2O	0.03	0.01	–	–	0.02	0.01	–	–	–
NiO	–	–	–	–	–	0.02	–	–	–
Total	95.68	94.91	94.30	101.08	101.33	100.69	93.66	95.70	93.64
	Cations on the basis of 4 (O)			Cations on the basis of 3 (O)			Cations on the basis of 4 (O)		
Ti	0.247	0.576	0.223	0.971	0.970	0.977	0.080	0.121	0.076
Al	0.097	0.060	0.100	0.003	0.004	0.003	0.053	0.120	0.066
Fe^{3+}	1.408	0.788	1.454	0.073	0.076	0.059	1.788	1.638	1.783
Fe^{2+}	1.196	1.486	1.174	0.858	0.857	0.868	0.997	0.961	0.987
Mn	0.036	0.066	0.035	0.069	0.069	0.069	0.010	0.014	0.010
Mg	0.015	0.024	0.014	0.025	0.025	0.024	0.073	0.145	0.079
Cations	3.000	3.000	3.000	2.000	2.000	2.000	3.000	3.000	3.000

Mineral	clinopyroxene									
Pluton	Razgah			Bozqush			Kaleybar			
Rock type	PslSy			NeSy			MoGb			
Sample no.	1	2	3	1	2	3	1	2	3	4
Wt.%										
SiO_2	51.47	50.84	51.28	52.39	51.87	52.31	51.59	49.73	49.40	50.75
TiO_2	1.04	1.00	0.92	0.89	0.47	0.58	0.62	1.01	1.03	0.69
Al_2O_3	2.32	2.52	2.02	2.36	2.52	2.51	3.64	5.30	5.50	3.97
FeO	9.10	12.49	12.83	8.76	11.87	10.35	6.99	8.19	8.15	8.76
MnO	0.42	0.49	0.58	0.50	0.72	0.58	0.37	0.42	0.39	0.37
MgO	13.46	9.81	9.87	13.66	10.72	11.62	13.42	12.20	12.06	12.14
CaO	21.92	22.98	22.49	22.51	22.66	22.81	23.65	23.61	23.55	23.70
Na_2O	0.62	0.80	0.94	0.74	0.96	0.94	0.96	1.00	0.95	0.94
Total	100.35	100.92	100.98	101.83	101.80	101.71	101.27	101.46	101.02	101.34

(*continued on next page*)

Table 2 (*continued*)

Mineral	clinopyroxene									
Pluton	Razgah			Bozqush			Kaleybar			
Rock type	PslSy			NeSy			MoGb			
Sample no.	1	2	3	1	2	3	1	2	3	4
Cations on the basis of 6 (O)										
Si	1.911	1.915	1.930	1.913	1.924	1.929	1.881	1.819	1.815	1.864
Al^T	0.089	0.085	0.070	0.087	0.076	0.071	0.119	0.181	0.185	0.136
Al^{M1}	0.013	0.027	0.020	0.015	0.034	0.038	0.037	0.047	0.054	0.035
Ti	0.029	0.028	0.026	0.024	0.013	0.016	0.017	0.028	0.028	0.019
Fe^{3+M1}	0.062	0.060	0.066	0.075	0.085	0.068	0.115	0.148	0.141	0.130
Fe^{2+M1}	0.151	0.333	0.333	0.141	0.275	0.239	0.098	0.102	0.110	0.139
Mg	0.745	0.551	0.554	0.744	0.593	0.639	0.729	0.665	0.661	0.665
Fe^{2+M2}	0.070	0.000	0.005	0.051	0.008	0.013	0.000	0.000	0.000	0.000
Mn	0.013	0.016	0.019	0.015	0.023	0.018	0.011	0.013	0.012	0.012
Ca	0.872	0.927	0.907	0.881	0.900	0.902	0.924	0.925	0.927	0.933
Na	0.045	0.058	0.068	0.052	0.069	0.068	0.068	0.071	0.067	0.067
Cations	4.000	4.000	4.000	4.000	4.000	4.000	4.000	4.000	4.000	4.000
Wo	45.6	49.1	48.2	46.2	47.8	48.0	49.20	49.90	50.10	49.66
En	38.9	29.2	29.4	39.0	31.5	34.0	38.85	35.88	35.70	35.40
Fs	15.5	21.7	22.4	14.8	20.7	18.0	11.95	14.22	14.20	14.94

Mineral	amphibole									
Pluton	Kaleybar			Kaleybar			Bozqush			
Rock type	NeSy			MoGb			NeSy			
Sample no.	1	2	3	1	2	3	1	2	3	4
Wt.%										
SiO_2	37.93	37.53	37.83	38.74	38.58	38.87	38.98	39.35	39.70	39.40
TiO_2	1.75	2.32	2.61	2.63	2.56	2.57	3.29	3.64	3.62	3.70
Al_2O_3	13.09	13.27	12.93	13.58	13.48	13.58	11.99	11.84	11.99	11.93
FeO	21.36	21.60	20.75	17.78	17.85	17.71	21.25	20.10	20.20	20.37
MnO	0.96	0.99	0.94	0.49	0.46	0.45	0.60	0.62	0.57	0.54
MgO	6.68	6.62	6.79	9.03	9.09	9.07	6.45	6.79	6.92	6.78
CaO	11.62	11.55	11.53	11.92	11.85	11.87	11.55	11.66	11.59	11.53
Na_2O	2.51	2.56	2.42	2.32	2.22	2.19	2.51	2.67	2.57	2.60
K_2O	2.26	2.28	2.30	2.38	2.42	2.44	1.97	1.90	1.88	1.88
Total	98.17	98.73	98.09	98.86	98.49	98.74	98.59	98.56	99.04	98.72
Cations on the basis of 23 (O)										
Si	5.930	5.845	5.919	5.904	5.896	5.923	6.085	6.139	6.145	6.127
Al^T	2.070	2.155	2.081	2.096	2.104	2.077	1.915	1.861	1.855	1.873
Al^C	0.341	0.279	0.301	0.342	0.323	0.359	0.289	0.315	0.330	0.313
Fe^{3+}	0.165	0.182	0.077	0.075	0.130	0.087	0.000	0.000	0.000	0.000
Ti	0.206	0.272	0.308	0.302	0.294	0.294	0.387	0.427	0.421	0.433
Mg	1.557	1.538	1.583	2.052	2.071	2.060	1.502	1.578	1.597	1.571
Fe^{2+}	2.629	2.632	2.638	2.191	2.151	2.170	2.774	2.622	2.614	2.648
Mn^C	0.103	0.097	0.093	0.039	0.032	0.029	0.047	0.057	0.038	0.035
Mn^B	0.025	0.034	0.031	0.025	0.028	0.029	0.032	0.024	0.036	0.035
Ca	1.946	1.927	1.933	1.947	1.940	1.938	1.932	1.948	1.922	1.922
Na^B	0.029	0.039	0.036	0.029	0.032	0.033	0.036	0.028	0.041	0.042
Na^A	0.730	0.735	0.699	0.656	0.625	0.615	0.724	0.780	0.730	0.741
K	0.450	0.453	0.459	0.462	0.471	0.474	0.391	0.377	0.372	0.373
Cations	16.181	16.188	16.158	16.117	16.096	16.090	16.115	16.157	16.102	16.115
$Mg/(Mg + Fe^{2+})$	0.37	0.37	0.38	0.48	0.49	0.49	0.35	0.38	0.38	0.37

Mineral	plagioclase				alkali-feldspar				
Pluton	Kaleybar				Kaleybar		Bozqush		
Rock type	MoGb				MoGb		NeSy		
Sample no.	1	2	3	4	1	2	1	2	3
Wt.%									
SiO_2	58.59	59.55	56.50	56.49	63.95	63.45	65.73	65.68	65.69
TiO_2	–	0.01	0.01	0.04	0.06	0.08	0.03	0.07	0.09
Al_2O_3	26.51	25.49	27.59	27.78	19.55	21.05	19.29	19.36	19.33
FeO	0.13	0.15	0.19	0.21	0.04	0.03	0.04	0.08	0.06
MnO	0.03	–	0.02	–	–	0.02	–	0.02	0.04
BaO	0.03	0.05	0.05	–	0.72	0.90	0.25	0.25	0.20
CaO	8.59	7.56	9.98	10.03	0.84	0.47	0.55	0.49	0.57
Na_2O	6.98	7.18	5.69	5.75	1.84	1.42	3.66	3.94	3.97

(continued on next page)

Table 2 (*continued*)

Mineral	plagioclase				alkali-feldspar				
Pluton	Kaleybar				Kaleybar		Bozqush		
Rock type	MoGb				MoGb		NeSy		
Sample no.	1	2	3	4	1	2	1	2	3
K_2O	0.41	0.54	0.91	0.29	12.79	13.40	10.78	10.41	10.26
Total	101.27	100.53	100.94	100.59	99.79	100.82	100.33	100.30	100.21
Cations on the basis of 32 (O)									
Si	10.391	10.602	10.113	10.108	11.780	11.598	11.900	11.883	11.885
Al	5.537	5.344	5.816	5.854	4.241	4.531	4.113	4.125	4.119
Ti	–	0.001	0.001	0.005	0.008	0.011	0.004	0.010	0.012
Fe^{2+}	0.019	0.022	0.028	0.031	0.006	0.005	0.006	0.012	0.009
Mn	0.005	–	0.003	–	–	0.003	–	0.003	0.006
Ba	0.002	0.003	0.004	–	0.052	0.064	0.018	0.018	0.014
Ca	1.632	1.442	1.914	1.923	0.166	0.092	0.107	0.095	0.110
Na	2.400	2.479	1.975	1.995	0.657	0.503	1.285	1.382	1.393
K	0.093	0.123	0.208	0.066	3.006	3.125	2.490	2.403	2.368
Cations	20.081	20.019	20.066	19.982	19.968	19.996	19.941	19.949	19.930
X	15.928	15.947	15.930	15.967	16.029	16.140	16.017	16.018	16.016
Z	4.151	4.069	4.132	4.015	3.887	3.792	3.906	3.913	3.900
Ab	58.2	61.3	48.2	50.1	17.2	13.5	33.1	35.6	36.0
An	39.5	35.7	46.7	48.3	4.3	2.5	2.8	2.4	2.8
Or	2.3	3.0	5.1	1.7	78.5	84.0	64.1	61.9	61.2

Mineral	plagioclase		alkali-feldspar						
Pluton	Bozqush		Bozqush		Razgah				
Rock type	NeSy		NeSy		PslSy				
Sample no.	1	2	1	2	1	2	3	4	5
Wt.%									
SiO_2	61.93	61.28	64.97	64.75	64.51	64.08	64.00	64.17	64.63
TiO_2	0.06	0.04	0.02	0.02	0.10	0.04	0.09	0.06	0.06
Al_2O_3	24.08	24.39	19.00	19.29	18.62	18.82	18.52	18.62	18.70
FeO	0.16	0.20	0.11	0.11	0.05	0.06	0.07	0.09	0.10
MnO	–	0.04	0.06	0.03	0.01	0.03	0.01	–	–
BaO	0.03	–	0.13	0.35	n.a.	n.a.	n.a.	n.a.	n.a.
CaO	5.59	6.17	0.25	0.31	0.22	0.14	0.13	0.19	0.17
Na_2O	8.11	7.82	1.66	1.98	0.44	0.45	0.28	0.43	0.41
K_2O	0.56	0.52	13.96	13.77	15.82	15.81	15.92	15.76	15.93
Total	100.52	100.46	100.16	100.61	99.76	99.43	99.03	99.33	99.99
Cations on the basis of 32 (O)									
Si	10.956	10.866	11.911	11.840	11.941	11.906	11.940	11.931	11.938
Al	5.017	5.093	4.102	4.154	4.058	4.117	4.069	4.077	4.067
Ti	0.008	0.005	0.003	0.003	0.014	0.006	0.012	0.009	0.008
Fe^{2+}	0.024	0.030	0.017	0.017	0.007	0.009	0.010	0.014	0.016
Mn	–	0.006	0.009	0.005	0.001	0.004	0.002	–	–
Ba	0.002	–	0.009	0.025	–	–	–	–	–
Ca	1.060	1.172	0.049	0.061	0.043	0.027	0.027	0.038	0.034
Na	2.782	2.689	0.590	0.702	0.159	0.162	0.102	0.155	0.145
K	0.126	0.118	3.265	3.212	3.735	3.748	3.789	3.739	3.754
Cations	19.977	19.979	19.964	20.058	19.958	19.979	19.951	19.963	19.962
X	15.981	15.964	16.016	15.997	16.013	16.029	16.021	16.017	16.013
Z	3.994	4.015	3.939	4.036	3.945	3.950	3.930	3.946	3.949
Ab	70.1	67.5	15.1	17.7	4.0	4.1	2.6	3.9	3.7
An	26.7	29.5	1.3	1.5	1.1	0.7	0.7	1.0	0.9
Or	3.2	3.0	83.6	80.8	94.9	95.2	96.7	95.1	95.4

Mineral	biotite									
Pluton	Kaleybar					Bozqush				
Rock type	MoGb					NeSy				
Sample no.	1	2	3	4	5	1	2	3	4	5
Wt.%										
SiO_2	36.20	36.10	35.82	36.34	35.95	36.12	36.19	36.30	35.62	36.10
TiO_2	4.82	4.80	4.85	4.71	4.41	5.80	5.90	6.03	5.58	5.42
Al_2O_3	15.02	15.10	15.10	15.13	15.75	14.50	14.34	14.31	14.39	14.70
FeO	19.17	19.37	19.55	18.12	18.33	21.38	21.37	21.48	22.40	21.70
MnO	0.37	0.41	0.42	0.35	0.36	0.47	0.46	0.52	0.58	0.55
MgO	11.75	11.92	11.53	12.77	12.49	10.00	9.91	9.91	9.39	9.55

(*continued on next page*)

Table 2 (*continued*)

Mineral	biotite									
Pluton	Kaleybar					Bozqush				
Rock type	MoGb					NeSy				
Sample no.	1	2	3	4	5	1	2	3	4	5
CaO	0.01	0.02	0.03	0.00	0.01	0.00	0.00	0.00	0.02	0.01
Na_2O	0.20	0.23	0.21	0.20	0.17	0.40	0.43	0.37	0.38	0.42
K_2O	9.59	9.62	9.71	9.68	9.86	9.44	9.45	9.49	9.58	9.57
Total	97.13	97.57	97.22	97.30	97.33	98.11	98.05	98.41	97.94	98.02
Cations on the basis of 22 (O)										
Si	5.546	5.504	5.502	5.519	5.467	5.573	5.596	5.593	5.541	5.594
Al^{IV}	2.454	2.496	2.498	2.481	2.533	2.427	2.404	2.407	2.459	2.406
Al^{VI}	0.255	0.216	0.233	0.225	0.288	0.208	0.207	0.189	0.177	0.277
Ti	0.556	0.550	0.560	0.538	0.504	0.673	0.686	0.699	0.653	0.632
Fe^{3+VI}	0.852	0.919	0.891	0.896	0.818	0.968	0.941	0.971	0.937	0.800
Fe^{2+}	1.604	1.552	1.620	1.405	1.513	1.791	1.822	1.776	1.956	2.012
Mn	0.049	0.053	0.055	0.045	0.046	0.061	0.060	0.068	0.076	0.072
Mg	2.684	2.710	2.640	2.891	2.831	2.300	2.284	2.276	2.178	2.206
Ca	0.002	0.003	0.005	0.000	0.002	0.000	0.000	0.000	0.003	0.002
Na	0.058	0.068	0.063	0.059	0.050	0.120	0.129	0.111	0.115	0.126
K	1.874	1.871	1.903	1.875	1.913	1.858	1.864	1.865	1.901	1.892
Cations	15.934	15.942	15.970	15.934	15.965	15.979	15.993	15.955	15.997	16.019

Mineral	spinel				
Pluton	Kaleybar				
Rock type	Cpy				
Sample no.	1	2	3	4	5
Wt.%					
SiO_2	–	0.01	–	0.01	–
TiO_2	0.06	0.03	0.04	0.06	0.05
Al_2O_3	62.56	62.74	62.62	62.76	62.36
FeO	16.12	15.94	16.28	16.68	16.79
MnO	0.18	0.15	0.13	0.18	0.18
MgO	20.16	20.20	19.98	19.92	19.80
CaO	–	–	–	–	0.01
Na_2O	0.02	0.04	–	0.03	0.04
NiO	0.02	0.04	0.02	–	0.03
Total	99.12	99.15	99.07	99.64	99.26
Cations on the basis of 4 (O)					
Ti	0.001	0.001	0.001	0.001	0.001
Al	1.883	1.887	1.887	1.884	1.880
Fe^{3+}	0.115	0.112	0.112	0.114	0.118
Fe^{2+}	0.229	0.228	0.236	0.241	0.242
Mn	0.004	0.003	0.003	0.004	0.004
Ni	–	0.001	–	–	0.001
Mg	0.768	0.768	0.761	0.756	0.755
Cations	3.000	3.000	3.000	3.000	3.000
End members (mol.)					
Spinel	0.768	0.768	0.761	0.756	0.755
Hercynite	0.170	0.171	0.179	0.182	0.181
Galaxite	0.004	0.003	0.003	0.004	0.004
Trevorite	–	0.001	–	–	0.001
Magnetite	0.057	0.056	0.056	0.057	0.059
Ulvöspinel	0.001	0.001	0.001	0.001	0.001

	garnet				
	Kaleybar				
	NeSy				
	1	2	3	4	5
Wt.%					
SiO_2	36.24	36.30	35.13	35.06	34.97
TiO_2	2.54	2.11	4.16	4.35	4.63
Al_2O_3	6.06	5.91	5.51	5.31	5.40
FeO	20.10	20.90	19.81	19.60	19.55
MnO	0.84	0.81	1.19	1.15	1.13
MgO	0.28	0.28	0.32	0.31	0.33
CaO	33.16	33.18	33.08	32.76	32.87
Total	99.22	99.49	99.20	98.54	98.88
Cations on the basis of 12 (O)					
Si	2.936	2.934	2.861	2.876	2.860
Al^{T}	0.064	0.066	0.139	0.124	0.140
Al^{VI}	0.514	0.496	0.389	0.389	0.380
Fe^{3+}	1.239	1.311	1.239	1.196	1.189
Ti	0.155	0.128	0.255	0.268	0.285
Fe^{2+}	0.123	0.101	0.110	0.149	0.148
Mg	0.034	0.034	0.039	0.038	0.040
Mn	0.058	0.055	0.082	0.080	0.078
Ca	2.878	2.873	2.886	2.880	2.880
Cations	8.000	8.000	8.000	8.000	8.000
End members (mol.%)					
Almandine	3.97	3.31	3.53	4.73	4.69
Andradite	64.95	67.73	65.80	64.51	64.15
Grossular	28.13	26.05	26.79	27.01	27.39
Pyrope	1.09	1.10	1.25	1.21	1.28
Spessartine	1.86	1.81	2.63	2.54	2.49
Uvarovite	0.00	0.00	0.00	0.00	0.00

Abbreviations: Cpy, clinopyroxenite; MoGb, monzo-gabbro; NeSy, Nepheline Syenite; PslSy, Pseudoleucite Syenite; n.a., not analyzed; and "-" means "under the detection limit".

the alkali-feldspars is 2 mol. %. The Ab contents range from 15 to 36 mol. %. The average composition of the alkali-feldspars from the Kaleybar monzo-gabbro and the Razgah pseudoleucite syenite are Or_{82} Ab_{15} An_3 and Or_{96} Ab_3 An_1, respectively. The plagioclase composition ranges from Ab_{55} An_{42} Or_3 for the Kaleybar monzo-gabbro to Ab_{69} An_{28} Or_3 for the Bozqush nepheline syenite (Fig. 6d).

6.6. Biotite

Based on the International Mineralogical Association (IMA) classification scheme, the mica compositions plot between the siderophyllite and eastonite end members as Mg-biotite in the Kaleybar alkali-gabbro to Fe-biotite in the Bozqush nepheline syenite (Fig. 6b). Based on their FeO, MnO, MgO, TiO_2, and Al^{VI} content, they are primary magmatic biotites.

Table 3
Representative whole rock analyses of the KRB main rocks.

Pluton	Kaleybar								
Rock type	NeSy					MoGb			QzMo
Sample no.	10	13	40	54	63	2	5	21	KB26
Wt.%									
SiO_2	57.6	55	59.9	58.2	55.2	48.1	47.7	47.8	60.1
TiO_2	0.40	0.12	0.33	0.38	0.39	0.93	0.99	0.74	0.45
Al_2O_3	18.70	23.20	19.85	19.25	19.60	17.90	17.70	17.70	16.75
Fe_2O_3(t)	3.55	1.36	2.34	2.84	4.26	9.58	10.8	9	4.34
MnO	0.12	0.10	0.1	0.13	0.17	0.19	0.22	0.17	0.13
MgO	0.81	0.05	0.39	0.55	1.04	3.95	4.61	4.08	2.17
CaO	3.83	1.64	2.6	3.04	3.96	10.05	10.15	10.25	5.12
Na_2O	4.78	8.70	3.94	4.93	5.14	2.98	3.50	3.27	4.08
K_2O	8.53	7.63	9.38	7.91	7.36	3.05	2.85	2.04	3.80
P_2O_5	0.21	0.01	0.09	0.15	0.25	0.51	0.48	0.57	0.26
SrO	0.21	0.01	0.12	0.15	0.12	0.13	0.09	0.16	0.07
BaO	0.27	< 0.01	0.13	0.14	0.11	0.14	0.07	0.11	0.12
LOI	0.88	2.09	1.08	1.43	1.51	0.70	0.85	0.34	0.71
Total	99.90	99.90	100.5	99.10	99.10	98.20	100.00	96.20	98.10
ppm									
Ba	2330	15.50	1140	1135	706	1300	615	993	1100
Rb	234	242	205	193.5	164.5	47.8	42.2	34	82.2
Sr	1775	58.6	1125	1180	804	1125	818	1385	630
Y	15.7	18.1	18.4	18.5	16.2	21.7	22.9	22.9	18.7
Zr	90	306	130	142	144	56	98	78	132
Nb	9	11.7	13.4	15.4	12.1	3.3	5.9	3.7	7.9
Th	8.34	25.6	11.95	15.15	17	3.29	5.04	5.39	10.5
Pb	28	33	31	34	27	10	13	14	12
Ga	14.9	23	15.1	15.9	14.5	17.8	18.7	18.6	17.9
Zn	72	60	59	76	77	95	125	83	51
Cu	128	12	20	34	41	46	69	180	13
Ni	< 5	5	8	12	< 5	7	10	12	6
V	105	35	73	78	100	313	378	289	101
Cr	< 10	< 10	10	10	< 10	< 10	10	10	10
Hf	2.2	6.7	3.2	3.5	3.6	1.6	2.9	2.4	3.6
Cs	7.24	13.85	2.53	5.80	7.39	0.61	1.06	1.08	0.80
Ta	0.7	0.5	1.2	1.0	0.7	0.3	0.5	0.3	0.6
Co	7.1	0.8	3.1	4.8	6.4	31.5	34.2	29.1	12.5
U	2.77	8.79	2.3	4.06	4.13	0.82	1.15	1.46	3.06
W	4	2	4	4	5	1	2	1	1
Mo	5	< 2	< 2	3	4	< 2	< 2	2	2
La	36.3	58.9	39.4	57.3	47.2	24.8	28.7	27.4	32.7
Ce	66.4	83.4	69.9	97.6	81.3	44.7	53.2	51.5	51.5
Pr	7.8	7.58	8.12	10.40	8.5	5.63	6.24	6.38	5.33
Nd	30.9	23	31.1	36.9	29.5	24.2	25.4	26.9	19.7
Sm	5.94	3.50	6.02	6.27	5.18	5.58	5.47	5.97	3.69
Eu	2.07	0.64	1.82	1.76	1.19	1.82	1.59	1.93	1.12
Gd	5.36	3.62	5.65	6.07	4.98	5.72	5.63	5.79	3.71
Tb	0.70	0.45	0.74	0.76	0.61	0.81	0.82	0.82	0.56
Dy	3.35	2.38	3.86	3.70	3.15	4.34	4.45	4.56	3.21
Ho	0.58	0.49	0.7	0.68	0.58	0.80	0.88	0.86	0.64
Er	1.69	1.77	1.99	1.93	1.81	2.29	2.59	2.53	1.97
Tm	0.24	0.32	0.26	0.28	0.24	0.34	0.35	0.39	0.33
Yb	1.34	2.36	1.89	1.65	1.80	1.90	2.37	2.24	2.23
Lu	0.20	0.42	0.26	0.26	0.26	0.29	0.35	0.34	0.39
Sum REE	163	189	172	226	186	123	138	138	127
Eu/Eu*	1.12	0.55	0.95	0.87	0.72	0.98	0.88	1.00	0.93
$(La/Sm)_N$	3.84	10.59	4.12	5.75	5.73	2.80	3.30	2.89	5.57
$(La/Yb)_N$	18.26	16.83	14.05	23.41	17.68	8.80	8.16	8.25	9.89
$(Tb/Yb)_N$	2.30	0.84	1.73	2.03	1.49	1.88	1.53	1.61	1.11
ASI	0.79	0.91	0.93	0.87	0.84	0.69	0.66	0.69	0.85
K/Rb	303	262	380	339	371	530	561	498	384
Mg#	0.31	0.07	0.24	0.28	0.35	0.45	0.46	0.48	0.50

Pluton	Kaleybar						
Rock type	Sy					MoDi	Cpy
Sample no.	27	41	48	58	59	45	KP3
Wt.%							
SiO_2	55.4	58.6	59	56.6	60.7	51.30	41.90
TiO_2	0.60	0.36	0.29	0.30	0.47	0.60	1.34

(*continued on next page*)

Table 3 (*continued*)

Pluton	Kaleybar						
Rock type	Sy					MoDi	Cpy
Sample no.	27	41	48	58	59	45	KP3
Al_2O_3	18.45	19.05	19.05	19.45	19.80	18.50	6.84
Fe_2O_3(t)	4.21	2.55	2.05	4	2.03	6.3	17
MnO	0.25	0.09	0.07	0.13	0.09	0.13	0.19
MgO	1.20	0.60	0.48	0.96	0.30	2.37	12.25
CaO	4.30	3.32	2.75	4.06	2.14	7.95	18.85
Na_2O	3.53	3.15	2.93	3.72	4.28	2.40	0.30
K_2O	7.42	8.88	9.40	7.60	9.06	5.82	0.08
P_2O_5	0.25	0.17	0.11	0.23	0.07	0.70	0.03
SrO	0.15	0.18	0.16	0.16	0.06	0.29	0.01
BaO	0.13	0.22	0.18	0.14	0.02	0.34	< 0.01
LOI	2.24	1.31	1.56	1.69	1.21	1.26	0.59
Total	98.10	98.50	98.00	99.00	100.00	98.00	99.40
ppm							
Ba	1130	1825	1660	1110	199.5	3250	24.2
Rb	181.5	162	172	176	215	120	1.6
Sr	1225	1505	1495	1325	548	2700	102
Y	32.2	15.8	15.9	9.6	24.5	24.6	15.5
Zr	155	94	87	124	120	96	39
Nb	23.9	9.6	10.1	9.7	23.6	8.3	0.3
Th	12.4	8.75	7.68	10.65	10.55	9.06	0.19
Pb	30	25	27	30	37	19	493
Ga	17.2	13.5	13.8	16	15.2	16.6	15.3
Zn	103	50	46	77	65	80	111
Cu	55	36	28	42	37	216	20
Ni	15	< 5	< 5	< 5	< 5	10	30
V	143	74	60	112	68	207	523
Cr	20	< 10	10	< 10	< 10	10	10
Hf	4.5	2.4	2.3	2.8	3.1	2.7	1.9
Cs	9.65	2.05	2.41	4.81	2.03	2.13	0.22
Ta	1.7	0.9	0.9	0.6	1.7	0.6	0.1
Co	9.3	5	3.4	6.7	2.8	20.9	61
U	2.71	2.27	2.34	4.21	3.28	2.64	0.06
W	3	3	5	5	5	4	1
Mo	3	2	2	3	3	3	< 2
La	79.1	44.6	31.4	40	57.8	47.1	2.40
Ce	155	62.6	59.8	63.9	117	91.5	10.2
Pr	17.9	7.57	7.29	6.44	13.75	11.45	2.02
Nd	67.1	29.7	29.6	22.4	51	48.8	11.10
Sm	11.55	5.89	5.87	3.65	9.15	10.05	3.81
Eu	2.84	1.86	2.02	1.12	1.97	3.02	1.17
Gd	10.60	5.17	5.26	3.75	8.47	9.08	4.00
Tb	1.42	0.64	0.68	0.43	1.09	1.14	0.69
Dy	6.78	3.19	3.35	2.07	5.46	5.41	3.81
Ho	1.17	0.59	0.58	0.36	0.98	0.98	0.71
Er	3.51	1.73	1.68	1.00	2.60	2.69	1.81
Tm	0.51	0.25	0.23	0.13	0.32	0.37	0.26
Yb	2.95	1.37	1.34	0.87	2.00	2.18	1.41
Lu	0.43	0.21	0.19	0.13	0.23	0.29	0.21
Sum REE	361	165	149	146	272	234	44
Eu/Eu*	0.78	1.03	1.11	0.93	0.68	0.97	0.92
$(La/Sm)_N$	4.31	4.76	3.36	6.89	3.97	2.95	0.40
$(La/Yb)_N$	18.08	21.95	15.80	31.00	19.48	14.57	1.15
$(Tb/Yb)_N$	2.12	2.06	2.24	2.18	2.40	2.31	2.16
ASI	0.86	0.92	0.96	0.91	0.96	0.78	0.20
K/Rb	339	455	454	359	350	403	415
Mg#	0.36	0.31	0.31	0.33	0.22	0.43	0.59

Pluton	Razgah							
Rock type	PslSy					monzonite		
Sample no.	11	17	2	45	5	37	39	41
Wt.%								
SiO_2	56.20	56.00	55.90	55.70	56.10	51.60	55.30	52.90
TiO_2	0.41	0.42	0.42	0.44	0.40	0.64	0.62	0.54
Al_2O_3	19.90	20.10	19.15	19.15	19.90	19.40	19.00	20.60
Fe_2O_3(t)	2.76	3.04	2.73	2.6	2.7	5.16	4.88	4.88
MnO	0.07	0.07	0.07	0.07	0.07	0.11	0.12	0.10
MgO	0.68	1.21	0.77	0.72	0.71	2.46	1.86	2.01

(*continued on next page*)

Table 3 (*continued*)

Pluton	Razgah							
Rock type	PslSy					monzonite		
Sample no.	11	17	2	45	5	37	39	41
CaO	2.46	2.15	2.26	2.50	2.38	7.33	4.94	6.58
Na_2O	3.88	3.42	4.16	4.63	3.95	3.62	4.04	3.86
K_2O	10.50	10.10	9.10	10.30	10.05	5.00	6.74	5.59
P_2O_5	0.43	0.44	0.43	0.53	0.42	1.12	0.84	0.84
SrO	0.05	0.05	0.05	0.06	0.05	0.13	0.08	0.14
BaO	0.12	0.12	0.11	0.13	0.12	0.10	0.15	0.20
LOI	2.44	2.87	3.09	1.45	2.59	1.47	1.52	1.71
Total	99.90	100.00	98.20	98.30	99.40	98.10	100.00	100.00
ppm								
Ba	1030	1045	1005	1130	1035	931	1300	1770
Rb	370	360	311	417	343	146	164	107
Sr	467	429	436	524	454	1205	712	1210
Y	16.8	16.7	18.1	20.9	17.8	26	31.3	22.1
Zr	114	119	126	157	126	104	199	129
Nb	8.6	8.9	9.6	12.9	9.3	7.6	14.7	8.8
Th	6.58	5.88	7.24	9.43	7.75	6.36	12.65	8.07
Pb	14	16	16	13	16	14	20	16
Ga	15.3	15.2	14.5	15.3	15.6	17	17.4	17.2
Zn	47	48	50	43	42	64	73	63
Cu	117	118	118	28	114	337	194	126
Ni	< 5	< 5	< 5	< 5	< 5	22	7	18
V	63	64	58	64	57	189	122	116
Cr	< 10	< 10	< 10	< 10	< 10	10	< 10	10
Hf	2.8	3	3.2	3.9	3.1	2.8	5.1	3.2
Cs	9.22	9.41	12.10	10.25	10.25	3.65	5.28	2.76
Ta	0.7	0.7	0.8	0.9	0.7	0.6	1	0.7
Co	4.1	4.7	4.2	3.8	3.9	13.5	9.9	11.6
U	2.02	2.01	2.30	3.19	2.49	2.21	4.09	2.74
W	2	6	4	3	3	2	4	3
Mo	< 2	< 2	< 2	< 2	< 2	< 2	2	< 2
La	29.7	38.9	31.8	36.2	30.1	41.6	52.9	37.5
Ce	55.4	54.3	59.8	67.4	56.5	81.7	99.6	71.1
Pr	6.40	6.34	6.99	7.81	6.60	10	11.55	8.43
Nd	24.9	24.3	26.3	29.7	25.1	41	44	33.7
Sm	4.57	4.46	4.90	5.34	4.63	8.09	8.18	6.29
Eu	1.08	1.07	1.11	1.30	1.13	1.83	1.72	1.76
Gd	4.30	4.31	4.75	5.38	4.52	7.45	8.06	6
Tb	0.61	0.59	0.62	0.73	0.59	1.02	1.09	0.80
Dy	3.27	3.26	3.46	3.93	3.31	5.18	5.90	4.24
Ho	0.63	0.64	0.68	0.77	0.66	0.99	1.14	0.83
Er	1.91	1.90	2.05	2.40	2.03	2.87	3.55	2.44
Tm	0.26	0.26	0.28	0.32	0.27	0.38	0.50	0.33
Yb	1.81	1.74	2.00	2.23	1.91	2.51	3.41	2.23
Lu	0.25	0.26	0.28	0.33	0.27	0.35	0.49	0.30
Sum REE	135	142	145	164	138	205	242	176
Eu/Eu*	0.74	0.75	0.70	0.74	0.76	0.72	0.65	0.88
$(La/Sm)_N$	4.09	5.49	4.08	4.26	4.09	3.23	4.07	3.75
$(La/Yb)_N$	11.06	15.07	10.72	10.94	10.62	11.17	10.46	11.34
$(Tb/Yb)_N$	1.49	1.50	1.37	1.44	1.36	1.79	1.41	1.58
ASI	0.92	1.01	0.94	0.84	0.94	0.83	0.87	0.88
K/Rb	236	233	243	205	243	284	341	432
Mg#	0.33	0.44	0.36	0.35	0.34	0.49	0.43	0.45

Pluton	Bozqush									
Rock type	syenite						monzonite			
Sample no.	16	21	49	36	4	44	46	50	55	9
Wt.%										
SiO_2	56.60	57.00	53.90	56.80	57.60	57.20	57.70	53.80	55.90	56.30
TiO_2	0.58	0.56	0.71	0.64	0.49	0.64	0.89	0.68	0.71	0.63
Al_2O_3	19.90	19.58	19.40	18.95	19.60	18.80	16.60	19.35	18.45	19.75
Fe_2O_3(t)	3.67	3.42	4.5	4.25	3.15	4.17	4.67	4.79	4.14	3.86
MnO	0.09	0.08	0.10	0.10	0.08	0.10	0.11	0.11	0.09	0.10
MgO	1.04	1.08	1.62	1.33	0.91	1.26	1.56	1.98	1.70	1.14
CaO	3.73	3.65	5.66	3.77	3.29	3.32	3.15	5.96	4.13	4.23
Na_2O	4.87	4.70	4.78	3.93	4.78	4.14	3.12	4.91	3.89	4.08
K_2O	6.54	6.63	5.20	7.01	6.90	7.56	8.33	5.19	7.05	6.70
P_2O_5	0.40	0.43	0.61	0.62	0.38	0.59	0.67	0.68	0.88	0.46

(*continued on next page*)

Table 3 (*continued*)

Pluton	Bozqush									
Rock type	syenite						monzonite			
Sample no.	16	21	49	36	4	44	46	50	55	9
SrO	0.10	0.10	0.10	0.09	0.09	0.08	0.05	0.10	0.10	0.11
BaO	0.13	0.15	0.11	0.15	0.13	0.16	0.14	0.11	0.27	0.15
LOI	0.84	0.50	1.28	0.92	0.66	0.56	1.25	1.36	0.74	1.29
Total	98.50	98.20	98.00	98.60	98.10	98.60	98.20	99.00	98.10	98.80
ppm										
Ba	1190	1340	1060	1395	1195	1435	1285	1035	2440	1365
Rb	174.5	130.5	146	181.5	144	203	221	155.5	171.5	201
Sr	857	844	903	861	806	727	447	845	927	944
Y	20.1	18.5	21.6	24.6	19.4	22.9	31.7	20.6	23.5	20.8
Zr	170	143	162	151	158	136	237	139	100	185
Nb	16.6	14.2	14.3	13	13.7	11.9	21.8	10.6	8.6	15.7
Th	11	7.99	9.15	8.82	8.93	8.51	13.1	8.28	6.8	11.3
Pb	20	19	19	18	19	19	20	15	16	19
Ga	19.3	18	18.8	17.5	18.7	17	17.9	19.1	16.2	18.5
Zn	59	53	75	61	50	59	78	68	53	59
Cu	89	68	247	96	60	90	239	42	147	87
Ni	8	5	8	7	8	20	< 5	15	6	6
V	62	68	110	88	61	101	103	119	143	67
Cr	< 10	< 10	10	< 10	10	40	< 10	10	< 10	< 10
Hf	4.2	3.5	4.2	3.7	3.8	3.5	6	3.6	2.4	4.6
Cs	4.71	2.16	3.95	7.95	3.81	6.17	4.35	5.45	4.07	7.13
Ta	1.1	0.9	0.9	0.8	0.9	0.8	1.4	0.7	0.6	1
Co	7.3	6.6	10.4	8	5.9	7.6	8.3	12.5	9.8	7.3
U	3.69	2.58	2.99	2.94	2.86	2.82	4.02	2.60	2.19	4.19
W	4	2	4	4	2	2	3	4	2	3
Mo	2	2	5	2	2	2	6	4	< 2	2
La	41.2	37.2	38	47.3	38.9	40.5	57.2	38.5	42.1	52.6
Ce	72.9	67.3	71	84.3	68.6	77.4	102.5	69.7	79.7	76.2
Pr	8.17	7.62	8.19	9.70	7.67	9.07	11.70	7.91	9.54	8.68
Nd	30.7	28.6	31	37.6	28.7	34.7	44.1	30.8	38.2	32.6
Sm	5.33	5.02	5.73	6.66	4.93	6.51	8.04	5.67	7.11	5.68
Eu	1.40	1.45	1.64	1.66	1.45	1.66	1.81	1.54	2.13	1.43
Gd	4.92	4.61	5.66	6.37	4.68	5.65	8.02	5.34	6.57	5.29
Tb	0.68	0.65	0.75	0.86	0.67	0.80	1.09	0.72	0.90	0.71
Dy	3.71	3.42	4.07	4.59	3.67	4.23	6.05	3.82	4.51	3.86
Ho	0.72	0.64	0.77	0.87	0.70	0.83	1.17	0.74	0.86	0.74
Er	2.30	2.02	2.39	2.64	2.15	2.46	3.54	2.29	2.56	2.40
Tm	0.35	0.30	0.35	0.40	0.34	0.38	0.56	0.32	0.36	0.36
Yb	2.20	1.96	2.30	2.29	2.11	2.26	3.53	2.08	2.10	2.30
Lu	0.34	0.28	0.36	0.37	0.31	0.35	0.57	0.32	0.32	0.33
Sum REE	175	161	172	206	165	187	250	170	197	193
Eu/Eu*	0.84	0.92	0.88	0.78	0.92	0.84	0.69	0.86	0.95	0.80
$(La/Sm)_N$	4.86	4.66	4.17	4.47	4.96	3.91	4.48	4.27	3.72	5.83
$(La/Yb)_N$	12.63	12.80	11.14	13.93	12.43	12.08	10.92	12.48	13.52	15.42
$(Tb/Yb)_N$	1.36	1.46	1.44	1.66	1.40	1.56	1.36	1.53	1.89	1.36
ASI	0.93	0.93	0.84	0.94	0.94	0.93	0.87	0.82	0.90	0.94
K/Rb	311	422	296	321	398	309	313	277	341	277
Mg#	0.36	0.38	0.42	0.38	0.36	0.38	0.40	0.45	0.45	0.37

Pluton	Bozqush		
Rock type	PslSy	NeSy	
Sample no.	60	31	63
Wt.%			
SiO_2	57.20	57.40	59.20
TiO_2	0.35	0.44	0.51
Al_2O_3	20.20	20.00	19.25
Fe_2O_3(t)	2.3	2.35	3.11
MnO	0.06	0.05	0.09
MgO	0.52	0.58	1.06
CaO	1.80	2.58	2.86
Na_2O	3.88	4.16	4.97
K_2O	10.50	9.16	7.94
P_2O_5	0.31	0.25	0.53
SrO	0.03	0.07	0.06
BaO	0.07	0.10	0.13
LOI	2.60	0.82	0.49
Total	99.80	98.00	100

(*continued on next page*)

Table 3 (*continued*)

Pluton	Bozqush		
Rock type	PslSy	NeSy	
Sample no.	60	31	63
ppm			
Ba	641	908	1185
Rb	411	325	164
Sr	295	631	559
Y	14.7	14.7	28.1
Zr	97	122	240
Nb	7.9	11.8	16.8
Th	5.82	6.64	13.30
Pb	13	17	24
Ga	16.6	17.9	17.9
Zn	38	42	50
Cu	71	89	65
Ni	< 5	7	6
V	32	50	63
Cr	< 10	10	10
Hf	2.5	3.2	5.9
Cs	11.3	8.39	3.51
Ta	0.6	0.8	1.1
Co	2.8	4.2	4.6
U	1.94	2.52	4.38
W	2	4	4
Mo	< 2	2	2
La	25.9	41	48.8
Ce	47.1	51.4	90.6
Pr	5.49	5.77	10.20
Nd	20.5	21.2	38.4
Sm	3.68	3.81	7.02
Eu	0.93	1.11	1.56
Gd	3.63	3.40	6.51
Tb	0.49	0.48	0.95
Dy	2.80	2.66	5.03
Ho	0.52	0.49	0.97
Er	1.61	1.68	3.15
Tm	0.27	0.26	0.50
Yb	1.59	1.60	3.20
Lu	0.24	0.24	0.50
Sum REE	115	135	217
Eu/Eu*	0.78	0.94	0.71
$(La/Sm)_N$	4.43	6.77	4.37
$(La/Yb)_N$	10.98	17.28	10.28
$(Tb/Yb)_N$	1.36	1.32	1.31
ASI	0.98	0.95	0.90
K/Rb	212	234	402
Mg#	0.31	0.32	0.40

Abbreviation: LOI, loss on ignition; Fe_2O_3 (t), total iron as Fe_2O_3; Mg# calculated as molar Mg/(Mg + Fe); MoGb, monzo-gabbro; QzMo, quartz monzonite; Sy, syenite; MoDi, monzo-diorite; Cpy, clinopyroxenite; others same as Table 1.

6.7. Garnet

The Kaleybar garnets are Ti-andradites and melanites (Table 2). The chemical zoning is characterized by a decrease in mole percent grossular, almandine, and spessartine and an increase in andradite from core to rim. The main substitution of the Kaleybar garnets is Ti-Si exchange in the tetrahedral site (Ashrafi et al., 2009a).

7. Whole rock geochemistry

Major and trace element compositions of 37 representative samples collected from the KRB plutons are given in Table 3, including 16, 8 and 13 samples from the Kaleybar, Razgah and Bozqush plutons, respectively (Fig. 2). Although the mineral assemblage and the mineral chemistry may differ between the intrusions, we present the whole-rock geochemistry as a whole due to the lack of significant difference. The rock type names in Table 3 are based on the TAS diagram (Fig. 7a).

7.1. Major elements and classification

SiO_2 ranges from 47.7 to 60.7 wt.% in the KRB samples, not including the clinopyroxenite (KP3) sample. Also, they have 2.04–10.5 wt.% K_2O, 2.4–8.7 wt.% Na_2O, 16.6–23.2 wt.% Al_2O_3, 1.64–10.25 wt.% CaO, 0.3–4.61 wt.% MgO, 0.01–1.12 wt.% P_2O_5 and 0.49–3.09 wt.% LOI. K_2O and P_2O_5 contents reach the highest concentrations in the Razgah samples, while those of the Kaleybar contain the highest contents of Na_2O, Al_2O_3 and MgO. The Mg# (~0.6), CaO, MgO, $Fe_2O_3^{tot}$, and TiO_2 contents are the highest for the Kaleybar clinopyroxenite compared to the other samples.

Based on the total alkalis ($K_2O + Na_2O$) wt.% vs. SiO_2 wt.% (TAS) nomenclature diagram (Middlemost, 1994) and the IUGS recommendation (Le Maitre et al., 2002), the Kaleybar pluton mostly consists of foid syenite, syenite, monzo-gabbro, monzo-diorite, quartz monzonite (KB26), and clinopyroxenite (KP3); the Razgah pluton mostly consists of foid syenite and monzonite; and the Bozqush pluton mostly consists of foid syenite, syenite, and monzonite. According to the TAS classification diagram of Le Bas et al. (1986) (Fig. 7a), most of the

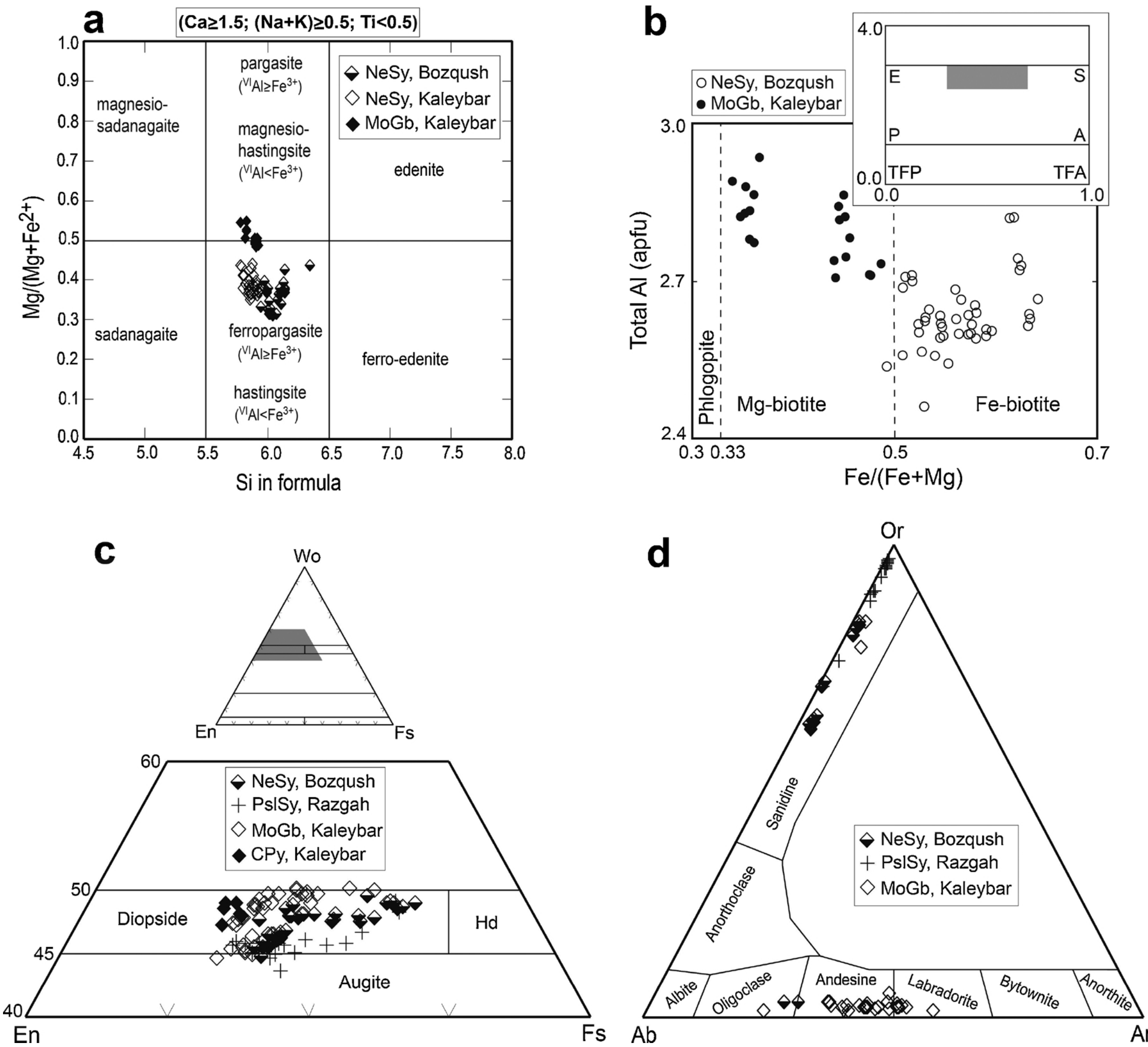

Fig. 6. Chemical classification diagrams for some minerals; (a) amphibole classification diagram (Leake et al., 1997), (b) plot of micas in the Al vs. Fe/(Fe + Mg) diagram (shaded in inset) (Rieder et al., 1998; Deer et al., 1992), (c) Enestatite-Ferrosilite-Wollastonite (En-Fs-Wo) diagram (Morimoto, 1989) for clinopyroxenes (shaded in inset), (d) Feldspars composition on the Albite-Anorthite-Orthoclase (Ab-An-Or) triangle. Abbreviations: A, annite; E, eastonite; Hd, hedenbergite; P, phlogopite; S, sidrophyllite; TFA, tetra-ferri-annite; TFP, tetra-ferri-phlogopite.

studied samples plot in the alkaline field and show a compositional trend from basic to intermediate (including monzo-gabbro to monzonite, syenite and foid-syenite), with the exception of the clinopyroxenite (KP3) and the quartz monzonite (KB26).

None of the samples can be considered “ultra-potassic” according to the criteria defined by Foley et al. (1987) with $K_2O/Na_2O > 2$, $K_2O > 3$wt.%, and $MgO > 3$wt.% (Fig. 7b). However, all of the samples (except for clinopyroxenite, KP3) show shoshonitic affinities (Fig. 7c, d; Morrison, 1980) and belong to shoshonite series, according to the diagram of SiO_2 versus K_2O (Peccerillo and Taylor, 1976; not shown). They are characterized by high total alkalis (> 5wt.%), high K_2O/Na_2O (> 0.6 at 50 wt.% SiO_2, > 1 at 55wt.% SiO_2 (Fig. 7c)), and low TiO_2 < 1.3wt.% (Fig. 7d).

Frost et al. (2001) proposed a modified alkali-lime index (MALI) to discriminate between calcic, calc-alkalic, alkali-calcic, and alkalic series. According to MALI, ($Na_2O + K_2O$)-CaO versus SiO_2 diagram (Fig. 7e), almost all of the samples plot in the alkalic field, except for the quartz-monzonite (KB26) which falls in the alkali-calcic field.

The aluminum-saturation index (ASI) is defined as molecular Al/(Ca-1.67P + Na + K) and separates rocks into metaluminous (ASI < 1) and peraluminous (ASI > 1) varieties (Frost and Frost, 2008; Frost et al., 2001; Zen, 1988). Plot of the samples in ASI versus Al/Na + K (A/NK) diagram (Fig. 7f) show that all of the samples are metaluminous (ASI < 1, Na + K < Al).

7.2. Major element fractionation trends

The KRB rocks have a range of composition from ~42 to ~61 wt.% SiO_2, corresponding to a variation from clinopyroxenite to syenite. In Harker major element diagrams, CaO (Fig. 8a), MgO (Fig. 8b), TiO_2 (Fig. 8c), and $Fe_2O_3^{tot}$ (not shown) decrease with increasing SiO_2, whereas K_2O (Fig. 8d) increase with increasing SiO_2. There is considerable scatter in the diagrams of Na_2O (Fig. 8e) and Al_2O_3 (not shown) versus SiO_2. P_2O_5 trend (Fig. 8f) with increasing SiO_2 is first ascending and then descending, likely related to the onset of apatite crystallization.

Harker variation diagrams show the linear trend displayed with a wide silica gap (~42–48 wt.% SiO_2) between clinopyroxenite and monzo-gabbros and a narrow silica gap (~48–51 wt.% SiO_2) between monzo-gabbros and foid-syenites. These patterns are consistent with magmatic crystallization and fractionation.

7.3. Trace element fractionation trends

In Harker trace element diagrams, compatible trace elements (i.e. V, Co; Fig. 9a, b) display negative trends with SiO_2 while Rb (Fig. 9c) and

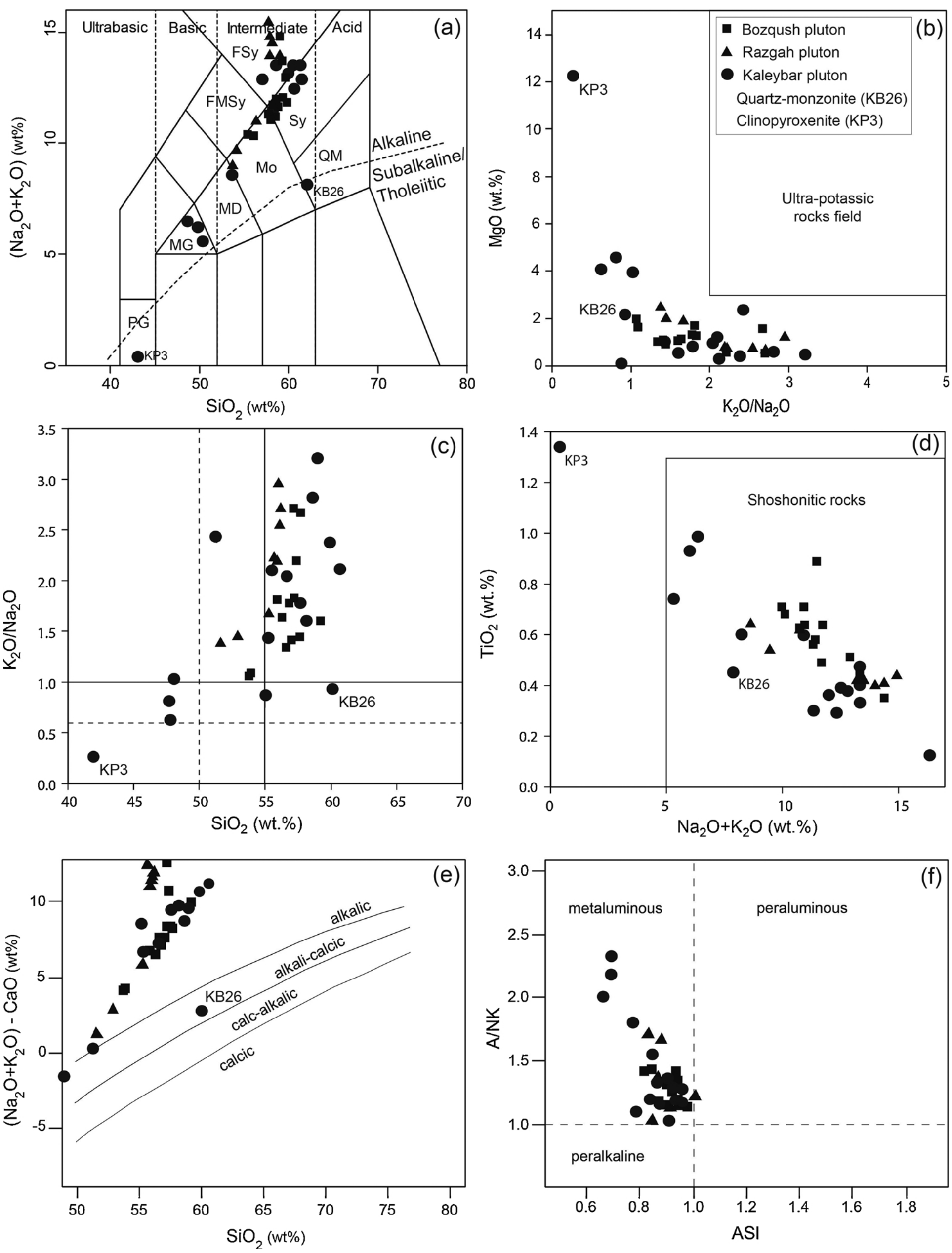

Fig. 7. Geochemical classification of studied rocks; (a) Total Alkali versus SiO_2 (TAS) (Le Bas et al., 1986; Middlemost, 1994), (b) K_2O/Na_2O versus MgO (Foley et al., 1987), (c) SiO_2 versus K_2O/Na_2O, shoshonitic rocks are characterized by $K_2O/Na_2O > 0.6$ at 50 wt.% SiO_2 (dashed lines) and $K_2O/Na_2O > 1$ at 55 wt.% SiO_2 (solid lines) (Morrison, 1980), (d) $Na_2O + K_2O$ versus TiO_2 (Morrison, 1980), (e) SiO_2 versus $(Na_2O + K_2O)$-CaO and (f) ASI versus A/NK diagram (Frost and Frost, 2008); Abbreviations: FMSy, nepheline/pseudoleucite monzosyenite; FSy, nepheline/pseudoleucite syenite; MD, monzo-diorite; MG, monzo-gabbro; Mo, monzonite; PG, peridot-gabbro; QM, quartz monzonite.

Zr (Fig. 9d) slightly show positive trends with SiO_2. The diagrams of Ba (Fig. 9e) and Sr (Fig. 9f) versus SiO_2 define scattered trends. The K_2O versus Rb diagram displays positive trends (not shown). Nickel and Cr are rather low, even in the most mafic samples (clinopyroxenite and monzo-gabbro).

7.4. Multi-element patterns

Incompatible trace element concentrations normalized against primordial mantle (Wood et al., 1979) are plotted in Fig. 10. Fig. 10a, b, and c show that the main rocks of the KRB have similar multi-element profiles. These patterns are characterized by significant enrichments in all the large ion lithophile elements (LILE), Rb, Ba, Th, U, K, and the LREE, relative to the high field strength elements (HFSE), Ta, Nb, Ti, Zr, Hf, Y, and heavy rare earth elements (HREE). The rocks exhibit negative anomalies in Ta, Nb, P, Zr, Hf, and Ti. The patterns all show strong positive anomalies for K, except for the clinopyroxenite and quartz-monzonite samples. Clinopyroxenite shows negative Ti, Rb, Nb, and P anomalies (Fig. 10d).

7.5. REE patterns

Chondrite-normalised rare earth element (REE) patterns are illustrated in Fig. 11. They are frequently LREE-enriched relative to the HREE with small to substantial negative Eu anomalies (Fig. 11a). Some samples of the Kaleybar pluton (nepheline syenite, KB10; syenite, KB48) show small positive Eu anomalies. The Eu/Eu*, $[Eu/Eu^* = Eu_N/\sqrt{(Sm)_N*(Gd)_N}]$ ratio varies from 0.55 to 1.12 and the $(La/Yb)_N$, $(La/Sm)_N$, and $(Tb/Yb)_N$ ratios are 8.2–31.0, 2.8–10.6, and 0.84–2.4, respectively. The HREE from Ho to Lu display nearly a flat pattern (Fig. 11c, d). The Kaleybar clinopyroxenite exhibits a different REE pattern with Eu/Eu* = 0.92, $(La/Yb)_N = 1.15$, $(La/Sm)_N = 0.4$, and $(Tb/Yb)_N = 2.16$ (Fig. 11b).

8. Discussion

8.1. Fractional crystallization and crustal contamination

The composition of pyroxenes and amphiboles varies according to

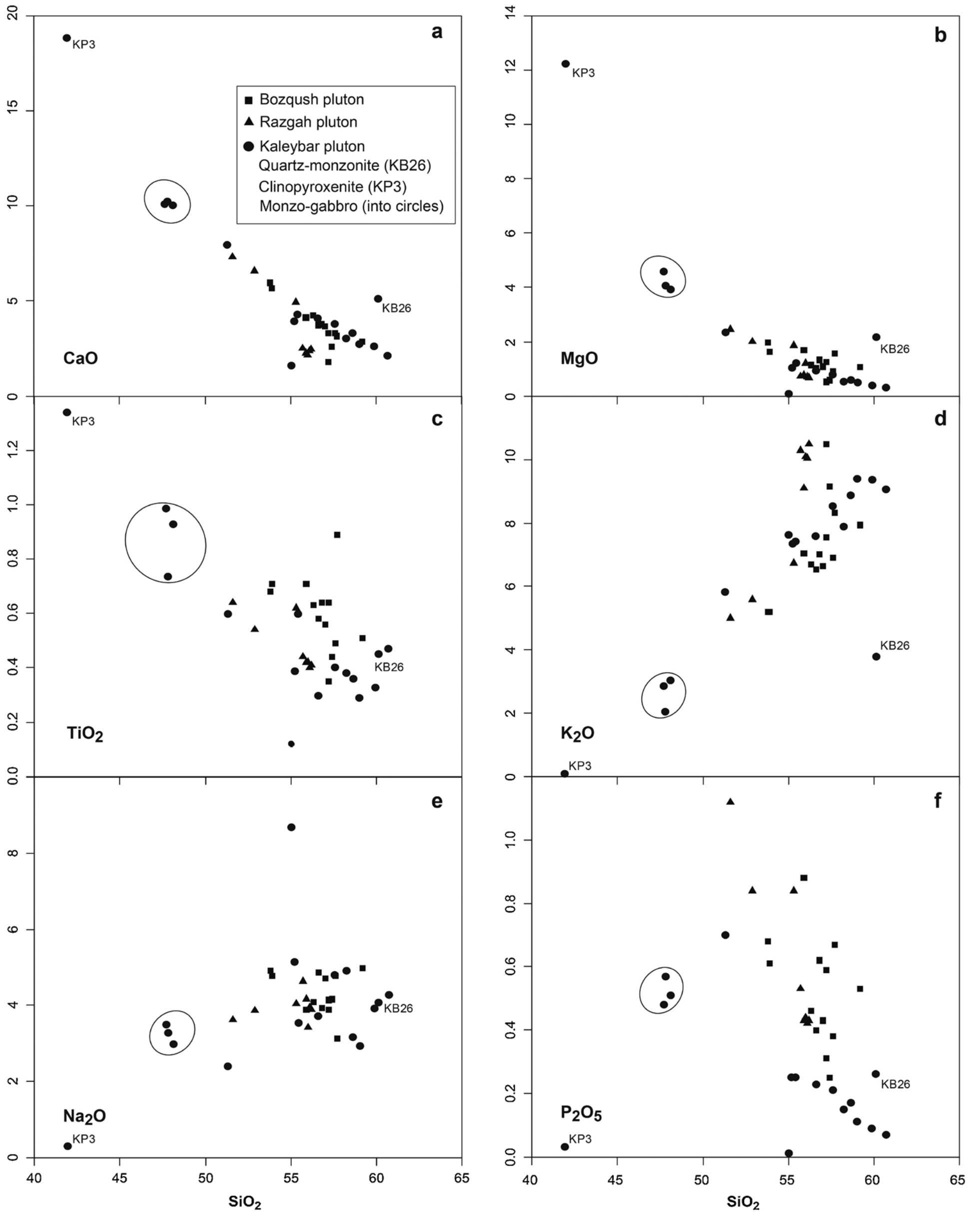

Fig. 8. Harker variation diagrams (SiO_2 versus major oxide in wt.%) of the studied samples.

the chemistry of their host magma (e.g., Giret et al., 1980; Leterrier et al., 1982; Deer et al., 1992; Rollinson, 1993). The chemistry of the clinopyroxenes and the amphiboles indicates that they were derived from alkaline (miaskitic) magmas of volcanic arc affinity at relatively low pressures (Ashrafi et al., 2014). The composition of the spinels (low Ni-Cr), plagioclases (An_{42-28}), olivines (Mg# < 0.5), and micas (Mg# < 0.5 in the nepheline syenites and Mg# ≈ 0.5-0.7 in the monzo-gabbros), amphiboles (Mg# ≈ 0.3-0.55), and pyroxenes (Mg# ≈ 0.5-0.8) can be attributed to derivation from a more evolved magma. According to previous studies (e.g., Abdel-Rahman, 1994; Stussi and Cuney, 1996; Sørensen, 1997; Marks et al., 2011), the composition of the KRB amphiboles, biotites, and clinopyroxenes shows a metaluminous, orogenic, and miaskitic suite nature (Ashrafi et al., 2009b, 2014). The occurrence of melanite, analcite, and pseudoleucite in the KRB plutons suggests that late- or post-magmatic processes played a significant role in the formation of secondary rock-forming minerals (Ashrafi et al., 2009a).

Based on the whole rock geochemistry, the foid-syenites and associated rocks have potassic alkaline (shoshonitic) and metaluminous affinities. The almost linear trends in the SiO_2 variation diagrams (such as the positive trends of K_2O, Rb, and Zr and the negative trends of CaO, MgO, TiO_2, $Fe_2O_3^{tot}$, V, and Co) and very low concentrations of compatible elements (such as Ni and Cr) seem to be consistent with the removal of Ca-plagioclase (supported by some of the REE patterns showing marked negative Eu anomalies as well), magnetite, pyroxene, and olivine during fractional crystallization. The Mg# values of the clinopyroxenite (~0.6), the monzo-gabbro (~0.5), and the foid syenite (< 0.4) are low, which confirm derivation from a differentiated melt. The Mg# of the pyroxene and the bulk (clinopyroxenite) are much higher (0.8 and 0.6, respectively) than for the differentiated rocks (foid syenite, 0.2-0.4). Therefore, the clinopyroxenite can be an early cumulate mafic rock. Basically the removal of the clinopyroxenite from a melt having the monzo-gabbro composition will drive the residual melt to more differentiated composition (e.g., Jagoutz, 2010; Nandedkar et al., 2014; Jagoutz and Klein, 2018), which indeed corroborate the fractional crystallization pattern.

Fractional crystallization associated with crustal contamination (AFC) is an important process during magma evolution (DePaolo, 1981) and may modify both elemental and isotopic compositions. Minor crustal contamination might result in negative Nb-Ta anomalies relative to LILE and LREE but would also produce positive Zr-Hf anomalies due

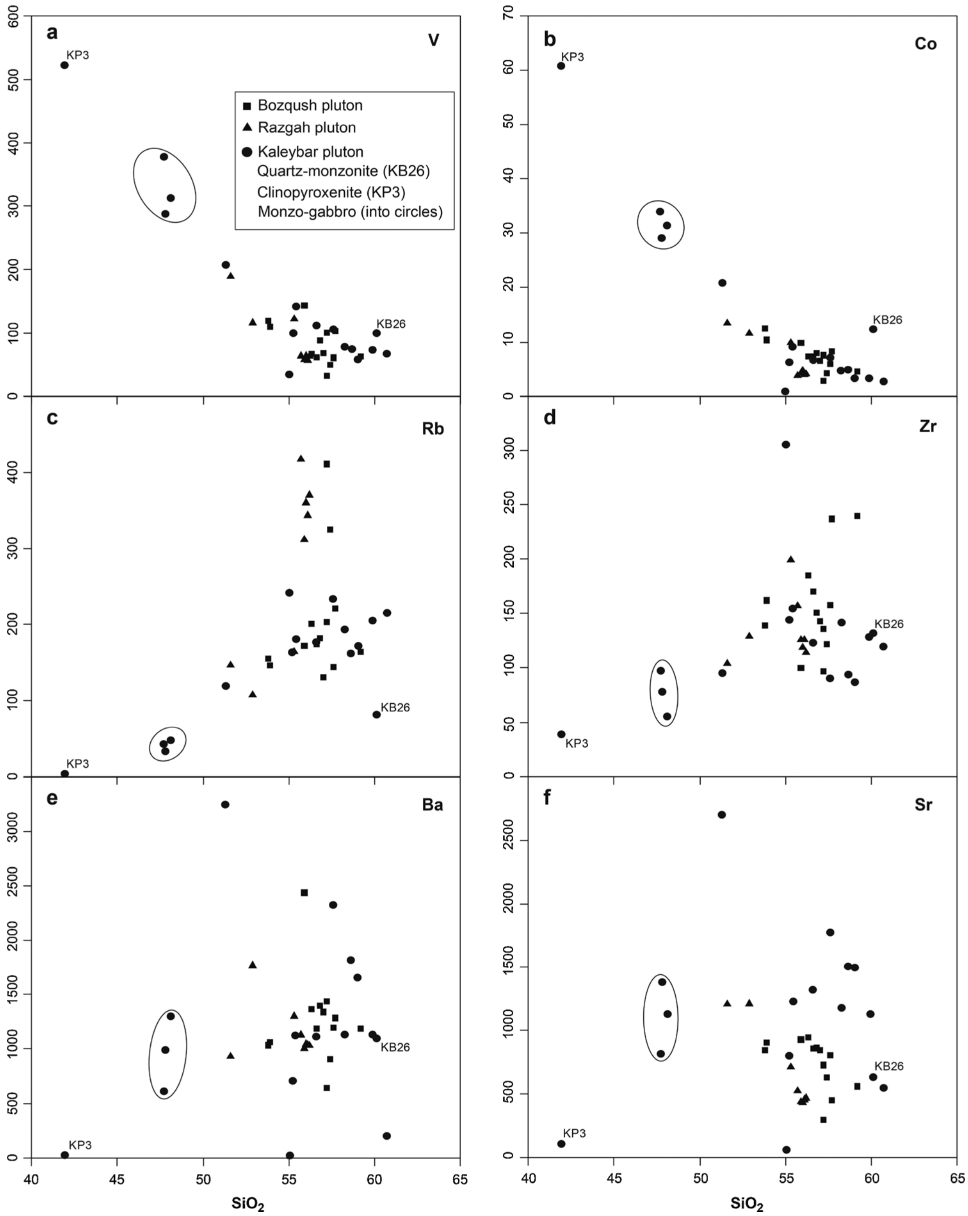

Fig. 9. Harker variation diagrams (SiO_2 in wt.% versus rare element in ppm) of the studied samples.

enrichment of these elements in crustal materials (Zhao and Zhou, 2007). The negative Zr-Hf anomalies observed in the spider diagrams for the KRB rocks (Fig. 10) support an interpretation that only little or no crustal contamination occurred.

8.2. Nature of the mantle source region

Green (1995) noted that in alkaline suites Nb/Ta and Zr/Hf ratios tend to fall into two groups. One group is characterized by a consistent ratio close to chondritic or mantle values (Nb/Ta = 17 and Zr/Hf = 40) whereas the other consists of a highly variable ratios significantly greater than mantle values. The KRB rocks belong to the first group, Nb/Ta = 11–17 and Zr/Hf = 33–44, with the exception of clinopyroxenite and a nepheline syenite sample (KB13) from the Kaleybar pluton (Fig. 12a). The presence of considerable Ti-garnet, together with titanite and zircon in the KB13 sample, which contain significant amounts of these elements, could contribute to the high ratios. The Kaleybar clinopyroxenite is characterized by Nb/Ta = 3 and Zr/Hf = 21). It is petrographically similar to the pyroxenites from the Ilomba intrusion, Malawi (Eby et al., 1998) and probably represent an early fractionated mafic cumulate. High Nb and Ta have been used to indicate an Oceanic-island basalt (OIB) component in magmatic rocks (e.g., Edwards et al., 1994). The KRB rocks are depleted in Nb and Ta. Although such negative anomalies can be caused by crustal contamination, the KRB rocks have obvious negative Zr-Hf anomalies in the primitive mantle-normalized trace element diagram (Fig. 10), ruling out the possibility of significant crustal contamination. Thus, there is no evidence of an OIB component in the source region of these rocks. Instead, the KRB plutons are believed to have been derived from lithospheric mantle sources.

In Fig. 12b, Ta/Yb values the KRB samples are plotted against their Th/Yb values. Fig. 12b shows that the KRB rocks form trends that run parallel to the mantle metasomatism array (Pearce, 1983) but are displaced towards higher Th/Yb ratios, suggesting either derivation from an enriched mantle source to which a subduction component had been added, or coupled crustal contamination with fractional crystallization (the inferred AFC curve on the diagram), or both.

Residual mineralogy and degree of partial melting in the AAMB

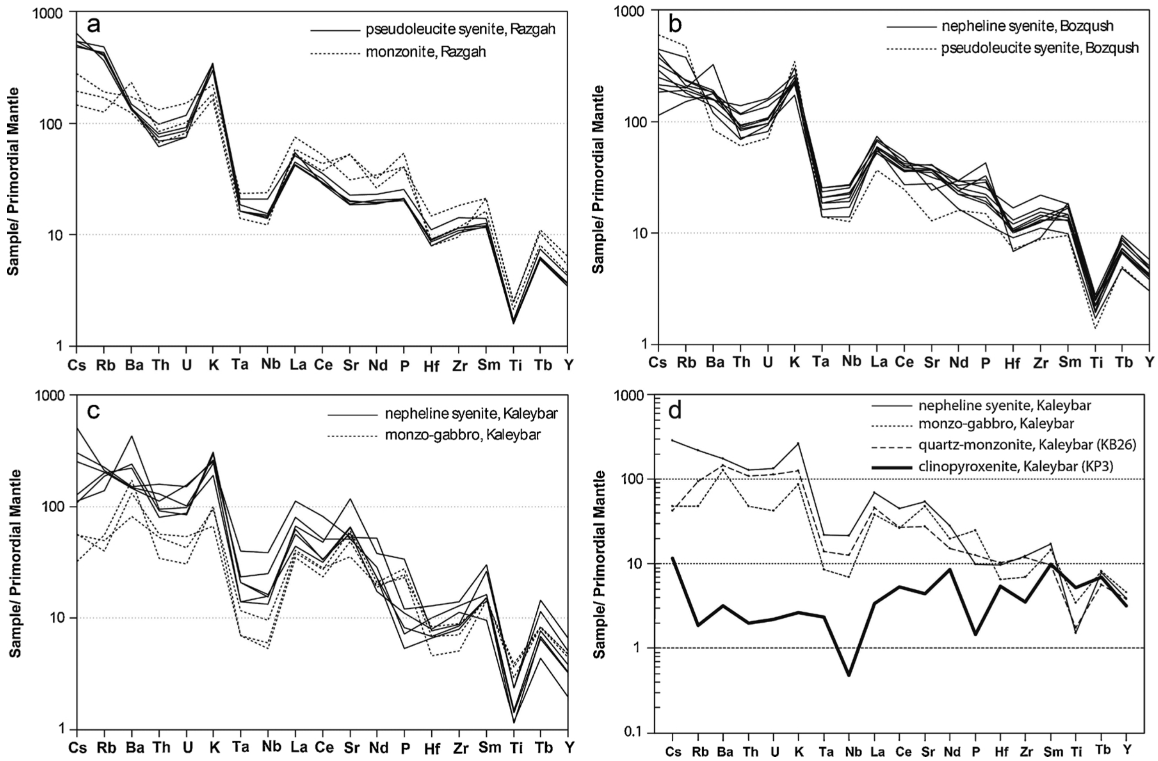

Fig. 10. Primordial mantle normalized patterns of the KRB samples; (a) the Razgah pseudoleucite syenite and monzonite, (b) the Bozqush nepheline syenite and pseudoleucite syenite, (c) the Kaleybar nepheline syenite and monzo-gabbro, and (d) comparison of the Kaleybar ultrabasic (KP3), basic (monzo-gabbro), and intermediate (KB26) samples. Normalizing values are from Wood et al. (1979).

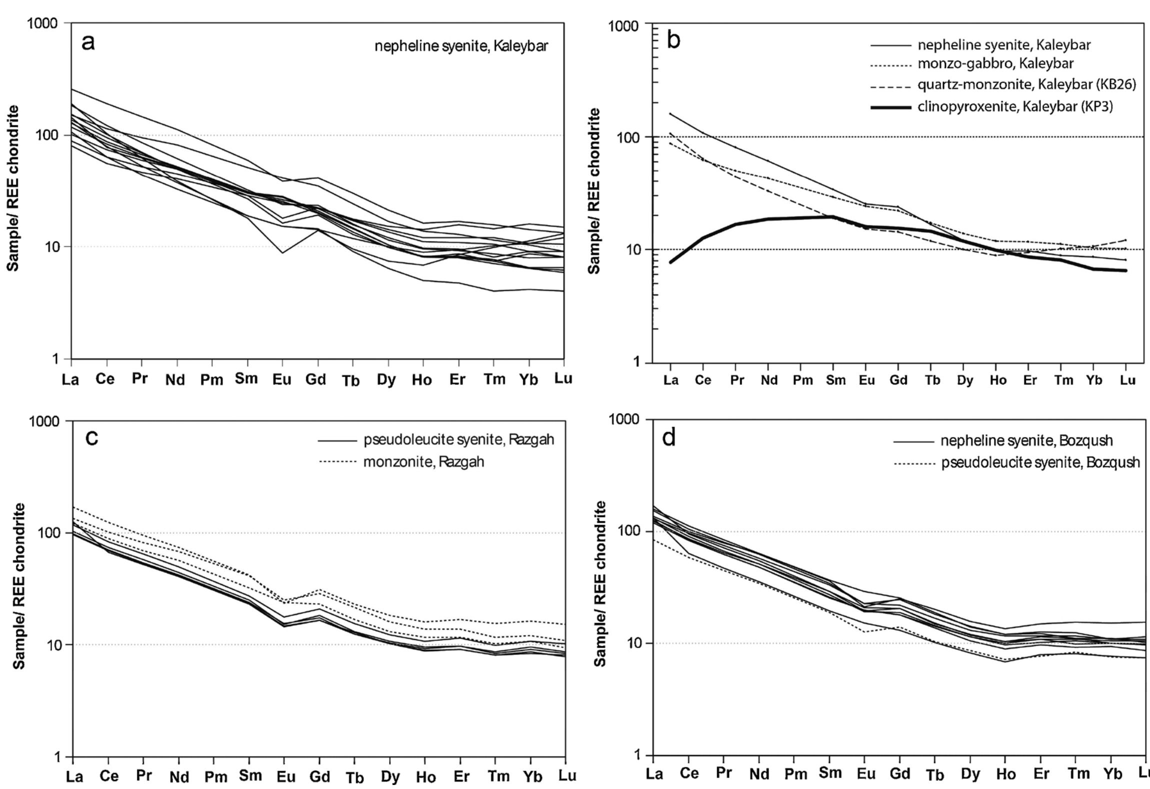

Fig. 11. Chondrite normalized REE patterns of the KRB samples; (a) the Kaleybar nepheline syenites, (b) comparison of the Kaleybar clinopyroxenite, quartz-monzonite, nepheline syenite, and monzo-gabbro (c) the Razgah pseudoleucite syenite and monzonite, and (d) the Bozqush samples. Normalizing values are from Boynton (1984).

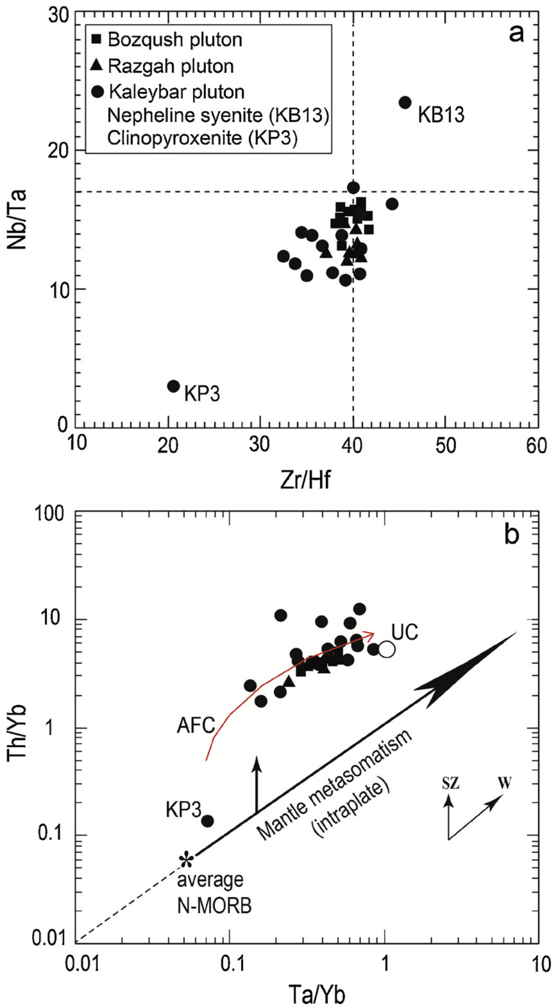

Fig. 12. (a) Zr/Hf versus Nb/Ta plot for the KRB rocks. (b) Th/Yb versus Ta/Yb diagram (Pearce, 1983) for the KRB rocks. Abbreviations: AFC, assimilation combined with fractional crystallization curve; SZ, subduction zone enrichment; UC, upper crust composition (Taylor and McLennan, 1985); W, within-plate enrichment.

lithospheric mantle can be better characterized using REE abundances and ratios in the gabbroic samples. The least differentiated rocks of the KRB magmatic series, the Kaleybar monzo-gabbro, display Mg# ≈ 0.5 and can represent parental magmas derived from primitive melts via crustal differentiation (e.g., Kelemen et al., 2003). Therefore, the monzo-gabbro samples of the Kaleybar pluton plot in the modeling diagrams (Aldanmaz et al., 2000; Jourdan et al., 2007). The mantle source partial melting was constrained using the mineral proportions in the range of spinel lherzolite and garnet lherzolite (Kinzler, 1997; Walter, 1998) together with the non-modal batch melting equilibrium equation $C_{liq}/C_i = 1/(D + F(1\text{-}P))$ of Shaw (1979), where C_{liq} is the concentration of a given element in the residual melt, C_i is the initial concentration of an element i in the parental melt, F is the fraction of melt produced, D is the bulk partition coefficient, and P is the bulk partition coefficient of the trace elements entering the melt from the melting minerals. See Aldanmaz et al. (2000); Jourdan et al. (2007), and the caption of Fig. 13 for further details.

La and Sm are not affected significantly by variations in the source mineralogy (e.g., garnet or spinel) and hence can provide information on the bulk chemical composition of the source. Fig. 13a shows that the studied samples (red circles) have La concentrations and La/Sm ratios greater than those that could be generated by direct melting of depleted MORB mantle (DMM), even when the degree of partial melting is very small (0.1%). Thus, it can be argued that one-stage melting of DMM or primitive mantle (PM) cannot produce magma with incompatible element concentrations similar to those of the studied rocks. The garnet-dependent, Sm/Yb ratio, can be used to constrain the source mineralogy of the alkaline magmas because Yb is compatible with garnet (Kd = 11.50, Arth, 1976), but not with clinopyroxene (Kd = 0.62, Arth, 1976). Fig. 13b show that the rocks are displaced from the spinel-lherzolite melting trend to higher Sm/Yb ratios and plot between the melting trajectories drawn for garnet- and garnet + spinel-lherzolite. Fig. 13a and b can also be combined as a plot of MREE/HREE against the LREE/MREE ratios, e.g., Sm/Yb versus La/Sm (Fig. 13c, d). Melting of a spinel-lherzolite source will create a horizontal melting trend, which lies within or close to a mantle array defined by DMM and PM compositions. In contrast, a small (or moderate) degree of partial melting of a garnet-lherzolite source (with garnet residue) produces melt with significantly higher Sm/Yb ratios than the mantle source. Fig. 13c and d show that variable degrees of partial melting of a spinel-lherzolite source cannot explain the compositions of the studied rocks as these plot well above the mantle array and spinel-lherzolite melting trends. The simplest model to account for the REE systematics of the studied samples thus involves garnet + spinel mantle mineralogies (and low to moderate degree of partial melting).

Garnet and amphibole have strongly different MREE/HREE partition coefficients (i.e., $D_{Dy/Yb} << 1$ and > 1, respectively), amphibole preferentially incorporates MREEs over HREEs, while garnet incorporates HREEs. As a result, while both residual amphibole and garnet increase La/Yb ratios of partial melts, residual garnet will simultaneously increase Dy/Yb, but residual amphibole will decrease Dy/Yb (Gao et al., 2009; Rollinson, 1993). From the high LREE enrichment but low HREE fractionation of the studied rocks (Fig. 11), it can be inferred that amphibole differentiation had a minor role in the genesis (also showed by minor Ho negative anomalies) and or amphibole was a residual in the melting process. It should be noted, however, the REE may be mobilized by halogen-rich or carbonate-rich mineralizing fluids in a rock. Fluid transport by F-Cl- and CO_3-rich solutions and the late magmatic stage processes might modify primary linear REE patterns to HREE flattening and U-shaped patterns. Occurrence of late primary and secondary phases such as garnet (melanite) and calcite, sodalite, zeolite, cancrinite, analcime, and fluorite in the studied rocks show that halogen- or carbonate-rich fluids played a significant role in the formation of the mentioned minerals (Eby et al., 1998; Eby, 2004; Fall et al., 2007). Relative abundances of the alkali and alkaline earth elements such as Rb, Sr and Ba can be used to assess the presence of amphibole and/or phlogopite in the mantle source region. These phases are important because they can attest to the metasomatic enrichment history of the source region, as well as helping to constrain the depth of melting. Both Rb and Ba are compatible in phlogopite (LaTourette et al., 1995), while Rb, Sr and Ba are moderately compatible in amphibole (Adam et al., 1993; LaTourette et al., 1995). Melts in equilibrium with phlogopite are expected to have significantly higher Rb/Sr and lower Ba/Rb values than those formed from amphibole-bearing sources. On the contrary, melts of an amphibole-bearing source may have extremely high Ba contents and Ba/Rb values. The ratios of Rb/Sr and Ba/Rb of gabbroic samples are plotted in Fig. 14a and do not indicate any distinct amphibole or phlogopite trend. Furthermore, in the Rb versus Rb/K diagram (Fig. 14b) the samples plot between phlogopite and amphibole analyses from the literature. The gabbroic samples are characterized by low Rb/Sr (< 0.1), low Rb/Ba (< 0.1) and high Ti/K (> 0.1). These geochemical features are incompatible with the presence of phlogopite in the mantle source of studied rocks. Additionally, negatively correlated U/Pb and K/Nb ratios in high-K rocks have been attributed to the presence of a K-bearing mineral phase that fractionates U/Pb (Hawkesworth et al., 1990). In the gabbroic samples, high K/Nb (> 4000) and low U/Pb (< 0.3) are associated with low Rb/Sr, probably suggesting the presence of some residual amphibole in the source region. However, as phlogopite, amphibole and/or apatite-bearing

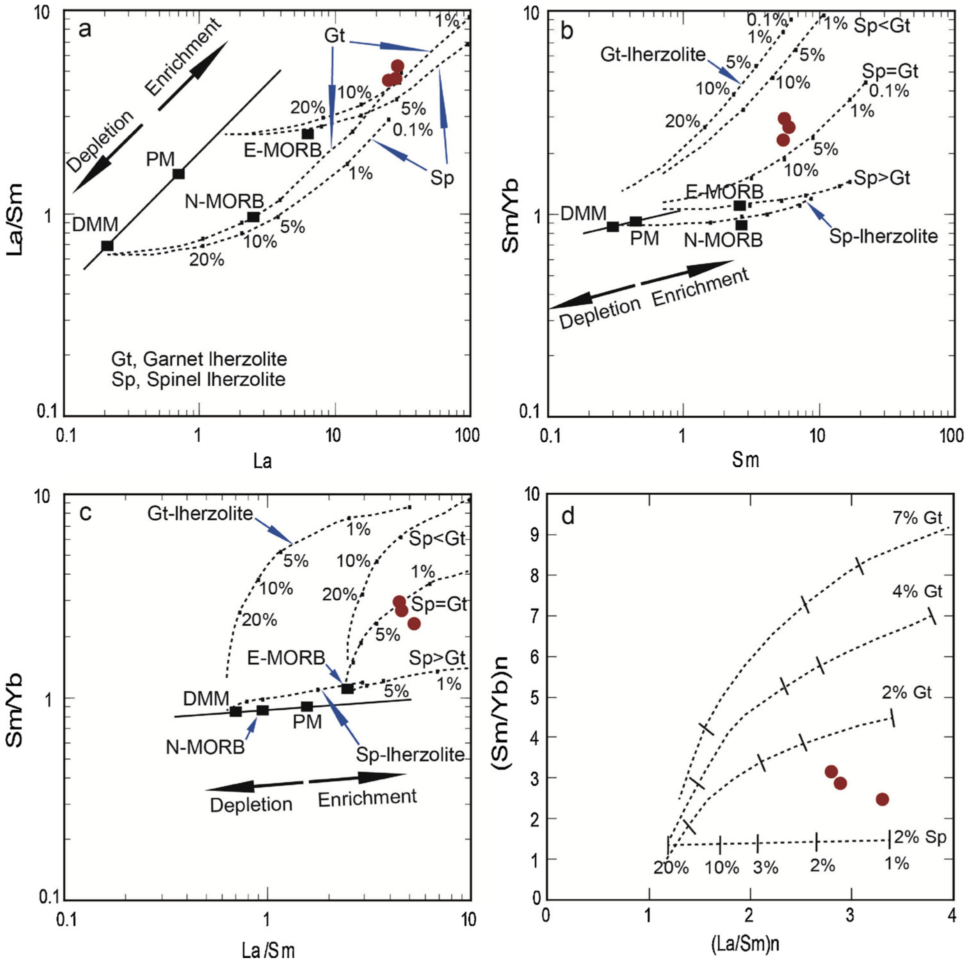

Fig. 13. (a)–(d) Plots of La/Sm versus La, Sm/Yb versus Sm, Sm/Yb versus La/Sm (Aldanmaz et al., 2000), and (Sm/Yb)n versus (La/Sm)n (Jourdan et al., 2007), showing modeling of REE abundances and ratios to constrain the source characteristics of the alkaline magma(s) in terms of REE concentrations, source mineralogy and degree of partial melting. The studied samples are shown as red circle. Mineral/matrix partition coefficients and DMM are from the compilation of McKenzie and O'Nions (1991, 1995); PM, N-MORB and E-MORB compositions, shown as black square in the diagrams, are from Sun and McDonough (1989). The chondrite-normalized values are after Boynton (1984). Melt curves obtained using the non-modal batch melting equations of Shaw (1970). The solid line represents the mantle array defined using DMM and PM compositions. Dashed curves are the melting trends. The tick marks on the curves correspond to melting degrees (For interpretation of the references to colour in this figure legend, the reader is referred to the web version of this article).

lherzolites are suggested to be the source for the subduction-related high-K rocks in Iran (e.g., Aftabi and Atapour, 2000; Liotard et al., 2008; Ahmadzadeh et al., 2010; Pang et al., 2013), it is possible that the phlogopite/amphibole signature decreased through mixing of melts derived from different mantle sources (e.g., Shafaii-Moghadam et al., 2014).

8.3. Modification of the mantle source by subduction components

The KRB rocks have Nb/U ratios range from1.3 to 8.8, which are significantly lower than the MORB and OIB (Nb/U = 47 ± 7; Hofmann et al., 1986) and the lower crust (Nb/U ≈ 25; Rudnick and Gao, 2003). Ayers (1998) suggested that subduction-zone hydrous fluids have significantly low Nb/U ratio (0.22), which may be ascribed to the transfer of considerable amounts of LILE but not HFSE in the slab-derived hydrous fluid. Accordingly, the significantly low Nb/U ratios of the KRB rocks are considered to be resulted from the fluid-related metasomatism in lithospheric mantle via a subduction process. According to LaFlèche et al. (1998), the fluid-related metasomatism in the subduction process would result in the depletions of Ta and Hf relative to La and Sm, respectively. In (Hf/Sm)n versus (Ta/La)n diagram (Fig. 14c), the gabbroic samples plot near/in the area of fluid-related subduction metasomatism, instead of melt-related subduction and carbonatite metasomatism (LaFlèche et al., 1998). Besides, the slab-derived H_2O rich fluids metasomatism also results in the strong relative enrichment in Cs over Rb (Sun and Stern, 2001). In contrast, the enrichment of Th over Yb may be ascribed to mantle wedge enrichment by melting of subducted sediments (Woodhead et al., 1998). In Cs/Rb versus Th/Yb diagram (Fig. 14d), the gabbroic rocks plot along the trend of the slab-derived fluid metasomatism. Source modification by subducted slab fluids is also supported by relatively low Nb/Zr and high Th/Zr ratios of the gabbroid samples. Fluids derived from the subducted slab will not only geochemically modify the overlying mantle wedge but will also lower the peridotite solidus to produce subduction-related magmas (Stolper and Newman, 1994; Grove et al., 2002). The ratios of Th/Zr and Nb/Zr of gabbroic samples are plotted in Fig. 14e and indicate a distinct fluid-related enrichment trend.

8.4. Geodynamic implications

The NE-oriented Arax strike-slip fault constitutes a major regional stratigraphic and structural limit between the NW Iran and the Lesser Caucasus (Sosson et al., 2010; Moritz et al., 2016b). The AAMB and the Lesser Caucasus have some contrasting Mesozoic tectonic, magmatic and sedimentary records (Moritz et al., 2016b). However, the AAMB and the Lesser Caucasus underwent similar Cenozoic tectonic evolutions (Moritz et al., 2016b). Also, the AAMB and the southernmost Lesser Caucasus reveal broadly similar magmatic evolutions during the Cenozoic, evolving from dominantly normal arc, calc-alkaline compositions during the Eocene to shoshonitic/alkaline and adakitic compositions sourced by a significant proportion of metasomatised lithospheric mantle during the Late Eocene-Miocene (Moritz et al., 2016a; Rezeau et al., 2017). The KRB rocks display similar geochemical features, enrichment in the LILE and LREE and depletion in the HFSE, which are typical of subduction-related magmas (Fig. 10). The chondrite-normalized patterns for REE show a slight depletion in HREE in the Kaleybar monzo-gabbros compared with the nepheline syenites (Fig. 11b), and a slight depletion in REE in the Razgah monzonites

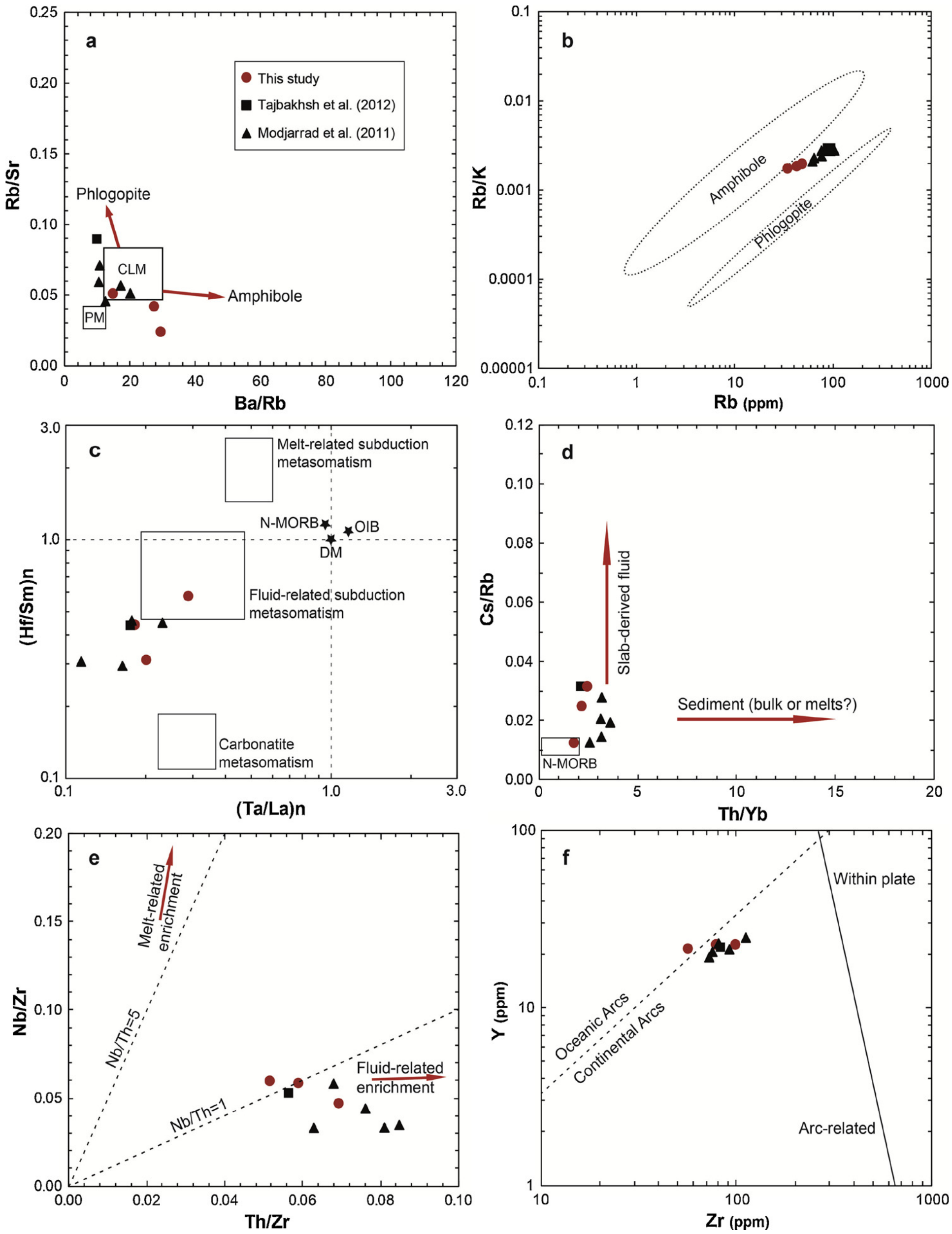

Fig. 14. (a–b) Variations in incompatible trace element ratios that may constrain source mineralogy; (a) Rb/Sr vs. Ba/Rb plot for the gabbroic rocks, the mineralogy of the CLM (common lithospheric mantle) source is inferred to include minor amounts of both amphibole and phlogopite (Furman and Graham, 1999), (b) Rb/K vs. Rb plot in which the gabbroic samples fall between the approximate phlogopite and amphibole composition fields (after Jung et al., 2004). (c–e) Evaluation of metasomatised mantle source in relation with subduction; (c) (Hf/Sm)n vs. (Ta/La)n diagram (after LaFlèche et al., 1998; primordial mantle normalizing values are from Wood et al., 1979), (d) Plot of Cs/Rb vs. Th/Yb (after Sun and Stern, 2001), (e) Nb/Zr vs. Th/Zr diagram for the gabbroic rocks, showing the source nature of the KRB plutons. (f) The tectonic discrimination diagram of Zr vs. Y (after Muller and Groves, 1997; dashed line after Pearce, 1983).

compared with pseudoleucite syenites (Fig. 11c), which support a genetic link between the basic and intermediate rocks. The gabbroic samples from the Kaleybar pluton (this study and Tajbakhsh et al. (2012)) and the Hashtsar pluton (Modjarrad et al., 2011) are plotted on the tectonic discrimination diagram of Muller and Groves (1997) (Fig. 14f). In the Zr versus Y diagram (Fig. 14f), the rocks fall into the Arc-related field. Also, on the basis of a Zr/Y value of 3 (dashed line in Fig. 14f after Pearce (1983)), almost all of the samples plot in the Continental-Arcs field, except for one sample which falls in the Oceanic-Arcs field. The age of emplacement of the KRB has not been determined by geochronological dating, but these alkaline plutons are Eocene to Oligocene (~55–23 Ma) in age, based on stratigraphical studies. Therefore, we focus on the tectono-magmatic events of the NW Iran and adjacent areas during the Eocene-Oligocene time. This stratigraphical age is consistent with dating of other adjacent plutons e.g. by Aghazadeh et al. (2010); Castro et al. (2013); Nabatian et al. (2014), and Rezeau et al. (2016, 2017), which yield ages of ~48–21 Ma based on Zircon U-Pb dating methods. However, the cooling ages for the KRB plutons range from ~40–29 Ma (Ashrafi et al., 2018), which determined by the apatite fission track analysis.

The geodynamic evolution of the AAMB is controversial, as well as the petrogenesis of its magmatic rocks. Azizi and Jahangiri (2008) proposed that the AAMB is related to the Khoy–Zanjan oceanic subduction beneath the Alborz-Azerbaijan plate and not to the Neo-Tethyan subduction beneath the Iranian plate. The boundary between the UDMA and the AAMB (i.e. Tabriz fault) is a sharp, distinct, deep-seated, high-angle fault zone (Alavi, 1996). Along the Tabriz Fault, there are some dismembered ophiolites (Azizi et al., 2006), which may be relicts of this oceanic crust (Azizi and Jahangiri, 2008). However, there is no detailed study about the mentioned ophiolites. Identical lithologic sequences of the same age in the UDMA and AAMB suggest that the two originally formed a single continental margin magmatic arc that was subsequently rifted apart (Hassanzadeh et al., 2002). Considering the underplated plumes formed in active continental margins may travel distances of more than 300 km below the lithospheric mantle according to predictions by numerical models (e.g., Currie et al., 2007); the UDMA (arc) and AAMB (back-arc) could resulted from subduction of Neo-Tethys oceanic crust beneath the Iranian plate.

Eocene normal faults have been identified in the Alborz Mountains (Guest et al., 2006), and stratigraphic evidence of Eocene subsidence in the Alborz Mountains and central Iran has been interpreted in terms of Eocene extension (e.g., Brunet et al., 2003; Hassanzadeh et al., 2004; Vincent et al., 2005; Morley et al., 2009). The presence of shallow marine sediments interbedded throughout the entire thickness of the Paleogene volcanic accumulations (Stöcklin, 1968; Berberian and King, 1981), as well as evidence of submarine volcanism (e.g., Förster et al., 1972; Amidi et al., 1984; Spies et al., 1984; Hassanzadeh, 1993), suggest synvolcanic subsidence. Thus, there is a growing body of evidence that much, if not all, of Iran was undergoing extension during at least part of the Eocene (Verdel et al., 2011; Mouthereau et al., 2012). The Neo-Tethys subduction has been an oblique convergence between the Arabian and the Central Iran plate. According to Upton et al. (2003), extension would be developed in an oblique convergence with the weak subduction interface rather than in an orthogonal convergence with the strong subduction interface. The long term subduction (from Upper Cretaceous to Paleogene) and probably high slab dipping angle of Neo-Tethys were propitious for a subsequent roll-back as the subducted slab plunges. Slab roll-back is commonly cited as the accepted mechanism for extension above subduction zones (e.g., Hamilton, 1995). Slab roll-back and consequent trench retreat play three key roles: (1) It inserts extensional episodes in an overall convergent regime, (2) it triggers changes in plate boundary patterns, and (3) it can trigger more mantle upwelling resulting in extensive magmatism (e.g., Zuo et al., 2017). The extensional regime in the Alborz-Azerbaijan micro-continent can be triggered by the slab roll-back of the Neo-Tethys system and probably produced a back-arc basin between the UDMA and the Alborz-Azerbaijan micro-continent (similar to the back-arc basin described by Alavi (1996) or the Khoy-Zanjan Ocean described by Azizi and Jahangiri (2008)). The back-arc basins related to E-, NE- and NNE-dipping subduction are characterized by slower opening rate and thick continental crust (Doglionli, 1995). We infer that extension was facilitated in the back-arc because of different velocity of the lithosphere in the hanging-wall of the Neo-Tethys subduction by the Tabriz fault. The Tabriz fault was defined as the western-southwestern border of the back-arc while the Talesh fault (and maybe other faults with the parallel trend) formed the eastern-northeastern border of the back-arc (Fig. 15). The voluminous Eocene-Oligocene shoshonitic magmatism was facilitated by local lithospheric extensions (mentioned by Lescuyer and Riou (1976) as incomplete local rift or extension) and was contemporaneous with calc-alkaline magmatism in the AAMB.

The major Cenozoic plutons of the AAMB, such as the Anzan, Khankandi, Shaivar-dagh, Sungun, Yuseflu, Roudbar, and Abhar plutons (i.e., the Arasbaran–Taroum batholith) and the KRB intrusions (e.g., Babakhani et al., 1990; Berberian and Berberian, 1981; Aghazadeh et al., 2010; Castro et al., 2013), can be correlated with the Dalidag, Pambak, Meghri-Ordubad, and Bargushat plutons in the Lesser Caucasus (e.g., Kazmin et al., 1986; Lordkipanidze et al., 1989; Sosson et al., 2010; Moritz et al., 2016b; Rezeau et al., 2017).

The Late Eocene to Neogene AAMB magmatism is attributed to decompression melting of metasomatised lithospheric mantle during extension and thinning of the crust (Aghazadeh et al., 2011; Castro et al., 2013). Castro et al. (2013) pointed out that the Arasbaran-Taroum batholith formed in a post-collisional setting and concluded that monzonitic and shoshonitic magmas of some plutons of the AAMB (Shaivar-Dagh, Khankandi and Yuseflu) have an adakitic signature inherited from early melts that metasomatized the peridotite mantle and subsequent decompression melting. However, the Neogene southernmost Lesser Caucasus magmatism is attributed to the transpressional geodynamic setting accompanied by crustal thickening as a consequence of decompressional melting of lower crust and lithospheric mantle (Moritz et al., 2016a). Also, Rezeau et al. (2017) proposed a decrease of the degree of partial melting of the sub-lithospheric mantle for the generation of shoshonitic magmas in related to the initiation of the Arabia-Eurasia collision. Although these scenarios would certainly initiate decompression melting, variations in the degree of partial melting, and/or slab silicic melts reactions in the mantle wedge generating adakite-like melts; the data presented in this study do not allow us to constrain all of these geodynamic settings during the Eocene-Oligocene magmatism.

In all the previous studies, the identification of subduction components in the Eocene-Oligocene plutonic rocks from NW Iran, with calc-alkaline to shoshonitic affinity, have been attributed to an unknown subduction or to the Neo-Tethys subduction notwithstanding that the mid-Tertiary plutons are more than 300 km farther from the Neo-Tethyan suture or to the back-arc setting related to the Neo-Tethys subduction. Commonly, the Cenozoic pre- to post-collision magmatism of the NW of Iran has been attributed to the subduction system of the southern branch of the Neo-Tethys Ocean (e.g., Castro et al., 2013; Aghazadeh et al., 2011) while the post-collision magmatism of the SAQ subduction system linked to slab break-off could also take place during the Cenozoic in the NW of Iran. The SAQ suture, the nearest suture zone to the studied area, is surrounded between two old long major faults, in the W-SW by the Tabriz fault and in the E-NE by the Talesh fault which might locally facilitate this post-collision magmatism (Fig. 15). Slab break-off may have led to thermal perturbation resulting in melting of the detached slab and metasomatism of the mantle in NW Iran and adjacent areas during the post-collisional event. The temporal (Late

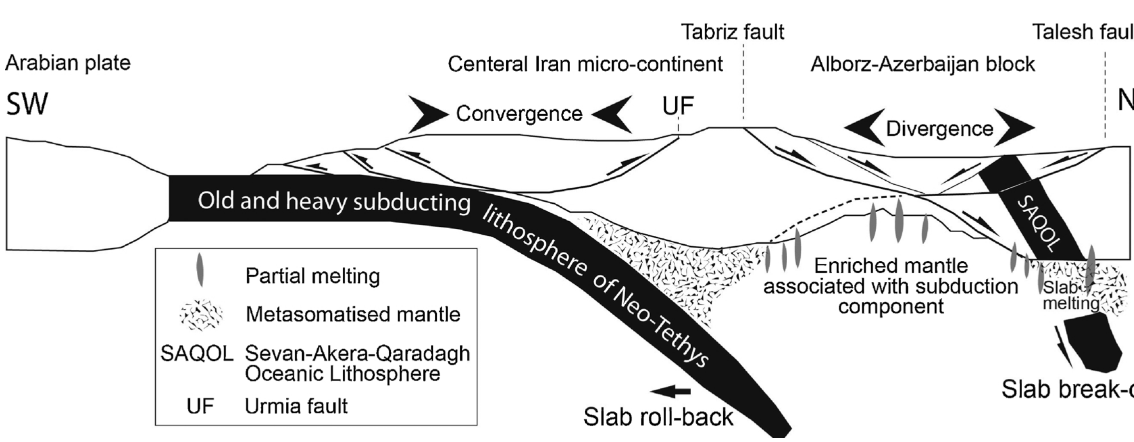

Fig. 15. Schematic model illustrating the geodynamic evolution of the Central Iran micro-continent and the Alborz-Azerbaijan block during the Eocene; the section highlights are adding subduction components and adakitic signatures to the AAMB magmas by the subduction and slab roll-back of Neo-Tethys as well as the SAQ slab break-off, mantle metasomatised by slab dehydration/melting at shallow depths during the early stages of subduction, melting enriched mantle under the AAMB by local lithospheric extension within Alborz-Azerbaijan block, and facilitating the local extension and magma ascending by the main faults (Tabriz and Talesh).

Oligocene - Early Miocene, Rezeau et al., 2017; Late Eocene-Oligocene, Castro et al., 2013) and spatial relationship of the adakite-like rocks with shoshonitic/alkaline rocks may be related to break-off of the subducted SAQ oceanic lithosphere beneath the Eurasian plate (e.g., Berberian, 1983; Galoyan et al., 2009; Rolland et al., 2009) or the Lesser Caucasus and the NW of Iran (Eyuboglu et al., 2011, 2012, 2014). The origin of adakites has been attributed to partial melting of either subducted oceanic crust converted to amphibole eclogite and garnet amphibolite (e.g., Defant and Drummond, 1990; Martin, 1999) or crustal differentiation dominated by amphibole in a thickened lower crust (e.g., Chapman et al., 2015; Chiaradia, 2015). Geophysical investigations indicate that the thickness of crust in this area is about 40–45 km (Dehghani and Makris, 1984), which is not an adequate depth for conversion of basaltic lower crust into garnet amphibolite or amphibole eclogite. Moreover, such deeper crustal materials have not been observed nor reported as xenoliths from the studied area.

The presence of the subduction component in the KRB rocks can be explained by the enriched mantle flow of Neo-Tethys and/or the SAQ slab break-off (Fig. 15). Slab-steepening and/or break-off in a collision setting may rapidly alter the pattern of flow in the asthenospheric mantle beneath the collision zones (e.g., Funiciello et al., 2006; Keskin et al., 2008; Kincaid and Griffiths, 2004; Neill et al., 2015). An asthenospheric mantle flow driven by the break-off of the SAQ slab during the Eocene might have dragged the subduction-modified asthenospheric mantle beneath the Alborz-Azerbaijan block to the southwest towards the slab (Fig. 15). The low partial melting of such a subduction-modified source material might have generated shoshonitic magmas with a subduction signature. Many subducted slabs experience multistage dehydration or melting. Slab dehydration normally occurs at shallower depths than slab melting (Rollinson and Tarney, 2005). Removal of mobile LILE from the slab by fluids is typically associated with the early stages of subduction, whereas later melting produces adakites with high K/Rb ratios and low Th, K and Rb contents. Thus, rocks associated with slab melt-modification are generally distributed behind those derived from fluid enriched mantle sources (Rollinson and Tarney, 2005; Zhao and Zhou, 2007).The gabbroic samples are characterized by low K/Rb ratios (498–561) and high Th (3–5 ppm), K ($>$ 17,000 ppm) and Rb (34–48 ppm) contents, which are consistent with a mantle source affected by slab dehydration rather than melting of subducted sediments (also see subsection 8.3). In the Meghri-Ordubad pluton of southernmost Lesser Caucasus, evolution from calc-alkaline to shoshonitic magmatic series has been attributed to a decrease of garnet lherzolite partial melting due to decrease of slab-related fluid input (Rezeau et al., 2017). A considerable decrease of the slab-related fluid input could be occurred during Eocene in the SAQ slab, which has probably contributed in the origin of KRB shoshonitic rocks (Fig. 15). We infer that the adakitic signatures in some Late Eocene-Oligocene plutons of the AAMB (Castro et al., 2013) can be attributed to the SAQ slab break-off and melting of the detached slab (e.g., Defant and Drummond, 1990). Lithospheric extension and decompression-driven partial melting of subduction-metasomatized lithosphere is the probable mechanism for the generation of the KRB shoshonitic magma. Melting of mantle lithosphere by the perturbation of the geotherm due to delamination of the thermal boundary layer or slab detachment, leading to conductive heating of enriched mantle, has been suggested for the origin of the Anatolian volcanic and plutonic rocks (e.g., Pearce et al., 1990; Aldanmaz et al., 2000; Keskin, 2003; Ilbeyli et al., 2004; Ilbeyli, 2005). In the case of KRB rocks, we argue that local lithospheric extension possibly affected at least some parts of Alborz-Azerbaijan block for the generation of the KRB shoshonitic magma in Eocene-Oligocene times. The local lithospheric extension was within an overall convergent setting and the coexistence of calc-alkaline and shoshonitic magmatism in the AAMB may be explained by differences in their mantle source regions related to low degree of partial melting and/or source composition. However, more detailed isotopic data is needed to constrain the possibility of the magmatism by lithospheric extension and precise temporal relation of the subduction-related alkaline rocks for evaluation of the proposed scenario.

9. Conclusions

The composition of the rock-forming minerals indicates that they were derived from alkaline (miaskitic) magmas of volcanic arc and can be attributed to derivation from a more evolved magma. Based on the whole rock geochemistry, the foid-syenites and associated rocks show mildly alkaline (shoshonitic) and metaluminous affinity. The removal of magnetite, olivine, pyroxene, and Ca-plagioclase during fractional crystallization is inferred from the major and trace element variations. Also, the removal of the clinopyroxenite, an early cumulate mafic rock (Mg# $\approx$ 0.6), from the monzo-gabbro composition melt (Mg# $\approx$ 0.5) could produced the more differentiated composition such as nepheline syenite, which indeed corroborate the fractional crystallization pattern. Geochemical data, HFS element depletion such as Nb, Ta and Ti, as well as discrimination diagrams indicate an arc-related environment for genesis of the KRB rocks. The geochemical results and melt generation modeling based on trace elements and REE presented above showed that the source of the KRB rocks was enriched in LILE and LREE relative to DMM and PM. Lithospheric extension within an overall convergent setting and decompression-driven partial melting of subduction-metasomatized lithosphere is the probable mechanism for the generation of the KRB mildly alkaline magma. A chemically enriched lithospheric mantle source composed of garnet-spinel-lherzolite that has undergone a low degree of partial melting ($<$ 5%) at shallow depths is proposed to generate the KRB intrusions. The KRB rocks were derived from a mantle source modified by fluids related to the subducted slab. Some geochemical features are compatible with the presence of amphibole in the mantle source of studied rocks. However, it is possible that the phlogopite signature decreased through mixing of melts derived from different mantle sources. The presence of the subduction component in the KRB rocks can be explained by the enriched mantle flow of Neo-Tethys and/or the SAQ slab break-off. A mantle flow driven by the break-off of the SAQ slab during the Eocene might have dragged the subduction-modified mantle beneath the Alborz-Azerbaijan block to the southwest towards the slab.

Acknowledgments

This work was supported by the Payame Noor and Tabriz Universities (Iran) and the Kanazawa University (Japan), for which we are thankful. The authors would like to acknowledge contributions of the Journal editors and reviewers, especially A. Holzheid, H. Shafaii-Moghadam, and H. Rezeau, in improving the manuscript by providing valuable suggestions.

References

Abdel-Rahman, A.M., 1994. Nature of biotites from alkaline, calc-alkaline, and peraluminous magmas. J. Petrol. 35, 525–541.
Adam, J.D., Green, T.H., Sie, S.H., 1993. Proton microprobe determined partitioning of Rb, Sr, Ba, Y, Zr, Nb and Ta between experimentally produced amphiboles and silicate melts with variable F content. Chem. Geol. 109, 29–49.
Adamia, S.A., Chkhotua, T., Kekelia, M., Lordkipanidze, M., Shavishvili, I., Zakariadze, G., 1981. Tectonics of Caucasus and adjoining regions: implications for the evolution of the Tethys ocean. J. Struct. Geol. 3, 437–447.
Aftabi, A., Atapour, H., 2000. Regional aspects of shoshonitic volcanism in Iran. Episodes 23, 119–125.
Agard, P., Omrani, J., Jolivet, L., Whitechurch, H., Vrielynck, B., Spakman, W., Monié, P., Meyer, B., Wortel, R., 2011. Zagros orogeny: a subduction-dominated process. Geol. Mag. 148, 692–725.
Aghanabati, A., 1990. Magmatic Rocks of Iran, Geological Quadrangle Map (scale 1:2,500,000). Geological Survey of Iran, Tehran.
Aghazadeh, M., Castro, A., Rashidnejad-Omran, N., Emami, M.H., Moinevaziri, H., Badrzadeh, Z., 2010. The gabbro (shoshonitic)–monzonite–granodiorite association of Khankandi pluton, Alborz Mountains, NW Iran. J. Asian Earth Sci. 38, 199–219.
Aghazadeh, M., Castro, A., Badrzadeh, Z., Vogt, K., 2011. Post-collisional polycyclic plutonism from the Zagros hinterland: the Shaivar dagh plutonic complex, Alborz

belt, Iran. Geol. Mag. 148, 980–1008.
Ahmadzadeh, G., Jahangiri, A., Lentz, D., Mojtahedi, M., 2010. Petrogenesis of Plio-Quaternary post-collisional ultrapotassic volcanism in NW of Marand, NW Iran. J. Asian Earth Sci. 39, 37–50.
Alavi, M., 1996. Tectonostratigraphic synthesis and structural style of the Alborz Mountain System in Iran. J. Geodyn. 21, 1–33.
Alavi, M., 2004. Regional stratigraphy of the Zagros folded-thrust belt of Iran and its proforeland evolution. Am. J. Sci. 304, 1–20.
Alberti, A.A., Comin-Chiaramonti, P., DiBattistini, G., Nicoletti, M., Petrucciani, C., Sinigoi, S., 1976. Geochronology of the Eastern Azerbaijan volcanic plateau (north-west Iran). Rendiconti della Societa Italiana di Mineralogia e Petrologia 32, 579–590.
Aldanmaz, E., Pearce, J.A., Thirwall, M.F., Mitchell, J.G., 2000. Petrogenetic evolution of late Cenozoic post-collision volcanism in western Anatolia, Turkey. J. Volcanol. Geotherm. Res. 102, 67–95.
Alici, P., Temel, A., Gourgaud, A., Kieffer, G., Gundogdu, M.N., 1998. Petrology and geochemistry of potassic rocks in the Golcuk area (Isparta, SW Turkey): genesis of enriched alkaline magmas. J. Volcanol. Geotherm. Res. 85, 423–446.
Allen, M.B., Armstrong, H.A., 2008. Arabia-eurasia collision and the forcing of mid-Cenozoic global cooling. Paleogeogr. Paleoclimatol. Paleoecol. 265, 52–58.
Amidi, S.M., Emami, M.H., Michel, R., 1984. Alkaline character of Eocene volcanism in the middle part of Iran and its geodynamic situation. Geol. Rundsch. 73, 917–932.
Arth, J.G., 1976. Behavior of trace elements during magmatic processes, a summery of theoretical models and their applications. J. Res. US Geol. Sur. 4, 41–47.
Asadian, O., Aminifazl, A., Khodabandeh, A., 1993. Geological Map of Qarachaman-Torkamanchay Quadrangle (scale 1:100,000). Geological Survey of Iran, Tehran.
Ashrafi, N., 2009. Mineralogy, Petrology, and Geochemistry of Foid-syenites of East Azerbaijan, NW Iran. Ph.D. Thesis. University of Tabriz, Iran, pp. 190.
Ashrafi, N., Ameri, A., Jahangiri, A., Hasebe, N., Eby, G.N., 2009a. Mineral chemistry of garnets in the Kaleybar alkaline igneous intrusion, NW Iran. Iran. J. Crystallogr. Mineral. 17, 357–368.
Ashrafi, N., Jahangiri, A., Ameri, A., Hasebe, N., Eby, G.N., 2009b. Biotite mineral chemistry of the Bozqush and Kaleybar intrusions, NW Iran. Iran. J. Crystallogr. Mineral. 17, 381–394.
Ashrafi, N., Jahangiri, A., Hasebe, N., 2014. Study of amphibole and clinopyroxene chemistry of the Bozqush, Kaleybar, and Razgah alkaline igneous intrusions, NW Iran. Iran. J. Crystallogr. Mineral. 22, 381–392.
Ashrafi, N., Hasebe, N., Jahangiri, A., 2018. Cooling history and exhumation of the nepheline syenites, NW Iran: constraints from apatite fission track. Iran. J. Earth Sci. 10.
Avagyan, A., Sosson, M., Karakhanian, A., Philip, H., Rolland, Y., Melkonhyan, R., Davtyan, Y., 2010. Recent stress field evolution in the Lesser Caucasus and adjacent regions. In: In: Sosson, M., Kaymakci, N., Stephenson, R., Bergerat, F., Starostenko, V. (Eds.), Sedimentary Basin Tectonics from the Black Sea and Caucasus to the Arabian Platform 340. Geological Society of London, pp. 393–409 Special Publication.
Ayers, J., 1998. Trace element modeling of aqueous fluid–peridotite interaction in the mantle wedge of subduction zones. Contrib. Mineral. Petrol. 132, 390–404.
Azizi, H., Jahangiri, A., 2008. Cretaceous subduction-related volcanism in the northern Sanandaj-Sirjan Zone, Iran. J. Geodyn. 45, 178–190.
Azizi, H., Moinevaziri, H., 2009. Review of the tectonic setting of Cretaceous to Quaternary volcanism in northwestern Iran. J. Geodyn. 47, 167–179.
Azizi, H., Moinevaziri, H., Mohajjel, M., Yagobpoor, A., 2006. PTt path in metamorphic rocks of the Khoy region (northwest Iran) and their tectonic significance for Cretaceous–Tertiary continental collision. J. Asian Earth Sci. 27, 1–9.
Babakhani, A.R., 1981. Petrography and Geochemistry of the North Azerbaijan Nepheline syenites and Phonolites. M.Sc. Thesis. Tehran University, Iran, pp. 84.
Babakhani, A.R., Lesquyer, J.L., Riou, R., 1990. Geological Map of Ahar Quadrangle (scale 1:250,000). Geological Survey of Iran, Tehran.
Ballato, P., Uba, C.E., Landgraf, A., Strecker, M.R., Sudo, M., Stockli, D.F., Friedrich, A., Tabatabaei, S.H., 2011. Arabia-Eurasia continental collision: insights from late tertiary foreland-basin evolution in the Alborz mountains, northern Iran. Geol. Soc. Am. Bull. 123, 106–131.
Barker, D.S., 1987. Tertiary alkaline magmatism in trans-pecos Texas. In: In: Fitton, J.G., Upton, B.G.J. (Eds.), Alkaline Igneous Rocks 30. Geological Society, London, pp. 413–431 Special publications.
Berberian, M., 1983. The southern Caspian: A compressional depression floored by a trapped, modified oceanic crust. Can. J. Earth Sci. 20, 163–183.
Berberian, F., Berberian, M., 1981. Tectono-plutonic episodes in Iran. In: Gupta, H.K., Delany, F.M. (Eds.), Zagros Hindukush, Himalaya Geodynamic Evolution. American Geophysical Union, Washington, DC, pp. 5–32.
Berberian, M., King, G.C.P., 1981. Towards a paleogeography and tectonic evolution of Iran. Can. J. Earth Sci. 18, 210–265.
Berberian, M., Amidi, S.M., Babakhani, A., 1981. Discovery of The Qaradagh ophiolite belt; the southern continuation of the Sevan-Akera (Little Caucasus) ophiolite belt in northwestern Iran (Ahar quadrangle); a preliminary field note. Geol. Surv. Iran, Intern. Rep. 15.
Berberian, F., Muir, I.D., Pankhurst, R.J., Berberian, M., 1982. Late Cretaceous and early Miocene Andean type plutonic activity in northern Makran and central Iran. J. Geol. Soc. Lond. 139, 605–614.
Bertrand, G., Guillou-Frottier, L., Loiselet, C., 2014. Distribution of porphyry copper deposits along the western Tethyan and Andean subduction zones: insights from a paleotectonic approach. Ore Geol. Rev. 60, 174–190.
Boynton, W.V., 1984. Geochemistry of rare earth elements: meteorite studies. In: Henderson, P. (Ed.), Rare Earth Element Geochemistry. Elsevier, New York, pp. 63–114.
Brotzu, P., Gomes, C.B., Melluso, L., Morbidelli, L., Morra, V., Ruberti, E., 1997. Petrogenesis of coexisting SiO_2-undersaturated to SiO_2-oversaturated felsic igneous rocks: the alkaline complex of Itatiaia, Southeastern Brazil. Lithos 40, 133–156.
Brunet, M.F., Korotaev, M.V., Ershov, A.V., Nikishin, A.M., 2003. The South Caspian basin: A review of its evolution from subsidence modeling. Sediment. Geology 156, 119–148.
Carmichael, I.S.E., Lange, R.A., Luhr, J.F., 1996. Quaternary minettes and associated volcanic rocks of Mascota, western Mexico: A consequence of plate extension above a subduction modified mantle wedge. Contrib. Mineral. Petrol. 124, 302–333.
Castro, A., Aghazadeh, M., Badrzadeh, Z., Chichorro, M., 2013. Late Eocene–Oligocene post-collisional monzonitic intrusions from the Alborz magmatic belt, NW Iran: an example of monzonite magma generation from a metasomatized mantle source. Lithos 180-181, 109–127.
Chapman, J.B., Ducea, M.N., DeCelles, P.G., Profeta, L., 2015. Tracking changes in crustal thickness during orogenic evolution with Sr/Y: an example from the North American Cordillera. Geology 43, 919–922.
Chiaradia, M., 2015. Crustal thickness control on Sr/Y signatures of recent arc magmas: an earth scale perspective. Sci. Rep. 5, 8115.
Chiu, H.-Y., Chung, S.-L., Zarrinkoub, M.H., Mohammadi, S.S., Khatib, M.M., Iizuka, Y., 2013. Zircon U–Pb age constraints from Iran on the magmatic evolution related to Neotethyan subduction and Zagros orogeny. Lithos 162–163, 70–87.
Comin-Chiaramonti, P., Meriani, S., Mosca, R., Sinigoi, S., 1979. On the occurrence of analcime in the northeastern Azerbaijan volcanic rocks (north western Iran). Lithos 12, 187–198.
Conceição, R.V., Green, D.H., 2004. Derivation of potassic (shoshonitic) magmas by decompressing melting of phlogopite + pargasite lherzolite. Lithos 72, 209–229.
Conticelli, S., Peccerillo, A., 1992. Petrology and geochemistry of potassic and ultrapotassic volcanismin central Italy: petrogenesis and inferences on the evolution of the mantle sources. Lithos 28, 221–240.
Conticelli, S., Guarnieri, L., Farinelli, A., Mattei, M., Avanzinelli, R., Bianchini, G., Boari, E., Tommasini, S., Tiepolo, M., Prelević, D., Venturelli, G., 2009. Trace elements and Sr–Nd–Pb isotopes of K-rich, shoshonitic, and calc-alkaline magmatism of the western mediterranean region: genesis of ultrapotassic to calc alkaline magmatic associations in a post-collisional geodynamic setting. Lithos 107, 68–92.
Currie, C.A., Beaumont, C., Huismans, R.S., 2007. The fate of subducted sediments: a case for back arc intrusion and underplating. Geology 35, 1111–1114.
Dabiri, R., Emami, M.H., Mollaei, H., Chen, B., Abedini, M.V., Rashidnejad, N., Ghaffari, M., 2011. Quaternary post-collision alkaline volcanism NW of Ahar (NW Iran): geochemical constraints of fractional crystallization process. Geol. Carpath. 62, 547–562.
Dawson, J.B., 1987. The kimberlite clan: relationship with olivine and leucitite lamproites, and inferences for upper mantle metasomatism. In: Fitton, J.G., Upton, B.G. (Eds.), Alkaline Igneous.
Deer, W.A., Howie, R.A., Zussman, J., 1992. An Introduction to the Rock Forming Minerals, second edition. Longman, London, pp. 696.
Defant, M.J., Drummond, M.S., 1990. Derivation of some modern arc magmas by melting of young subducted lithosphere. Nature 34, 662–665.
Dehghani, G.A., Makris, T., 1984. The gravity field and crustal structure of Iran. Neues Jahrbuch fur Geologie und Palaontologie-Abhandlungen 168, 215–229.
DeMets, C., Gordon, R.G., Argus, D.F., Stein, S., 1990. Current plate motions. Int. J. Geophys. 101, 425–478.
DePaolo, D.J., 1981. Trace element and isotopic effects of combined wallrock assimilation and fractional crystallisation. Earth Planet. Sci. Lett. 53, 189–202.
Dewey, J.F., Pitman, W.C., Ryan, W.B.F., Bonnin, J., 1973. Plate tectonics and the evolution of the Alpine system. Geol. Soc. Am. Bull. 84, 3137–3180.
Didon, J., Gemain, Y.M., 1976. le Sabalan, Volcan Plio-Quaternaire de l'Azerbaidjan oriental (Iran): Ètude géologique et pétrographique de l'édifice et de son environment régional. Thèse, Docteur du 3 ème cycle. Univ. Grénoble, France, pp. 304.
Dilek, Y., Imamverdiyev, N., Altunkaynak, S., 2010. Geochemistry and tectonics of Cenozoic volcanism in the Lesser Caucasus (Azerbaijan) and the peri-Arabian region: collision-induced mantle dynamics and its magmatic fingerprint. Int. Geol. Rev. 52, 536–578.
Doglionli, C., 1995. Geological remarks on the relationships between extension and convergent geodynamic setting. Tectonophysics 252, 253–267.
Eby, G.N., 2004. Petrology, geochronology, mineralogy, and geochemistry of the Beemerville alkaline complex, northern New Jersey. In: Puffer, J.H., Volkert, R.A. (Eds.), Neoproterozoic, Paleozoic, and Mesozoic Intrusive Rocks of Northern New Jersey and Southeastern New York. Twenty-First Annual Meeting Geological Association of New Jersey, Mahwah, NJ, pp. 52–68.
Eby, G.N., Woolley, A.R., Din, V., Platt, G., 1998. Geochemistry and petrogenesis of nepheline syenites: Kasungu-Chipala, Ilomba, and Ulindi nepheline syenite intrusions, North Nyasa Alkaline Province. Malawi. J. Petrol. 39, 1405–1424.
Edwards, C.M.H., Menzies, M.A., Thirlwall, M.F., Morris, J.D., Leeman, W.P., Harmon, R.S., 1994. The transition to potassic alkaline volcanism in island arcs: the Ringgit-Beser complex, east Java, Indonesia. J. Petrol. 35, 1557–1595.
Emami, M.H., 2000. Magmatism in Iran. Geological survey of Iran, Tehran. Tech. Rep. 71, 608.
Espurt, N., Hippolyte, J.C., Kaymakci, N., Sangu, E., 2014. Lithospheric structural control on inversion of the southern margin of the Black Sea Basin, Central Pontides. Turk. Lithosphere 6, 26–34.
Eyuboglu, Y., Chung, S.L., Santosh, M., Dudas, F.O., Akaryali, E., 2011. Transition from shoshonitic to adakitic magmatism in the Eastern Pontides, NE Turkey: implications for slab window melting. Gondwana Res. 19, 413–429.
Eyuboglu, Y., Santosh, M., Yi, K., Bektas, O., 2012. Discovery of Miocene adakitic dacite from the Eastern Pontides belt (NE Turkey) and a revised geodynamic model for the late Cenozoic evolution of the Eastern mediterranean region. Lithos 146–147, 218–232.
Eyuboglu, Y., Santosh, M., Yi, K., Tuysuz, N., Korkmaz, S., Akaryali, E., Dudas, F.O., Bektas, O., 2014. The Eastern Black Sea-type volcanogenic massive sulfide deposits:

geochemistry, zircon U–Pb geochronology and an overview of the geodynamics of ore genesis. Ore Geol. Rev. 59, 29–54.
Fall, A., Bodnar, R.J., Szabó, C., Pál-Molnár, E., 2007. Fluid evolution in the nepheline syenites of the Ditrău alkaline Massif, Transylvania, Romania. Lithos 95, 331–345.
Farhoudi, G., 1978. A comparison of Zagros geology to island arcs. J. Geol. 86, 323–334.
Fitton, J.G., 1987. The Cameroon line, West Africa: a comparison between oceanic and continental alkaline volcanism. In: In: Fitton, J.G., Upton, B.G.J. (Eds.), Alkaline Igneous Rocks 30. Geological Society, London, pp. 413–431 Special publications.
Fitton, J.G., Upton, B.G.J., 1987. Alkaline Igneous Rocks 30. Geological Society, London, pp. 568 Special publications.
Foley, S.F., Venturelli, G., Green, D.H., Toscani, L., 1987. The ultra-potassic rocks: characteristics, classification and constraints for petrogenetic models. Earth Sci. Rev. 24, 81–134.
Förster, H., Fesefeldt, K., Kürsten, M., 1972. Magmatic and orogenic evolution of the central Iranian volcanic belt. Armstrong, J.E., Hedberg, H.D. (Eds.), 24th International Geologic Congress 198–210.
Frezzotti, M., Angelo Peccerillo, A., Panza, G., 2009. Carbonate metasomatism and CO_2 lithosphere–asthenosphere degassing beneath the Western mediterranean: an integrated model arising from petrological and geophysical data. Chem. Geol. 262, 108–120.
Frost, B.R., Frost, C.D., 2008. A geochemical classification for feldspathic igneous Rocks. J. Petrol. 49, 1955–1969.
Frost, B.R., Arculus, R.J., Barnes, C.G., Collins, W.J., Ellis, D.J., Frost, C.D., 2001. A geochemical classification of granitic rocks. J. Petrol. 42, 2033–2048.
Funiciello, F., Moroni, M., Piromallo, C., Faccenna, C., Cenedese, A., Bui, H.A., 2006. Mapping mantle flow during retreating subduction: laboratory models analyzed by feature tracking. J. Geoph. Res. Solid Earth 111 (B3), B03402.
Furman, T., Graham, D., 1999. Erosion of lithospheric mantle beneath the east African rift system: geochemical evidence from the Kivu volcanic province. Lithos 48, 237–262.
Galoyan, G., Rolland, Y., Sosson, M., Corsini, M., Melkonyan, R., 2007. Evidence for superposed MORB, oceanic plateau and volcanic arc series in the Lesser Caucasus (Stepanavan, Armenia). Comptes Rendus Geosci. 339, 482–492.
Galoyan, G., Rolland, Y., Sosson, M., Corsini, M., Billo, S., Verati, C., Melkonyan, R., 2009. Geochemistry and $^{40}Ar/^{39}Ar$ dating of Sevan Ophiolites, Lesser Caucasus, Armenia): evidences for jurassic Back-arc opening and hot spot event between the South Armenian block and Eurasia. J. Asian Earth Sci. 34, 135–153.
Gao, Y., Wei, R., Ma, P., Hou, Z., Yang, Z., 2009. Post-collisional ultrapotassic volcanism in the Tangra Yumco-Xuruco graben, south Tibet: constraints from geochemistry and Sr–Nd–Pb isotope. Lithos 110, 129–139.
Ghasemi, A., Talbot, C.J., 2006. A new tectonic scenario for the Sanandaj-Sirjan zone (Iran). J. Asian Earth Sci. 26, 683–693.
Giret, A., Bonin, B., Leger, J.M., 1980. Amphibole compositional trends in oversaturated and undersaturated alkaline plutonic ring complexes. Can. Mineral. 18, 481–495.
Green, T.H., 1995. Significance of Nb/Ta as an indicator of geochemical processes in the crust mantle system. Chem. Geol. 120, 347–359.
Grove, T.L., Parman, S.W., Bowring, S.A., Price, R.C., Baker, M.B., 2002. The role of an H_2O-rich fluid component in the generation of primitive basaltic andesites and andesites form the Mt. Shasta region, N. California. Contrib. Mineral. Petrol. 142, 375–396.
Guest, B., Axen, G.J., Lam, P.S., Hassanzadeh, J., 2006. Late Cenozoic shortening in the west-central Alborz mountains, northern Iran, by combined conjugate strike-slip and thin-skinned deformation. Geosphere 2, 35–52.
Hajalilou, B., Moayyed, M., Hosseinzadeh, Gh., 2009. Petrography, geochemistry and geodynamic environment of potassic alkaline rocks in eslamy peninsula, northwest of Iran. J. Earth Syst. Sci. 118, 643–657.
Hamilton, W.B., 1995. Subduction systems and magmatism. In: In: Smellie, J.L. (Ed.), Volcanism Associated With ExtenSion at Consuming Plate Margins 81. Geological Society, London, pp. 3–28 Special Publications.
Harris, N.B.W., Kelley, S., Okay, A.I., 1994. Post-collision magmatism and tectonics in northwest Anatolia. Contrib. Mineral. Petrol. 117, 241–252.
Hassanzadeh, J., 1993. Metallogenic and Tectonomagmatic Events in the SE Sector of the Cenozoic Active Continental Margin of Iran (Shahre-Babak Area, Kerman Province). Ph.D Thesis. University of California, Los Angeles, pp. 204.
Hassanzadeh, J., Ghazi, A.M., Axen, G., Guest, B., 2002. Oligomiocene mafic-alkaline magmatism north and northwest of Iran: evidence for the separation of the Alborz from the Urumieh–Dokhtar magmatic arc. Geol. Soc. Am. Abstr. Programs 34, 331.
Hassanzadeh, J., Axen, G., Guest, B., Stockli, D.F., Ghazi, A.M., 2004. The Alborz and NW Urumieh-Dokhtar magmatic belts, Iran: Rifted parts of a single ancestral arc. Geol. Soc. Am. Abstr. Programs 36, 434.
Hässig, M., Rolland, Y., Sosson, M., Galoyan, G., Müller, C., Avagyan, A., Sahakyan, L., 2013. New structural and petrological data on the Amasia ophiolites (NW Sevan–Akera suture zone, Lesser Caucasus): insights for a large-scale obduction in Armenia and NE Turkey. Tectonophysics 588, 135–153.
Hässig, M., Rolland, Y., Sosson, M., 2015. From Sea-Floor Spreading to Obduction: Jurassic Cretaceous Evolution of the Northern Branch of the Neotethys to Obduction Initiation: History of the Northern Branch of Neotethys in the North-Eastern Anatolian and Lesser Caucasus Regions. Geological Society of London Special Publication 428 (SP428.10).
Hawkesworth, C.J., Kempton, P.D., Rogers, N.W., Ellam, R.M., van Calstern, P.W., 1990. Continental mantle lithosphere and shallow level enrichment processes in the earth's mantle. Earth. Planet. Sci. Lett. 96, 256–268.
Hessami, K., Koyi, H.A., Talbot, C.J., Tabasi, H., Shabanian, E., 2001. Progressive unconformities within an evolving foreland fold-thrust belt, Zagros mountains. J. Geol. Soc. Lond. 158, 969–981.
Hofmann, A.W., Jochum, K.P., Seufert, M., White, W.M., 1986. Nb and Pb in oceanic basalts: new constraints on mantle evolution. Earth. Planet. Sci. Lett. 79, 33–45.
Ilbeyli, N., 2005. Mineralogical–geochemical constraints on intrusives in central Anatolia, Turkey: tectono-magmatic evolution and characteristics of mantle source. Geol. Mag. 142, 187–207.
Ilbeyli, N., Pearce, J.A., Thirlwall, J.G., Mitchell, J.G., 2004. Petrogenesis of collision-related plutonics in Central Anatolia. Turk. Lithos 72, 163–182.
Jackson, J.A., McKenzie, D., 1984. Active tectonics of the Alpine–Himalayan belt between western Turkey and Pakistan. Geophys. J. R. Astron. Soc. 77, 185–264.
Jagoutz, O.E., 2010. Construction of the granitoid crust of an island arc. Part II: a quantitative petrogenetic model. Contrib. Mineral. Petrol. 160, 359–381.
Jagoutz, O., Klein, B., 2018. On the importance of crystallization-differentiation for the generation of SiO_2-rich melts and the compositional build-up of arc (and continental) crust. Am. J. Sci. 318, 29–63.
Jahangiri, A., 2007. Post-collisional Miocene adakitic volcanism in NW Iran: geochemical and geodynamic implications. J. Asian Earth Sci. 30, 433–447.
Jourdan, F., Bertrand, H., Schärer, U., Blichert-Toft, J., Feraud, G., Kampunzu, A.B., 2007. Major and trace element and Sr, Nd, Hf, and Pb isotope compositions of the Karoo large igneous Province, Botswana-Zimbabwe: lithosphere vs mantle plume contribution. J. Petrol. 48, 1043–1077.
Jung, S., Mezger, K., Hoernes, S., 2004. Shear zone-related syenites in the Damara belt (Namibia): the role of crustal contamination and source composition. Contr. Mineral. Petrol. 148, 104–121.
Kaislaniemi, L., Van Hunen, J., Allen, M.B., Neill, I., 2014a. Sublithospheric small-scale convection – A mechanism for collision zone magmatism. Geology 42, 291–294.
Kaislaniemi, L., Van Hunen, J., Allen, M.B., Neill, I., 2014b. Sublithospheric small-scale convection – A mechanism for collision zone magmatism. Geology 42, 291–294.
Kazmin, V.G., Sbortshikov, I.M., Ricou, L.-E., Zonenshain, L.P., Boulin, J., Knipper, A.L., 1986. Volcanic belts as markers of the Mesozoic-Cenozoic active margin of Eurasia. Tectonophysics 123, 123–152.
Kelemen, P.B., Hanghøj, K., Greene, A.R., 2003. One view of the geochemistry of subduction-related magmatic arcs, with an emphasis on primitive andesite and lower crust. In: In: Rudnick, R.L. (Ed.), Treatise on Geochemistry 3. Elsevier, pp. 593–659.
Keskin, M., 2003. Magma generation by slab steepening and breakoff beneath a subduction-accretion complex: an alternative model for collision-related volcanism in Eastern Anatolia. Turk. Geophys. Res. Lett. 30 (24), 8046.
Keskin, M., Genç, Ş.C., Tüysüz, O., 2008. Petrology and geochemistry of post-collisional Middle Eocene volcanic units in North-Central Turkey: evidence for magma generation by slab breakoff following the closure of the Northern Neotethys Ocean. Lithos 104, 267–305.
Kincaid, C., Griffiths, R.W., 2004. Variability in flow and temperatures within mantle subduction zones. Geochem. Geophys. Geosyst. 5, Q06002.
Kinzler, R.J., 1997. Melting of mantle peridotite at pressures approaching the spinel to garnet transition: application to midocean ridge basalt petrogenesis. J. Geophys. Res. 102, 853–874.
Korobeinikova, A.N., Laajokib, K., Gehor, S., 2000. Nepheline-bearing alkali feldspar syenite (pulaskite) in the Khibina pluton, Kola Peninsula, NW Russia: petrological investigation. J. Asian Earth Sci. 18, 205–212.
LaFlèche, M.R., Camire, G., Jenner, G.A., 1998. Geochemistry of post-Acadian, Carboniferous continental intraplate basalts from the Maritimes Basin, Magdalen islands, Quebec. Can. Chem. Geol. 148, 115–136.
LaTourette, T., Hervig, R.L., Holloway, J.R., 1995. Trace element partitioning between amphibole, phlogopite, and basanite melt. Earth. Planet. Sci. Lett. 135, 13–30.
Le Bas, M.J., Le Maitre, R.W., Streckeisen, A., Zanetti, B., 1986. A chemical classification of volcanic rock based on the total alkali–silica diagram. J. Petrol. 27, 745–750.
Le Maitre, R.W., 1989. . A Classification of Igneous Rocks and Glossary of Terms. Blackwell Scientific Publication, Oxford, pp. 193.
Le Maitre, R.W., Streckeisen, A., Zanettin, B., Le Bas, M.J., Bonin, B., Bateman, P., Bellieni, G., Dudek, A., Efremova, S.A., Keller, J., Lameyre, J., Sabine, P.A., Schmid, R., Sørensen, H., Woolley, A.R., 2002. Igneous Rocks: a Classification Glossary of Terms. Cambridge University Press, Cambridge, pp. 236.
Leake, B.E., Woolley, A.R., Arps, C.E.S., Birch, W.D., Gilbert, M.C., Grice, J.D., Hawthorne, F.C., Kato, A., Kisch, H.J., Krivovichev, V.G., Linthout, K., Laird, J., Mandarino, J.A., Maresch, W.V., Nickel, E.H., Rock, N.M.S., Schumacher, J.C., Smith, D.C., Stephenson, N.C.N., Ungaretti, L., Whittaker, E.J.W., Youzhi, G., 1997. Nomenclature of amphiboles: report of the subcommittee on amphiboles of the international mineralogical association, commission on new minerals and minerals name. Am. Mineral. 82, 1019–1037.
Lefebvre, C., Meijers, M.J.M., Kaymakci, N., Peynircioglu, A., Langereis, C.G., Van Hinsbergen, D.J.J., 2013. Reconstructing the geometry of central Anatolia during the late Cretaceous: large-scale Cenozoic rotations and deformation between the Pontides and Taurides. Earth Planet. Sci. Lett. 366, 83–98.
Lescuyer, J.L., Riou, R., 1976. Géologie de la system de Mianeh (Azerbaijan): Contribution a l'étude du volcanisme Tertiaire de l'Iran: Thèse. Univ. Grénoble, France, pp. 232.
Leterrier, J., Maury, R.C., Thonon, P., Girad, D., Marchel, M., 1982. Clinopyroxene composition as a method of identification of the magmatic affinities of paleo-volcanic series. Earth. Planet. Sci. Lett. 59, 139–154.
Liotard, J.M., Dauria, J.M., Bosch, D., Condomines, M., Mehdizadeh, H., Ritz, J.F., 2008. Origin of the absarokite–banakite association of the Damavand volcano (Iran): trace element and Sr, Nd, Pb isotope constraints. Int. J Earth Sci. (Geol Rundsch) 97, 89–102.
Litvinovsky, B.A., Jahn, B.M., Zanvilevich, A.N., Shadaev, M.G., 2002. Crystal fractionation in the petrogenesis of an alkali monzodiorite-syenite series: the Oshurkovo plutonic sheeted complex, Transbaikalia, Russia. Lithos 64, 97–130.
Lordkipanidze, M.B., Meliksetian, B., Djarbashian, R., 1989. Mesozoic-Cenozoic magmatic evolution of the Pontian–Crimean–Caucasian region. In: In: Raku's, M., Dercourt, J., Nairn, A.E.M. (Eds.), IGCP Project No. 198: Evolution of the Northern

Margin of Tethys. Mem. Soc. Geol. France 154. pp. 103–124.
Mahdavi, M.A., Aminifazl, A., 1989. Geological Map of Ahar Quadrangle (scale 1:100,000). Geological Survey of Iran, Tehran.
Marks, M.A.W., Hettmann, K., Schilling, J., Frost, B.R., Markl, G., 2011. The mineralogical diversity of alkaline igneous rocks: critical factors for the transition from miaskitic to agpaitic phase assemblages. J. Petrol. 52, 439–455.
Martin, H., 1999. The adakitic magmas: modern analogues of Archaean granitoids. Lithos 46, 411–429.
McKenzie, D.P., O'Nions, R.K., 1991. Partial melt distribution from inversion of rare earth element concentrations. J. Petrol. 32, 1021–1091.
McKenzie, D.P., O'Nions, R.K., 1995. The source regions of Ocean Island Basalts. J. Petrol. 36, 133–159.
McQuarrie, N., van Hinsbergen, D.J.J., 2013. Retrodeforming the Arabia–Eurasia collision zone: age of collision versus magnitude of continental subduction. Geology 41, 315–318.
McQuarrie, N., Stock, J.M., Verdel, C., Wernicke, B., 2003. Cenozoic evolution of Neotethys and implications for the causes of plate motions. Geophys. Res. Lett. 30 (20), 2036.
Mederer, J., Moritz, R., Ulianov, A., Chiaradia, M., 2013. Middle Jurassic to Cenozoic evolution of arc magmatism during Neotethys subduction and arc-continent collision in the Kapan zone, southern Armenia. Lithos 177, 61–78.
Mehrpartou, M., Nazer, N.Kh., 1999. Geological Map of Kaleybar Quadrangle (scale 1:100,000). Geological Survey of Iran, Tehran.
Mehrpartou, M., Aminifazl, A., Radfar, J., 1992. Geological Map of Varzghan Quadrangle (scale 1:100,000). Geological Survey of Iran, Tehran.
Meijers, M.J.M., Vrouwe, B., van Hinsbergen, D.J.J., Kuiper, K.F., Wijbrans, J., Davies, G.R., Stephenson, R.A., Kaymakci, N., Matenco, L., Saintot, A., 2010. Jurassic arc volcanism on Crimea (Ukraine): implications for the paleo-subduction zone configuration of the Black Sea region. Lithos 119, 412–426.
Menzies, M., 1987. Alkaline rocks and their inclusions: a window on the earth's interior. In: In: Fitton, J.G., Upton, B.G. (Eds.), Alkaline Igneous Rocks 30. Geological Society, London, pp. 15–27 Special publications.
Middlemost, E.A.K., 1994. Naming materials in the magma/igneous rock system. Earth Sci. Rev. 37, 215–224.
Moayyed, M., Moazzena, M., Calagari, A.A., Jahangiri, A., Modjarrad, M., 2008. Geochemistry and petrogenesis of lamprophyric dykes and the associated rocks from Eslamy peninsula, NW Iran: implications for deep-mantle metasomatism. Chem. Erde 68, 141–157.
Modjarrad, M., Moayyed, M., Hosseinzadeh, G., 2011. The Hashtsar gabbro: influence of subduction-related metasomatism. Iran. J. Geol. 19, 61–80.
Mohajjel, M., Fergusson, C.L., 2000. Dextral transpression in late-Cretaceous continental collision, Sanandaj—Sirjan zone, western Iran. J. Struct. Geol. 22, 1125–1139.
Moinevaziri, H., 1999. An Introduction to the Magmatism in Iran. Kharazmi University Publication, Tehran, pp. 440 (in Persian).
Moradian, A., 1997. Geochemistry, Geochronology and Petrography of Feldspathoid Bearing Rocks in Urumieh-Dokhtar Volcanic Belt, Iran. Ph.D Thesis. University of Wollongong, Australia, pp. 412.
Morimoto, N., 1989. Nomenclature of pyroxenes. Can. Mineral. 27, 143–156.
Moritz, R., Melkonyan, R., Selby, D., Popkhadze, N., Gugushvili, V., Tayan, R., Ramazanov, V., 2016a. Metallogeny of the Lesser Caucasus: from arc construction to post-collision evolution. In: In: Richards, J. (Ed.), Tethyan Tectonics and Metallogeny 19. pp. 157–192 Special Publication of the Society of Economic Geology.
Moritz, R., Rezeau, H., Ovtcharova, M., Tayan, R., Melkonyan, R., Hovakimyan, S., Ramazanov, V., Selby, D., Ulianov, A., Chiaradia, M., Putlitz, B., 2016b. Long-lived, stationary magmatism and pulsed porphyry systems during Tethyan subduction to post-collision evolution in the southernmost Lesser Caucasus, Armenia and Nakhitchevan. Gondwana Res. 37, 465–503.
Morley, C.K., Kongwung, B., Julapour, A.A., Abdolghafourian, M., Hajian, M., Waples, D., Warren, J., Otterdoom, H., Srisuriyon, K., Kazeni, H., 2009. Structural development of a major late Cenozoic basin and transpressional belt in central Iran: The Central Basin in the Qom-Saveh area. Geosphere 5, 325–362.
Morrison, G.W., 1980. Characteristics and tectonic setting of the shoshonite rock association. Lithos 13, 97–108.
Motoki, A., Sichel, S.E., Vargas, T., Melo, D.P., Motoki, K.F., 2015. Geochemical behaviour of trace elements during fractional crystallization and crustal assimilation of the felsic alkaline magmas of the state of Rio de Janeiro, Brazil. Anais da Academia Brasileira de Ciências 87, 1959–1979.
Mouthereau, F., Lacombe, O., Vergés, J., 2012. Building the Zagros collisional orogen: timing, strain distribution and the dynamics of Arabia/Eurasia plate convergence. Tectonophysics 532, 27–60.
Muller, D., Groves, D.I., 1997. Potassic Igneous Rocks and Associated Gold-Copper Mineralization. Second Updated and Enlarged Edition. Springer, pp. 238.
Muller, D., Groves, D.I., 2000. Potassic Igneous Rocks and Associated Gold-Copper Ineralizations. Springer, Berlin, pp. 252.
Muller, D., Rock, N.M.S., Groves, D.I., 1992. Geochemical discrimination between shoshonitic and potassic volcanic rocks from different tectonic setting: a pilot study. Mineral. Petrol. 46, 259–289.
Nabatian, G., Ghaderi, M., Neubauer, F., Honarmand, M., Liu, X., Dong, Y., Jiang, S.Y., Quadt, A., Bernroider, M., 2014. Petrogenesis of Tarom high-potassic granitoids in the Alborz–Azerbaijan belt, Iran: geochemical, U–Pb zircon and Sr–Nd–Pb isotopic constraints. Lithos 184–187, 324–345.
Nandedkar, R.H., Ulmer, P., Müntener, O., 2014. Fractional crystallization of primitive, hydrous arc magmas: an experimental study at 0.7 GPa. Contrib. Mineral. Petrol. 167, 1–27.
Neill, I., Meliksetian, K., Allen, M.B., Navasardyan, G., Kuiper, K., 2015. Petrogenesis of mafic collision zone magmatism: The Armenian sector of the Turkish–Iranian plateau. Chem. Geol. 403, 24–41.
Okay, A.I., Zattin, M., Cavazza, W., 2010. Apatite fission-track data for the Miocene Arabia-Eurasia collision. Geology 38, 35–38.
Okay, A.I., Nikishin, A.M., 2015. Tectonic evolution of the southern margin of Laurasia in the Black Sea region. Int. Geol. Rev. 57, 1051–1076.
Pang, K.N., Chung, S.L., Zarrinkoub, H.S., Lin, Y.C., Lee, H.Y., Lo, C.H., Khatib, M.M., 2013. Iranian ultrapotassic volcanism at ~11 Ma signifies the initiation of post-collisional magmatism in the Arabia–Eurasia collision zone. Terra Nova 25, 405–413.
Pearce, J.A., 1983. Role of the sub-continental lithosphere in magma genesis at active continental margins. In: Hawkesworth, C.J., Norry, M.J. (Eds.), Continental Basalts and Mantle Xenoliths. Shiva, UK, pp. 230–249.
Pearce, J.A., Bender, J.F., De Long, S.E., Kidd, W.S.F., Low, P.J., Güner, Y., Saroglu, F., Yilmaz, Y., Moorbath, S., Mitchell, J.G., 1990. Genesis of collision volcanism in eastern Anatolia, Turkey. J. Volcanol. Geotherm. Res. 44, 189–229.
Peccerillo, A., Frezzotti, M.L., 2015. Magmatism, mantle evolution and geodynamics at the converging plate margins of Italy. J. Geol. Soc. Lond. 172, 407–427.
Peccerillo, A., Taylor, S.R., 1976. Geochemistry of Eocene calc-alkaline volcanic rocks from the Kastamanou area, northern Turkey. Contrib. Mineral. Petrol. 58, 63–81.
Pe-Piper, G., Piper, D.J.W., Koukouvelas, I., Dolansky, L., Kokkalas, S., 2009. Postorogenic shoshonitic rocks and their origin by melting underplated basalts: The Miocene of Limnos, Greece. Geol. Soc. Am. Bull. 121, 39–54.
Prelević, D., Foley, S.F., Romer, R.L., Conticelli, S., 2008. Mediterranean tertiary lamproites: multicomponentmelts in post-collisional geodynamics. Geochim. Cosmochim. Acta 72, 2125–2156.
Prelević, D., Akal, C., Foley, S., Romer, R., Stracke, A., Van Den Bogaard, P., 2012. Ultrapotassic mafic rocks as geochemical proxies for post-collisional dynamics of orogenic lithospheric mantle: the case of southwestern Anatolia, Turkey. J. Petrol. 53, 1019–1055.
Prelević, D., Akal, C., Romer, R.L., Mertz-Kraus, R., Helvacı, C., 2015. Magmatic response to slab tearing: constraints from the Afyon alkaline volcanic complex, Western Turkey. J. Petrol. 56, 527–562.
Rezaeian, M., Carter, A., Hovius, N., Allen, M.B., 2012. Cenozoic exhumation history of the Alborz mountains, Iran: New constraints from low temperature chronometry. Tectonics 31, TC2004.
Rezeau, H., Moritz, R., Wotzlaw, J.F., Tayan, R., Melkonyan, R., Ulianov, A., Selby, D., d'Abzac, F.X., Stern, R.A., 2016. Temporal and genetic link between incremental pluton assembly and pulsed porphyry Cu-Mo formation in accretionary orogens. Geology 44, 627–630.
Rezeau, H., Moritz, R., Leuthold, J., Moritz, R., Hovakimyan, S., Tayan, R., Chiaradia, M., 2017. 30 Myr of Cenozoic magmatism along the Tethyan margin during Arabia-Eurasia accretionary orogenesis (Meghri-Ordubad pluton, southernmost Lesser Caucasus). Lithos. https://doi.org/10.1016/j.lithos.2017.07.007.
Richards, J.P., 2015. Tectonic, magmatic, and metallogenic evolution of the Tethyan orogen: from subduction to collision. Ore Geol. Rev. 70, 323–345.
Richards, J.P., Sholeh, A., 2016. The tethyan tectonic history and Cu-Au metallogeny of Iran. Soc. Econ. Geol. Spec. Publ. 19, 193–212.
Rieder, M., Cavazzini, G., Yakonov, Y.D., Frank-Kanetskii, V.A., Gottardi, G., Guggenheim, S., Koval, P.V., Müller, G., Neiva, A.M.R., Radoslovich, E.W., Robert, J.L., Sassi, F.P., Takeda, H., Weiss, Z., Wones, D.R., 1998. Nomenclature of the micas. Can. Mineral. 36, 905–912.
Robertson, A., Parlak, O., Ustaomer, T., Tasli, K., Inan, N., Dumitrica, P., Karaoglan, F., 2014. Subduction, ophiolite genesis and collision history of Tethys adjacent to the Eurasian continental margin: new evidence from the eastern Pontides, Turkey. Geodinamica Acta 26, 230–293.
Robinson, A., Rudat, J.H., Banks, C.J., Wiles, R.L.F., 1996. Petroleum geology of the Black Sea. Mar. Pet. Geol. 13, 195–223.
Rolland, Y., 2017. Caucasus collisional history: review of data from East Anatolia to West Iran. Gondwana Res. 49, 130–146.
Rolland, Y., Billo, S., Corsini, M., Sosson, M., Galoyan, G., 2009. Blueschists of the Amassia–Stepanavan suture zone (Armenia): linking tethys subduction history from E-Turkey to W-Iran. Int. J. Earth Sci. 98, 533–550.
Rolland, Y., Galoyan, G., Sosson, M., Melkonyan, R., Avagyan, A., 2010. The Armenian Ophiolite: insights for Jurassic back-arc formation, Lower Cretaceous hot spot magmatism, and Upper Cretaceous obduction over the South Armenian block. Geol. Soc. Lond. Spec. Publ. 340, 353–382.
Rolland, Y., Perincek, D., Kaymakci, N., Sosson, M., Barrier, E., Avagyan, A., 2012. Evidence for ~80–75 Ma subduction jump during Anatolide–Tauride–Armenian block accretion and ~48 Ma Arabia–Eurasia collision in Lesser Caucasus–East Anatolia. J. Geodyn. 56, 76–85.
Rollinson, H.R., 1993. Using Geochemical Data: Evaluation, Presentation, Interpretation. Longman Scientific and Technical. Wiley, New York, pp. 352.
Rollinson, H.R., Tarney, J., 2005. Adakites—the key to understanding LILE depletion in granulites. Lithos 79, 61–81.
Rudnick, R.L., Gao, S., 2003. Composition of the continental crust. In: Holland, H.D., Turekian, K.K. (Eds.), Treatise on Geochemistry. Elsevier-Pergamon, Oxford, pp. 1–64.
Sengör, A.M.C., 1984. The Cimmeride Orogenic System and Tectonics of Eurasia. Geological Society of America, pp. 195 Special Paper.
Sengör, A.M.C., Ozeren, S., Genc, T., Zor, E., 2003. East Anatolian high plateau as a mantle-supported, north-south shortened domal structure. Geophys. Res. Lett. 30, 8045.
Shafaii-Moghadam, H.S., Ghorbani, G., Khedr, M.Z., Fazlnia, N., Chiaradia, M., Eyuboglu, Y., Santosh, M., Francisco, C.G., Martinez, M.L., Gourgaud, A., Arai, S., 2014. Late Miocene K-rich volcanism in the Eslamieh peninsula (Saray), NW Iran: implications for geodynamic evolution of the Turkish–Iran. Gondwana Res. 26, 1028–1050.
Shaw, D.M., 1970. Trace element fractionation during anatexis. Geochim. Cosmochim.

Acta 34, 237–243.
Shaw, D.M., 1979. Trace element melting models. Physics and Chemistry of the Earth 11. pp. 577–586.
Sørensen, H., 1997. The agpaitic rocks, an overview. Mineral. Mag. 61, 485–498.
Sosson, M., Rolland, Y., Danelian, T., Muller, C., Melkonyan, R., Adamia, S., Kangarli, T., Avagyan, A., Galoyan, G., 2010. Subductions, obduction and collision in the Lesser Caucasus (Armenia Azerbaijan, Georgia), new insights. In: In: Sosson, M., Kaymakci, N., Stephenson, R.F., Bergerat, F., Starostenko, V. (Eds.), Sedimentary Basin Tectonics from the Black Sea and Caucasus to the Arabian Platform 340. Geological Society of London, pp. 329–352 Special Publication.
Sosson, M., Stephenson, R., Sheremet, Y., Rolland, Y., Adamia, S., Melkonian, R., Kangarli, T., Yegorova, T., Avagyan, A., Galoyan, G., Danelian, T., Hassig, M., Meijers, M., Muller, C., Sahakyan, L., Sadradze, N., Alania, V., Enukidze, O., Mosar, J., 2016. The eastern Black Sea-Caucasus region during the Cretaceous: New evidence to constrain its tectonic evolution. Comptes Rendus Geosci. 348, 23–32.
Spies, O., Lensch, G., Mihm, A., 1984. Petrology and geochemistry of the post-ophiolitic tertiary volcanics between Sabzevar and Quchan, NE Iran. Neues Jahrbuch für Geologie und Paläontologie-Abhandlungen 168, 389–408.
Stöcklin, J., 1968. Structural history and tectonics of Iran: A review. Am. Assoc. Petrol. Geol. Bull. 52, 1229–1258.
Stöcklin, J., Nabavi, M.H., 1973. Tectonic Map of Iran (scale 1:2,500,000). Geological Survey of Iran, Tehran.
Stolper, E., Newman, S., 1994. The role of water in the petrogenesis of Mariana trough magmas. Earth. Planet. Sci. Lett. 121, 293–325.
Stussi, J.M., Cuney, M., 1996. Nature of biotites from alkaline, calc-alkaline and peraluminous magmas by Abdel-Fattah M. Abdel-Rahman: a comment. J. Petrol. 37, 1025–1029.
Sun, S.S., McDonough, W.F., 1989. Chemical and isotopic systematics of oceanic basalts: implications for mantle composition and processes. In: In: Saunders, A.D., Norry, M.J. (Eds.), Magmatism in the Ocean Basins. 42. Geological Society, London, pp. 313–345 Special Publications.
Sun, C.H., Stern, R., 2001. Genesis of Mariana shoshonites: contribution of the subduction component. J. Geophys. Res. 106, 589–608.
Tajbakhsh, Gh., Emami, M.H., Moinevaziri, H., Rashidnejad-Omran, N., 2012. Petrology, geochemistry and tectonomagmatic setting of Kaleybar intrusion (Eastern Azerbaijan). Iran. Sci. Q. J., Geosci. 22, 205–224.
Tatsumi, Y., Eggins, S., 1995. Subduction Zone Magmatism. Blackwell Science, pp. 211.
Taylor, S.R., McLennan, S.M., 1985. The Continental Crust: Its Composition and Evolution. Geoscience Texts. Blackwell Scientific Publications, London.
Turner, S., Arnaud, N., Liu, J., Rogers, N., Hawkesworth, C., Harris, N., Kelley, S., Calsteren, P.V., Deng, W., 1996. Post-collision, shoshonitic volcanism on the Tibetan plateau: implications for Gonvective thinning of the lithosphere and the source of ocean island basalts. J. Petrol. 37, 45–71.
Upton, P., Koons, P.O., Eberhart-Phillips, D., 2003. Extension and partitioning in an oblique subduction zone, New Zealand: constraints from three-dimensional numerical modeling. Tectonics 22 (6), 1068.
Van Hunen, J., Allen, M.B., 2011. Continental collision and slab break-off: A comparison of 3-D numerical models with observations. Earth. Planet. Sci. Lett. 302, 27–37.
Verdel, C.S., Wernicke, B.P., Hassanzadeh, J., Guest, B., 2011. A Paleogene extensional arc flare-up in Iran. Tectonics 30, TC3008.
Vincent, S.J., Allen, M.B., Ismail-Zadeh, A.D., Flecker, R., Foland, K.A., Simmons, M.D., 2005. Insights from the Talysh of Azerbaijan into the Paleogene evolution of the South Caspian region. Geol. Soc. Am. Bull. 117, 1513–1533.
Vincent, S.J., Morton, A.C., Carter, A., Gibbs, S., Barabadze, T.G., 2007. Oligocene uplift of the western Greater Caucasus: an effect of initial Arabia-Eurasia collision. Terra Nova 19, 160–166.
Walter, M.J., 1998. Melting of garnet peridotite and the origin of komatiite and depleted lithosphere. J. Petrol. 39, 29–60.
Wang, Q., Li, J.W., Jian, P., Zhao, Z.H., Xiong, X.L., Bao, Z.W., Xu, J.F., Li, C.F., Ma, J.L., 2005. Alkaline syenites in eastern Cathaysia (South China): link to Permian-Triassic transtension. Earth. Planet. Sci. Lett. 230 (339), 354.
Wood, I.A., Joron, J.L., Treuil, M., Norry, L., Tarney, J., 1979. Elemental and Sr isotope variations in basic lavas from Iceland and surrounding ocean floor. Contr. Mineral. Petrol. 70, 319–339.
Woodhead, J.D., Eggins, S.M., Johnson, R.W., 1998. Magma genesis in the New Britain Island arc: further insights into melting and mass transfer processes. J. Petrol. 39, 1641–1668.
Woolley, A.R., Jones, G.C., 1987. The petrochemistry of the northern part of the Chilwa alkaline province, Malawi. In: In: Fitton, J.G., Upton, B.G. (Eds.), Alkaline Igneous Rocks. 30. Geological Society, London, pp. 335–355 Special publications.
Yilmaz, A., Adamia, Sh., Chabukiani, A., Chkhotua, T., Erdogan, K., Tuzcu, S., Karabilykoglu, M., 2000. Structural correlation of the southern Transcaucasus (Georgia)-eastern Pontides (Turkey). In: In: Bozkurt, E., Winchester, J.A., Piper, J.D.A. (Eds.), Tectonics and Magmatism in Turkey and the Surrounding Area 173. Geological Society of London, pp. 171–182 Special Publication.
Zanvilevich, A.N., Litvinovsky, B.A., Wickham, S.M., Bea, F., 1995. Genesis of alkaline and peralkaline syenite-granite series, the Khartonovo pluton (Transbaikalia, Russia). J. Geol. 103, 127–145.
Zen, E., 1988. Phase relations of peraluminous granitic rocks and their petrogenetic implications. Annu. Rev. Earth Planet. Sci. 16, 21–52.
Zhang, X., Zhang, H., Jiang, N., Zhai, M., Zhang, Y., 2010. Early Devonian alkaline intrusive complex from the northern North China craton: a petrological monitor of post-collisional tectonics. J. Geol. Soc. Lond. 167, 717–730.
Zhao, J.H., Zhou, M.F., 2007. Geochemistry of Neoproterozoic mafic intrusions in the Panzhihua district (Sichuan Province, SW China): implications for subduction-related metasomatism in the upper mantle. Precambrian Res. 152, 27–47.
Zuo, X., Chan, L.S., Gao, J.F., 2017. Compression-extension transition of continental crust in a subduction zone: A parametric numerical modeling study with implications on Mesozoic-Cenozoic tectonic evolution of the Cathaysia block. PLoS One 12 (2), e0171536.